



University of Naples Federico II  
Department of Industrial Engineering

---

Doctorate School in Industrial Engineering

Ph.D. degree in Engineering of Mechanical Systems

# The Nonlinear Actuator Disk Method as Applied to Open and Ducted Rotors

Candidate:  
Rodolfo Bontempo

Advisors:  
Prof. Marcello Manna  
Prof. Andrea Vacca

Thesis submitted in 2014



---

## ABSTRACT

---

The thesis presents a generalized semi-analytical actuator disk model as applied to the analysis of the incompressible, axisymmetric and inviscid flow around open and ducted rotors. The method strongly couples the nonlinear actuator disk method of Conway (1998) (*J. Fluid Mech.* 1998; 365: 235-267) and the vortex element method of Martensen (1959) (*Arch. Rat. Mech.* 1959; 3: 235-270) and it returns the exact solution, although in an implicit formulation, as superposition of ring vortices properly arranged along the duct surface and the wake region. The solution is made explicit through a semi-analytical procedure which is validated with the help of asymptotic relations. The model duly accounts for non-uniform load radial distribution, slipstream contraction, mutual nonlinear interaction between duct and propeller, wake rotation, and ducts of general shape. Furthermore, the method can be easily employed to simulate the flow around an open rotor with a finite hub.

The thesis also presents an assessment of two existing numerical methods capable to simulate open and ducted rotors flow fields. The first is the aforementioned nonlinear and semi-analytical actuator disk method. The second is based on the introduction of an actuator disk model in a CFD package describing the effects of the rotor through radial profiles of blade forces distributed over a disk surface. A set of reference numerical data, providing the inviscid axisymmetric velocity and pressure field distributions, are generated with controlled accuracy. Owing to an in-depth analysis of the error generated by the semi-analytical method and to the exactness of

the solution in its implicit form, the collected data are well-suited for code-to-code validation of existing or newly developed computational methods.

Finally, thanks to its extremely reduced computational cost the semi-analytical procedure can easily be integrated into design systems based on the repeated analysis scheme of hierarchical type.

The computer code is freely available on contacting the author at the following e-mail address: `rodolfo.bontempo@unina.it`.

---

## ACKNOWLEDGEMENTS

---

I would like to express my deepest gratitude and appreciation to Prof. Marcello Manna for encouraging my research and for his assistance in making this thesis an exciting and enjoyable learning experience. I would thank Prof. Andrea Vacca for his guidance and the invaluable advices he gave me during my research.

Thanks are also due to the board of the PhD course in Engineering of Mechanical Systems and to Prof. Massimo Cardone. In addition, I want to thank my colleague Giovanni Vorraro for his friendship and assistance.

Finally, I thank my family and Daria for everything they have done for me.



---

# CONTENTS

---

<b>Nomenclature</b>	<b>xix</b>
<b>1 Exact Solution of the Flow over a non-Uniform Heavily Loaded Ducted Actuator Disk</b>	<b>1</b>
1.1 Introduction . . . . .	1
1.2 The open rotor flow model . . . . .	2
1.3 The duct alone flow model . . . . .	8
1.4 The coupled flow model . . . . .	10
1.5 Solution strategy . . . . .	11
1.6 Results and applications . . . . .	19
1.6.1 Ducted rotor without slipstream rotation . . . . .	20
1.6.2 Ducted rotor with slipstream rotation . . . . .	29
1.6.3 Comparison between open and ducted rotor . . . . .	39
<b>2 Flow Analysis of Open and Ducted Turbines and Comparison with CFD</b>	<b>45</b>
2.1 Introduction . . . . .	45
2.2 The ducted actuator disk flow model . . . . .	47
2.2.1 The ducted actuator disk flow model: theoretical background . . . . .	47
2.2.2 The ducted actuator disk flow model: the solution as superposition of ring vortex . . . . .	49

2.2.3	The ducted actuator disk flow model: solution strategy	51
2.3	Flow analysis of open and ducted turbines . . . . .	54
2.4	Error analysis and comparison with CFD . . . . .	58
2.4.1	The semi-analytical actuator disk method: error analysis . . . . .	59
2.4.2	The CFD actuator disk method: error analysis . . . . .	60
2.4.3	Semi-analytical and CFD actuator disk methods: comparison of the results . . . . .	64
<b>3</b>	<b>Flow Analysis of Open and Ducted Propellers and Comparison with CFD</b>	<b>71</b>
3.1	Introduction . . . . .	71
3.2	The duct effect: linear and nonlinear analysis . . . . .	76
3.3	Comparison between the semi-analytical and the CFD actuator disk method . . . . .	82
3.3.1	The semi-analytical actuator disk method with swirl: error analysis . . . . .	83
3.3.2	The 3D CFD actuator disk method with swirl: error analysis . . . . .	86
3.3.3	Semi-analytical and CFD actuator disk methods: comparison of the results . . . . .	88
<b>4</b>	<b>Exact Solution of the Flow over a non-Uniform Heavily Loaded Actuator Disk with Finite Hub</b>	<b>93</b>
4.1	Introduction . . . . .	93
4.2	The nonlinear actuator disk flow model with finite hub . . . . .	96
4.2.1	Theoretical aspects . . . . .	96
4.2.2	The semi-analytical solution procedure . . . . .	100
4.3	Discussion and analysis of the results . . . . .	108
4.4	Error analysis and comparison with CFD . . . . .	114
4.4.1	The semi-analytical actuator disk with finite hub: error analysis . . . . .	115
4.4.2	The CFD actuator disk with finite hub: mesh dependence analysis . . . . .	118
4.4.3	Semi-analytical and CFD actuator disk with finite hub: comparison of the results . . . . .	119
<b>5</b>	<b>Conclusions</b>	<b>123</b>
<b>A</b>	<b>The Green function of the linear elliptic operator <math>L_{(\zeta, \sigma)}</math></b>	<b>125</b>

<b>B Computation of Bessel-Laplace Integrals</b>	<b>131</b>
B.1 Recurrence relations . . . . .	131
B.2 Recursion schemes . . . . .	134
B.3 Analytical solutions for the Bessel-Laplace integrals . . . . .	137
<b>Bibliography</b>	<b>143</b>



---

## LIST OF FIGURES

---

1.1	Schematic view of the actuator disk geometrical configuration.	3
1.2	Schematic view and nomenclature used for the duct ring vortex distribution. . . . .	8
1.3	Schematic view of the ducted rotor geometrical configuration.	10
1.4	Propeller ducted with a NACA 4415 profile with $\hat{b} = 15$ : (a) duct wall pressure coefficient; (b) radial distribution of the load. . . . .	23
1.5	Propeller ducted with a NACA 4415 profile with $\hat{b} = 15$ : streamlines. . . . .	23
1.6	Propeller ducted with a NACA 4415 profile with $\hat{b} = 15$ : $\hat{u}$ (top) and $\hat{v}$ (bottom) radial distributions at different axial stations. . . . .	25
1.7	Propeller ducted with a NACA 4415 profile with $\hat{b} = 15$ : contours of total (top), axial (middle) and radial (bottom) velocity. . . . .	26
1.8	Propeller ducted with a NACA 4415 profile with $\hat{b} = 15$ : convergence analysis. . . . .	27
1.9	Propeller ducted with a NACA 4415 profile with $\hat{b} = 15$ : approach of the $\hat{u}$ radial distribution to the asymptotic one. . . . .	28
1.10	Propeller ducted with a NACA 4415 profile with $\hat{b} = 15$ and $J = 0.5$ : (a) duct wall pressure coefficient; (b) radial distribution of the load. . . . .	31

LIST OF FIGURES

1.11	Turbine ducted with a NACA 5415 profile with $\hat{b} = -2$ and $\lambda = 2\pi$ : (a) duct wall pressure coefficient; (b) radial distribution of the load. . . . .	31
1.12	Propeller ducted with a NACA 4415 profile with $\hat{b} = 15$ and $J = 0.5$ : projection of the generatrices of the stream-tubes onto the meridian plane. . . . .	32
1.13	Turbine ducted with a NACA 5415 profile with $\hat{b} = 2$ and $\lambda = 2\pi$ : projection of the generatrices of the stream-tubes onto the meridian plane. . . . .	32
1.14	Propeller ducted with a NACA 4415 profile with $\hat{b} = 15$ and $J = 0.5$ : $\hat{u}$ (top) and $\hat{v}$ (bottom) radial distributions at different axial stations. . . . .	33
1.15	Turbine ducted with a NACA 5415 profile with $\hat{b} = -2$ and $\lambda = 2\pi$ : $\hat{u}$ (top) and $\hat{v}$ (bottom) radial distributions at different axial stations. . . . .	34
1.16	$\hat{w}$ radial distribution at different axial stations. Top: propeller ( $\hat{b} = 15$ and $J = 0.5$ ) ducted with a NACA 4415 profile. Bottom: turbine ( $\hat{b} = -2$ and $\lambda = 2\pi$ ) ducted with a NACA 5415 profile. . . . .	35
1.17	Propeller ducted with a NACA 4415 profile with $\hat{b} = 15$ and $J = 0.5$ : contours of total (top), axial (middle) and radial (bottom) velocity. . . . .	36
1.18	Turbine ducted with a NACA 5415 profile with $\hat{b} = -2$ and $\lambda = 2\pi$ : contours of total (top), axial (middle) and radial (bottom) velocity. . . . .	37
1.19	Propeller ducted with a NACA 4415 profile with $\hat{b} = 15$ and $J = 0.5$ : convergence analysis. . . . .	38
1.20	$\hat{u}$ distribution at different axial stations for rotors with slipstream rotation. Top: propeller described in Table 1.1. Bottom: turbine described in Table 1.4. . . . .	40
1.21	Load radial distribution for open and ducted rotors. Left: turbines. Right: propellers. . . . .	41
1.22	Comparison of the open and the ducted turbine slipstream edge. . . . .	42
1.23	Comparison of the open and the ducted propeller slipstream edge. . . . .	44
2.1	Computed power coefficient versus rotor thrust coefficient for open and ducted turbines. . . . .	55

2.2	Load radial distributions related to simulations reported in Fig 2.1. . . . .	56
2.3	Computed mass flow ratio $\dot{m}_{ducted}/\dot{m}_{open}$ . . . . .	57
2.4	Computational domain. Left: full size; right: inner domain. . . . .	63
2.5	Open turbine: comparison of the radial (top) and axial (bottom) velocity profiles obtained through the semi-analytical (SAOT-5) and CFD (CFDOT-3 and CFDOT-1) actuator disk methods. . . . .	65
2.6	Turbine ducted with a NACA5415: comparison of the radial (top) and axial (bottom) velocity profiles obtained through the semi-analytical (SADT-5) and the CFD (CFDDT-3 and CFDDT-1) actuator disk methods. . . . .	66
2.7	Turbine ducted with a NACA5415: comparison of the wall pressure coefficient profile obtained through the semi-analytical (SADT-5) and the CFD (CFDDT-3 and CFDDT-1) actuator disk methods. . . . .	67
2.8	Computational cost of the semi-analytical and CFD actuator disk methods. . . . .	69
3.1	Efficiency comparison between open and ducted propellers. . . . .	79
3.2	Duct thrust coefficient for ducted propellers. . . . .	79
3.3	Rotor thrust contribution to the overall propulsive thrust for ducted propellers. . . . .	80
3.4	Percentage variation in efficiency for ducted and open propellers. . . . .	80
3.5	Streamlines for duct D2 at different values of the thrust coefficient $C_T$ . . . . .	81
3.6	Wall pressure coefficient for duct D2 at different values of the thrust coefficient $C_T$ . . . . .	81
3.7	Computational domain. . . . .	86
3.8	Open propeller: comparison of the radial (top) and axial (bottom) velocity profiles obtained through the semi-analytical (SAOP-5) and CFD (CFDOP-3) actuator disk methods. . . . .	89
3.9	Open propeller: comparison of the tangential velocity profiles obtained through the semi-analytical (SAOP-5) and CFD (CFDOP-3) actuator disk methods. . . . .	90
3.10	Ducted propeller: comparison of the radial (top) and axial (bottom) velocity profiles obtained through the semi-analytical (SADP-5) and CFD (CFDDP-3) actuator disk methods. . . . .	91

LIST OF FIGURES

3.11	Ducted propeller: comparison of the tangential velocity (top) and of the wall pressure coefficient (bottom) distributions obtained through the semi-analytical (SADP-5) and CFD (CFDDP-3) actuator disk methods. . . . .	92
4.1	Load radial distribution (left) and projection of the generatrices of the stream-tubes onto the meridian plane (right). . .	110
4.2	Radial (top) and axial (bottom) velocity profiles at different axial stations. . . . .	111
4.3	Tangential velocity profiles at different axial stations (top) and distribution of the wall pressure coefficient (bottom). . .	112
4.4	Convergence analysis. . . . .	113
4.5	Nonlinear actuator disk with finite hub (SAHP-5): load radial distribution (left) and streamlines (right). . . . .	115
4.6	Computational domain. Left: full size; right: inner domain. .	118
4.7	Comparison between the wall pressure coefficient profiles obtained with the semi-analytical (SAHP-5) and CFD (CFDHP-3) actuator disk methods. . . . .	119
4.8	Radial (top) and axial (bottom) velocity profiles obtained with the semi-analytical (SAHP-5) and CFD (CFDHP-3) actuator disk methods. . . . .	120
B.1	Computation of the integrals $I_{(-(n+1),n+2,1)}$ through equation (B.16) . . . . .	135
B.2	Computation of the integrals $I_{(-n,n+2,0)}$ through equation (B.16) . . . . .	136
B.3	Computation of the integrals $I_{(-n,n+2,0)}$ through equation (B.16) . . . . .	136

---

## LIST OF TABLES

---

1.1	Propeller ducted with a NACA 4415 profile: geometry and operating conditions. . . . .	22
1.2	Propeller ducted with a NACA 4415 profile with $\hat{b} = 15$ : Number of iterations needed to reach convergence with different loads and relaxation factors $\omega_{rf}$ . . . . .	24
1.3	Propeller ducted with a NACA 4415 profile with $\hat{b} = 15$ : performance coefficients. . . . .	28
1.4	Turbine ducted with a NACA 5415 profile: geometry and operating conditions. . . . .	30
1.5	Turbine ducted with a NACA 5415 profile with $\hat{b} = -2$ and $\lambda = 2\pi$ : performance coefficients. . . . .	39
1.6	Propeller ducted with a NACA 4415 profile with $\hat{b} = 15$ and $J = 0.5$ : performance coefficients. . . . .	39
1.7	Comparison of the open and ducted turbine performance coefficients. . . . .	43
1.8	Comparison of the open and ducted propeller performance coefficients. . . . .	43
1.9	Propeller ducted with a NACA 5415 profile: geometry and operating condition . . . . .	43
2.1	Turbine ducted with a NACA 5415 profile: geometry. . . . .	56

LIST OF TABLES

2.2	Open rotor configuration: numerical parameters and operating condition. . . . .	59
2.3	Open turbine: error analysis. . . . .	60
2.4	Turbine ducted with a NACA 5415 profile: numerical parameters and operating condition. . . . .	60
2.5	Turbine ducted with a NACA 5415: performance coefficients error analysis. . . . .	61
2.6	Turbine ducted with a NACA 5415: axial velocity error analysis. . . . .	61
2.7	Characteristics of the mesh employed in the CFD grid dependence analysis for open turbine. . . . .	61
2.8	Characteristics of the mesh employed in the CFD grid dependence analysis for ducted turbine. . . . .	62
2.9	Open turbine: mesh dependence analysis. . . . .	62
2.10	Turbine ducted with a NACA 5415: mesh dependence analysis. . . . .	62
2.11	$L^2$ discrete norm of the difference between semi-analytical (SAOT-5 and SADT-5) and CFD actuator disk (CFDOT-3 and CFDDT-3) velocity and pressure fields. . . . .	68
3.1	Propeller ducted with a NACA 4415 profile: geometry. . . . .	78
3.2	Propeller ducted with a NACA 4415 profile: main geometrical parameters. . . . .	84
3.3	Open rotor configuration: numerical parameters and operating conditions. . . . .	84
3.4	Propeller ducted with a NACA 4415 profile: numerical parameters and operating conditions. . . . .	84
3.5	Open propeller: error analysis. . . . .	85
3.6	Propeller ducted with a NACA 4415: performance coefficients error analysis. . . . .	85
3.7	Propeller ducted with a NACA 4415: axial velocity error analysis. . . . .	85
3.8	Characteristics of the mesh employed in the CFD grid dependence analysis for open propeller. . . . .	87
3.9	Open propeller: $L^2$ discrete norm of the error. . . . .	87
3.10	Propeller ducted with a NACA 4415: $L^2$ discrete norm of the error. . . . .	87
3.11	Comparison between semi-analytical (SAOP-5 and SADP-5) and CFD actuator disk (CFDOP-3 and CFDDP-3): $L^2$ discrete norm of the error. . . . .	88
4.1	Hub coordinates. . . . .	107

4.2	Semi-analytical actuator disk with finite hub: performance coefficients. . . . .	110
4.3	Semi-analytical actuator disk with finite hub and without slipstream rotation: performance coefficients. . . . .	114
4.4	Nonlinear actuator disk with finite hub: numerical parameters.	116
4.5	Nonlinear actuator disk with finite hub: error analysis. . . . .	116
4.6	Characteristics of the mesh employed in the CFD grid dependence analysis. . . . .	117
4.7	CFD actuator disk: mesh dependence analysis. . . . .	117
4.8	Comparison between semi-analytical (SAHP-5) and CFD (CFDHP-3) actuator disk: $L_2$ discrete norm of the error. . . . .	117



---

## NOMENCLATURE

---

$a_m$	Load polynomial coefficients
$A_n$	Tangential vorticity polynomial coefficients
$A_{rot}$	Area swept by the rotor
$\mathbf{B}$	Vector potential
$\hat{b} = \sigma_{ad}^2 a_1 / U_\infty \Psi_{\sigma_{ad}}$	Dimensionless load magnitude parameter
$b_m$	Load magnitude parameter
$C$	Contour of the duct section
$c, \tilde{c}$	Curvilinear abscissa along the duct section
$\hat{c} = c / \sigma_{ad}$	Dimensionless curvilinear abscissa
$C_P$	Power coefficient
$C_{p,w} = \frac{p - p_\infty}{1/2 \rho U_\infty^2}$	Wall pressure coefficient
$C_T, C_{T,rot}$	Total and rotor thrust coefficients
$C_{T,duct}, C_{T,hub}$	Duct and hub thrust coefficients

LIST OF TABLES

$D$	Rotor diameter
$E$	Complete elliptic integral of the second kind
$G$	Green function
$H$	Bernoulli constant
$H_\infty$	Bernoulli constant at upstream infinity
$\mathcal{H} = \Delta H_{\text{across the disk}}$	Rotor load
$\hat{\mathcal{H}} = 2/U_\infty^2$	Load coefficient
$\hat{H} = 2H/U_\infty^2$	Dimensionless Bernoulli constant
$(\mathbf{i}_\zeta, \mathbf{i}_\sigma, \mathbf{i}_\theta)$	Unit vectors representing the axial, radial and tangential directions
$J$	Advance coefficient
$J$	Jacobian matrix
$J_n$	Bessel function of the first kind and order $n$
$K$	Complete elliptic integral of the first kind
$k(c, \tilde{c}), K(c_m, c_n)$	Coupling coefficients
$L_{(\sigma, \zeta)}$	Linear elliptic operator appearing at the right-hand side of the through-flow governing equation
$\dot{m}$	Mass flow
$M_p$	Number of panels on the duct section
$\mathbf{n}$	Outward unit normal
$n_z$	Number of axial stations
$n_{zs} \times n_{rs}$	Number of axial and radial stations
$P$	Power extracted by the rotor
$p$	Static pressure
$Q_{1/2}$	Legendre function of the second kind and degree 1/2

$\mathbf{T}$	Thrust experienced by the device
$\mathbf{t}$	Unit vector tangent to the duct profile
$T$	Magnitude of the thrust experienced by the device
$\mathbf{T}_{duct}$	Thrust experienced by the duct
$T_{duct}$	Magnitude of the thrust experienced by the duct
$\mathbf{T}_{hub}$	Thrust experienced by the hub
$T_{hub}$	Magnitude of the thrust experienced by the hub
$\mathbf{T}_{rot}$	Thrust experienced by the rotor
$T_{rot}$	Magnitude of the thrust experienced by the rotor
$\mathbf{u}$	Velocity vector
$u, v, w$	Axial, radial and tangential components of the velocity
$u', v'$	Axial and radial components of the velocity induced by a ring vortex
$U_\infty$	Free stream velocity
$\hat{u}, \hat{v}, \hat{w}$	Dimensionless axial, radial and tangential components of the velocity
$\mathbf{u}_a, \mathbf{u}_b$	Velocities just above and beneath the duct vorticity sheet
$u_{ad}, v_{ad}$	Axial and radial components of the velocity induced by the actuator disk wake ring vortex distribution
$u_{ad,m}, v_{ad,m}$	Axial and radial components of the velocity induced by the actuator disk wake ring vortex distribution at the m-th panel
$W$	Work extracted by the rotor
$z, r$	Auxiliary axial and radial coordinates
<b>Greek symbols</b>	

LIST OF TABLES

$\alpha$	Angle between the chord and the axial direction
$\beta(c)$	Local duct profile slope
$\Gamma$	Circulation around the duct
$\Gamma(n)$	Gamma function
$\gamma_{ad}$	Strength density of the actuator disk ring vortex distribution
$\gamma_d$	Strength density of the duct ring vortex distribution
$\gamma_h$	Strength density of the hub ring vortex distribution
$\delta$	Dirac delta function
$\hat{\sigma} = \sigma/\sigma_{ad}$	Dimensionless radial coordinate
$\Delta c_n$	Length of the n-th panel
$\Delta p_{ad}$	Static pressure jump across the disk
$\Delta \hat{p}_{ad} = 2\Delta p_{ad}/\rho U_\infty^2$	Dimensionless static pressure jump across the disk
$\epsilon$	Tip gap
$\zeta, \sigma, \theta$	Axial, radial and tangential coordinates
$\hat{\zeta} = \zeta/\sigma_{ad}$	Dimensionless axial coordinate
$\zeta_{h,LE}$	Hub leading edge axial position
$\zeta_{h,TE}$	Hub trailing edge axial position
$\zeta_{LE}$	Duct leading edge axial position
$\zeta_m, \sigma_m$	Axial and radial coordinate of the control point of the m-th panel
$\zeta_{TE}$	Duct trailing edge axial position
$\eta = C_T/C_P$	Propulsive efficiency
$\kappa$	Single ring vortex strength
$\lambda = \Omega \sigma_{ad}/U_\infty$	Tip speed ratio

$\rho$	Density
$\hat{\sigma} = \sigma/\sigma_{ad}$	Dimensionless radial coordinate
$\sigma_{ad}$	Actuator disk radius
$\sigma_h(\zeta)$	Function describing the hub shape
$\sigma_{LE}$	Duct leading edge radial position
$\sigma_s(\zeta)$	Slipstream edge
$\sigma_{TE}$	Duct trailing edge radial position
$\Psi$	Stokes stream function
$\Psi'$	Stokes stream function induced by a ring vortex
$\Psi_0$	Stokes stream function on the duct
$\Psi_{ad}$	Stokes stream function evaluated at ( $\zeta = 0, \sigma = \sigma_{ad}$ )
$\Psi_d$	Stokes stream function induced by the duct ring vortex distribution and by the free stream
$\Psi_h$	Stokes stream function induced by the hub ring vortex distribution and by the free stream
$\boldsymbol{\omega} = (\omega_\zeta, \omega_\sigma, \omega_\theta)$	Vorticity vector
$\Omega$	Turbine angular velocity
$\omega_{rf}$	Relaxation factor
<b>Mathematical symbols</b>	
$\nabla$	Gradient operator
$\nabla \cdot$	Divergence operator
$\nabla \times$	Curl operator
$\nabla^2$	Laplace operator
<b>Acronyms</b>	
CFDDP	CFD actuator disk method for a ducted propeller

LIST OF TABLES

CFDDT	CFD actuator disk method for a ducted turbine
CFDHP	CFD actuator disk method for a propeller with finite hub
CFDOP	CFD actuator disk method for a open propeller
CFDOT	CFD actuator disk method for a open turbine
SADP	Semi-analytical actuator disk method for a ducted propeller
SADT	Semi-analytical actuator disk method for a ducted turbine
SAHP	Semi-analytical actuator disk method for a propeller with finite hub
SAOP	Semi-analytical actuator disk method for a open propeller
SAOT	Semi-analytical actuator disk method for a open turbine

# CHAPTER 1

---

## EXACT SOLUTION OF THE FLOW OVER A NON-UNIFORM HEAVILY LOADED DUCTED ACTUATOR DISK

---

### 1.1 Introduction

The concept of inserting a rotor into a duct is already very old, and it is currently used in the fields of propulsion and energy conversion systems for marine, wind and aeronautical applications. On general grounds, the duct enhances the performance of the coupled system by increasing either the efficiency of a heavily loaded propeller or the energy output of a turbine. Other applications aim at improving the cavitation behaviour of marine propellers.

Most of the theoretical investigations on ducted rotors are based on the combined use of several representations of the velocity field induced by the duct with that generated by the rotor, typically modelled by the lifting line, the lifting surface or the boundary element methods. Remarkable applications are due to Ryan and Glover (1972), Kerwin, Kinna, et al. (1987), Baltazar and Falcão de Campos (2009) and Çelik, Güner, and Ekinçi (2010), but this list should not be regarded as exhaustive. A more thorough literature review can be found in the textbooks of Carlton (2007) and Breslin

and Andersen (1994). Not disregarding the computationally intensive 3D unsteady computational fluid dynamics (CFD) based methods, in many applications the rotor is still modelled as a linearised actuator disk (Conway 1995; Horlock 1978) with spanwise variable load or its nonlinear generalized variant (Conway 1998; Greenberg and Powers 1970; Wu 1962). Dickmann and Weissinger (1955) modelled a ducted propeller representing the duct with an elliptical distribution of ring vortices lying on a cylinder of constant radius and the propeller by an actuator disk of constant load. Chaplin (1964) and Van Gunsteren (1973) investigated the effects of the slipstream contraction on the duct performance using simplified actuator disk models. Gibson and Lewis (1973) modelled a ducted propeller by coupling an actuator disk with a surface vorticity method. Although the rotation effects and the slipstream contraction were neglected, the duct was more closely represented by the localized surface vorticity distribution, compared to the thin airfoil theory. Falcão de Campos (1983) calculated the axisymmetric flow through a ducted actuator disk in a wake using a discrete vortex sheet method.

The purpose of this first chapter is to extend the nonlinear actuator disk theory of Conway (1998) to ducted rotors in order to better fulfil the design and analysis needs for marine, wind and aeronautical applications (see also Bontempo and Manna (2013) and Bontempo, Cardone, et al. (2014)). In more detail, an exact solution of the inviscid axisymmetric flow generated by a heavily loaded ducted rotor accounting for the proper shape of the slipstream, whether converging or diverging, is sought. Ideally, the solution procedure should be cost-effective, and capable of handling arbitrary load radial distributions, rotor wake rotation and ducts of general shape and thickness distribution.

This chapter has been organized as follows. After this short introduction, in §1.2 and §1.3 the models and the associated solutions for the open rotor and the duct-alone flows are detailed. In §1.4 the differential problem governing the coupled flow is described; finally in §1.5 and §1.6 the solution procedure and the results are presented.

## 1.2 The open rotor flow model

In order to simulate an open rotor and its vortical wake, consider the incompressible, steady and axisymmetric flow of an effectively inviscid fluid with vorticity through an actuator disk with center at the origin of a cylindrical coordinate system  $(\zeta, \sigma, \theta)$ , radius  $\sigma_{ad}$  and immersed in a free-stream with

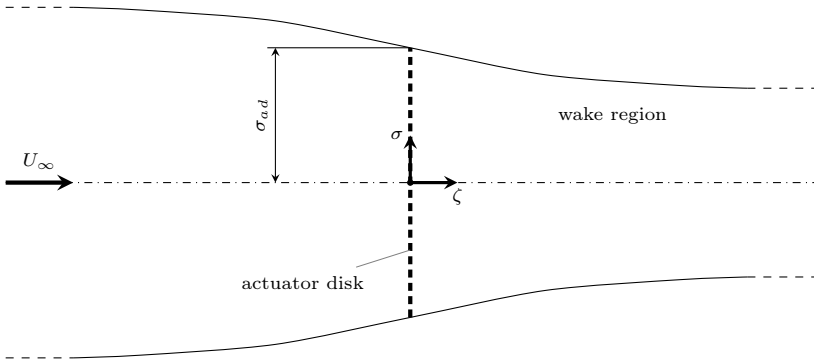


Figure 1.1: Schematic view of the actuator disk geometrical configuration.

velocity  $U_\infty$  in the positive  $\zeta$ -axis direction (see Figure 1.1).

Preliminarily, focus on the characteristics of a general axisymmetric flow. As is customary when dealing with this class of problems, it is convenient to introduce the Stokes stream function  $\Psi$ , so that the mass-conservation equation is automatically satisfied. For the above flows, the velocity vector field  $\mathbf{u} = (u, v, w)$  can be expressed in terms of a vector potential  $\mathbf{B}$  through  $\mathbf{u} = \nabla \times \mathbf{B}$ , with  $B_\theta = \Psi/\sigma$ . If  $\nabla \cdot (\nabla \cdot \mathbf{B}) = \mathbf{0}$  then  $\mathbf{B}$  satisfies the equation (Batchelor 1967)

$$\nabla^2 \mathbf{B} = -\boldsymbol{\omega}, \quad (1.1)$$

with  $\boldsymbol{\omega}$  the vorticity vector

$$\boldsymbol{\omega} = (\omega_\zeta, \omega_\sigma, \omega_\theta) = \left( \frac{1}{\sigma} \frac{\partial(\sigma w)}{\partial \sigma}, -\frac{\partial w}{\partial \zeta}, \frac{\partial v}{\partial \zeta} - \frac{\partial u}{\partial \sigma} \right). \quad (1.2)$$

The  $\theta$  component of (1.1) is equivalent to (Batchelor 1967; Wu 1962)

$$L_{(\sigma, \zeta)} \left( \frac{\Psi}{\sigma} \right) = \sigma \left( \frac{\partial^2}{\partial \sigma^2} + \frac{1}{\sigma} \frac{\partial}{\partial \sigma} - \frac{1}{\sigma^2} + \frac{\partial^2}{\partial \zeta^2} \right) \frac{\Psi}{\sigma} = \frac{\partial^2 \Psi}{\partial \sigma^2} - \frac{1}{\sigma} \frac{\partial \Psi}{\partial \sigma} + \frac{\partial^2 \Psi}{\partial \zeta^2} = -\omega_\theta \sigma. \quad (1.3)$$

Actually, since  $\nabla \cdot (\nabla \cdot \mathbf{B}) \cdot \mathbf{i}_\theta = 0$  for axisymmetric flow, equation (1.3) is always valid in this case. Alternatively, equation (1.3) can be found simply by substituting the axial and radial velocity expressions in terms of the Stokes stream function in the definition of  $\omega_\theta$ .

Neglecting body forces, the momentum equation for steady, incompressible and inviscid flows can be written as

$$\mathbf{u} \times \boldsymbol{\omega} = \nabla H, \quad (1.4)$$

where  $H = p/\rho + \frac{1}{2}(u^2 + v^2 + w^2)$  is the Bernoulli constant. The above equation can be used to manipulate the vorticity field appearing on the right-hand side of (1.1) or (1.3). In particular, from (1.4) it follows that  $\mathbf{u} \cdot \nabla H = 0$ , and therefore  $H$  is constant along a streamline and it is a function of  $\Psi$  alone, i.e.  $H = H(\Psi)$ . Thus using the chain rule:

$$\nabla H = \nabla_{(\Psi)} H \mathbf{J}_{\Psi} = \frac{dH}{d\Psi} \nabla \Psi, \quad (1.5)$$

where  $\nabla_{(\Psi)} H$  and  $\mathbf{J}_{\Psi}$  are the gradient of  $H$  in the direction of  $\Psi$  and the Jacobian matrix of  $\Psi$ , respectively. Therefore equation (1.4) becomes

$$\mathbf{u} \times \boldsymbol{\omega} = \frac{dH}{d\Psi} \nabla \Psi. \quad (1.6)$$

Furthermore, it can be shown that the product  $\sigma w$  is a function of  $\Psi$  alone too (Wu 1962). In fact, the flow being axisymmetric, the theta component of equation (1.4) reduces to

$$u\omega_{\sigma} - v\omega_{\zeta} = \frac{1}{\sigma} \frac{dH}{d\theta} = 0.$$

Substituting the vorticity definition (1.2), the above equation becomes

$$u \frac{\partial(\sigma w)}{\partial \zeta} + v \frac{\partial(\sigma w)}{\partial \sigma} = 0,$$

which, by means of the axisymmetric flow assumption, can be cast in the form

$$\mathbf{u} \cdot \nabla(\sigma w) = 0.$$

The previous equation states that the product  $\sigma w$  is constant along a streamline and thus that  $\sigma w$  is a function of  $\Psi$  alone.

To compute the tangential vorticity appearing at the right-hand side of (1.3), it suffices to evaluate the cross-product between  $\mathbf{u}$  and equation (1.6) thus obtaining

$$[v(u\omega_{\sigma} - v\omega_{\zeta}) - w(w\omega_{\zeta} - u\omega_{\theta})] \mathbf{i}_{\zeta} = -\sigma w \frac{dH}{d\Psi} \mathbf{i}_{\zeta}, \quad (1.7a)$$

$$[w(v\omega_{\theta} - w\omega_{\sigma}) - u(u\omega_{\sigma} - v\omega_{\zeta})] \mathbf{i}_{\sigma} = -\sigma v w \frac{dH}{d\Psi} \mathbf{i}_{\sigma}, \quad (1.7b)$$

$$[u(w\omega_{\zeta} - u\omega_{\theta}) - v(v\omega_{\theta} - w\omega_{\sigma})] \mathbf{i}_{\theta} = \sigma(u^2 + v^2) \frac{dH}{d\Psi} \mathbf{i}_{\theta}. \quad (1.7c)$$

With some remarkable algebra, equation (1.7c) yields

$$-\omega_\theta\sigma = \sigma^2 \frac{dH}{d\Psi} - \sigma w \frac{d\sigma w}{d\Psi}.$$

With the help of the above equation, (1.7b) and (1.7c) return

$$\omega_\zeta = u \frac{d(\sigma w)}{d\Psi}, \quad \omega_\sigma = v \frac{d(\sigma w)}{d\Psi}.$$

Summarizing the above results, the vorticity vector filed  $\boldsymbol{\omega}$  can be expressed as

$$\boldsymbol{\omega} = (\omega_\zeta, \omega_\sigma, \omega_\theta) = \left( u \frac{d(\sigma w)}{d\Psi}, v \frac{d(\sigma w)}{d\Psi}, w \frac{d(\sigma w)}{d\Psi} - \sigma \frac{dH}{d\Psi} \right). \quad (1.8)$$

Recalling that the main objective is to simulate the axisymmetric flow induced by an open rotor and its vortical wake through an actuator disk, and keeping in mind that (1.3) is the governing equation to be solved, it is necessary to express the azimuthal component of the vorticity field  $\omega_\theta(\zeta, \sigma)$  as a function of the load radial distribution  $\mathcal{H}(\Psi) = \Delta H_{\text{across the disk}} = H(\Psi)|_{(\zeta>0, \sigma<\sigma_s(\zeta))} - H_\infty$  at the disk. In the previous relation, the quantity  $\sigma_s(\zeta)$  denotes the outer edge of the wake. Since outside the slipstream  $H = H_\infty$ , and inside it,  $H(\Psi)|_{(\zeta>0, \sigma<\sigma_s(\zeta))} \neq H_\infty$ , in the foregoing the subscript  $(\zeta > 0, \sigma < \sigma_s(\zeta))$  will be omitted when referring to  $H(\Psi)$ . Because  $\mathcal{H}(\Psi)$  is a single-valued composite function of  $\Psi$ , although defined at the disk, it can be used everywhere in the slipstream. With the help of the angular momentum equation,  $\mathcal{H}(\Psi)$  can be written as

$$\mathcal{H}(\Psi) = H(\Psi) - H_\infty = \Omega\sigma w, \quad (1.9)$$

where  $\Omega$  is the angular velocity of the rotor. Finally, using (1.9) in (1.8), the  $\theta$ -component of the vorticity can be expressed as

$$-\omega_\theta\sigma = \begin{cases} \frac{\Omega^2\sigma^2 - \mathcal{H}}{\Omega^2} \frac{d\mathcal{H}}{d\Psi} & \text{inside the slipstream,} \\ 0 & \text{outside the slipstream.} \end{cases} \quad (1.10)$$

Thus substituting (1.10) into (1.3) yields the following nonlinear partial differential equation with the associated conditions at infinity (Wu 1962):

$$L_{(\sigma, \zeta)} \left( \frac{\Psi}{\sigma} \right) = \begin{cases} \frac{\Omega^2\sigma^2 - \mathcal{H}}{\Omega^2} \frac{d\mathcal{H}}{d\Psi} & \text{inside the slipstream,} \\ 0 & \text{outside the slipstream,} \end{cases} \quad (1.11)$$

$$\frac{1}{\sigma} \frac{\partial \Psi}{\partial \sigma} \rightarrow U_\infty, \quad \frac{\partial \Psi}{\partial \zeta} \rightarrow 0 \quad \text{as } \zeta \rightarrow -\infty \quad \text{or } \sigma \rightarrow \infty, \quad (1.12a)$$

$$\frac{\partial \Psi}{\partial \zeta} \rightarrow 0 \quad \text{as } \zeta \rightarrow +\infty, \quad (1.12b)$$

valid outside the disk. To complete the formulation of problem (1.11)-(1.12), the load distribution at the disk  $\mathcal{H}(\Psi)$  and the angular velocity  $\Omega$  have to be prescribed. However, the slipstream location  $\sigma_s(\zeta)$ , defining the domain region inside which the right-hand side of (1.11) does not vanish, is not known in advance and must be determined as part of the solution. For flows without swirl, that is, whenever the azimuthal velocity component  $w(\zeta, \sigma)$  is zero in the wake region, the through-flow velocities  $u(\zeta, \sigma)$  and  $v(\zeta, \sigma)$  can be computed by solving problem (1.11)-(1.12) in terms of the Stokes stream function  $\Psi$ . Conversely, for swirled flows, the azimuthal velocity has to be computed using equation (1.9). It is worth noting that, for prescribed  $\mathcal{H}(\Psi)$  and  $\Omega$ , problem (1.11)-(1.12) is fully decoupled from (1.9), and  $w(\zeta, \sigma)$  can be evaluated from the field values of  $\Psi(\zeta, \sigma)$ .

Since  $L_{(\zeta, \sigma)}$  is a linear operator, the differential equation (1.11) can be converted into the following nonlinear integral equation:

$$\frac{\Psi(\zeta, \sigma)}{\sigma} = \int_0^\infty \int_0^{\sigma_s(z)} G(\sigma, r, \zeta - z) \omega_\theta(z, r) r \, dr \, dz + q(\zeta, \sigma), \quad (1.13)$$

where  $q(\zeta, \sigma)$  is a solution of  $L_{(\zeta, \sigma)}\{q(\zeta, \sigma)\} = 0$ . In (1.13),  $G(\sigma, r, \zeta - z)$  is the Green function of the operator  $L_{(\zeta, \sigma)}$  and satisfies

$$L_{(\zeta, \sigma)}\{G(\sigma, r, \zeta - z)\} = -\delta(\sigma - r)\delta(\zeta - z), \quad (1.14)$$

where  $\delta$  is the Dirac delta function. From the conditions (1.12), it follows that  $q(\zeta, \sigma) = U_\infty \sigma / 2$  and  $G(\sigma, r, \zeta - z)$  vanishes at infinity. A solution can be obtained by applying to (1.14) the Hankel transform with respect to  $\sigma$  (see Appendix A):

$$G(\sigma, r, \zeta - z) = \frac{1}{2} \int_0^\infty e^{-s|\zeta - z|} J_1(sr) J_1(s\sigma) \, ds, \quad (1.15)$$

where  $J_1$  is the Bessel function of the first kind. Finally, substituting (1.15) in (1.13), the solution of the problem (1.11)-(1.12) reduces to

$$\frac{\Psi(\zeta, \sigma)}{\sigma} = \frac{1}{2} \int_0^\infty \int_0^{\sigma_s(z)} \int_0^\infty e^{-s|\zeta - z|} \omega_\theta(z, r) r J_1(sr) J_1(s\sigma) \, ds \, dr \, dz + \frac{U_\infty \sigma}{2}. \quad (1.16)$$

Since the only non-zero component of the vorticity of the axisymmetric field  $(u, v, 0)$  is  $\omega_\theta$  (see (1.2)), an alternative solution strategy for the problem (1.11)-(1.12) is based on the description of the wake by a continuous distribution of ring vortices with axis parallel to the  $\zeta$ -axis. To show the above, consider the stream function and velocity field induced by a single ring vortex of radius  $r$ , strength  $\kappa$  and located at  $\zeta = z$  and  $\sigma = 0$ , given by (Basset 1888; Lamb 1932)

$$\frac{\Psi'(\zeta, \sigma)}{\sigma} = \frac{\kappa r}{2} \int_0^\infty e^{-s|\zeta-z|} J_1(sr) J_1(s\sigma) ds, \quad (1.17)$$

$$u'(\zeta, \sigma) = \frac{\kappa r}{2} \int_0^\infty e^{-s|\zeta-z|} s J_1(sr) J_0(s\sigma) ds, \quad (1.18)$$

$$v'(\zeta, \sigma) = \pm \frac{\kappa r}{2} \int_0^\infty e^{-s|\zeta-z|} s J_1(sr) J_1(s\sigma) ds, \quad (1.19)$$

where the positive sign is for  $\zeta - z \geq 0$  and vice versa. This simple flow solution can be used to reproduce a vortical region, like the wake. To this aim, it is necessary to introduce a continuum surface singularity distribution covering the space region bounded by the disk and the slipstream  $\sigma_s(\zeta)$ . Defining  $\gamma_{ad}(\zeta, \sigma)$  as the ring vortex density strength and integrating equations (1.17), (1.18) and (1.19) over the wake leads to the following expressions:

$$\frac{\Psi(\zeta, \sigma)}{\sigma} = \frac{1}{2} \int_0^\infty \int_0^{\sigma_s(z)} \int_0^\infty e^{-s|\zeta-z|} \gamma_{ad}(z, r) r J_1(sr) J_1(s\sigma) ds dr dz + \frac{U_\infty \sigma}{2}, \quad (1.20)$$

$$u_{ad}(\zeta, \sigma) = \frac{1}{2} \int_0^\infty \int_0^{\sigma_s(z)} \int_0^\infty e^{-s|\zeta-z|} \gamma_{ad}(z, r) sr J_1(sr) J_0(s\sigma) ds dr dz, \quad (1.21)$$

$$v_{ad}(\zeta, \sigma) = \pm \frac{1}{2} \int_0^\infty \int_0^{\sigma_s(z)} \int_0^\infty e^{-s|\zeta-z|} \gamma_{ad}(z, r) sr J_1(sr) J_1(s\sigma) ds dr dz. \quad (1.22)$$

The density function  $\gamma_{ad}(\zeta, \sigma)$  has to be capable of reproducing the vorticity field  $\omega_\theta(\zeta, \sigma)$  imposed by the disk load distribution  $\mathcal{H}(\Psi)$ . Comparing equation (1.16) and (1.20), it is readily understood that equation (1.20) satisfies problem (1.11)-(1.12) whenever (Conway 1998)

$$\gamma_{ad}(\zeta, \sigma) = \omega_\theta(\zeta, \sigma). \quad (1.23)$$

In conclusion, once the load distribution  $\mathcal{H}(\Psi)$  and the angular velocity  $\Omega$  have been chosen, the through-flow can be described by a ring vortex distribution of strength  $\gamma_{ad}(\zeta, \sigma) = \omega_\theta(\zeta, \sigma)$ , while the tangential velocity is given by (1.9).

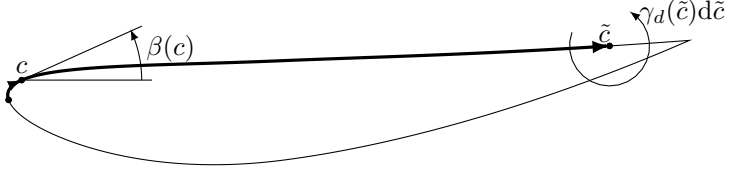


Figure 1.2: Schematic view and nomenclature used for the duct ring vortex distribution.

### 1.3 The duct alone flow model

As anticipated in §1.1, the main task of the duct is to enhance the performance of the rotor whether it operates as a propeller or as a turbine. It is generally a slender lifting element defining a contoured axisymmetric channel inside which the rotor is installed.

Following the classical approach of Martensen (1959), later elaborated by Jacob and Riegels (1963), Wilkinson (1967a, 1967b) and Nyiri and Baranyi (1983), the inviscid flow around an axisymmetric duct of general shape is assumed to be described by a sheet of ring vorticity whose density strength  $\gamma_d$  makes the duct boundary a stream surface (see Figure 1.2). An extensive description of the method and many related applications can be found in Lewis (1991) and references therein. Only the key elements of the procedure are summarized hereafter.

Since the flow at zero incidence around an annular body with contour  $C$  is axisymmetric, it is again convenient to introduce a cylindrical coordinate system  $(\zeta, \sigma, \theta)$ . The objective is to determine the density strength  $\gamma_d$  that satisfies the appropriate velocity boundary condition along solid walls, i.e.  $\mathbf{u} \cdot \mathbf{n} = 0$ , with  $\mathbf{n}$  the outward unit normal. In turn, the  $\gamma_p$  distribution is related to the circulation around the duct by

$$\Gamma = \oint_C \gamma_d(c) dc. \quad (1.24)$$

which controls the amount of lift around the duct cross-section. In (1.24),  $c$  is the curvilinear abscissa measured clockwise from the leading edge (see Figure 1.2).

It can be shown (see e.g. Lewis (1991); Anderson (2001)) that  $\gamma_d$  is also the jump in the tangential velocity across the vortex sheet

$$\gamma_d(c) = (\mathbf{u}_a(c) - \mathbf{u}_b(c)) \cdot \mathbf{t}, \quad (1.25)$$

where  $\mathbf{t}$  is the unit vector tangent to the duct profile, and  $\mathbf{u}_a$  and  $\mathbf{u}_b$  are the velocities just above and beneath the vorticity sheet, respectively. Moreover, it can be further shown (Lewis 1991; Martensen 1959) that the no-penetration requirement along the solid wall is satisfied by the homogeneous Dirichlet boundary condition on the tangent to the wall velocity just beneath the vorticity sheet  $\mathbf{u}_b(c)$ , provided there are no vortex or source distributions within the profile. Using the homogeneous Dirichlet boundary condition in equation (1.25), it follows that the solution  $\gamma_d$  equals the velocity parallel to the annular surface just above the sheet.

In more detail, the  $\gamma_d(c)$  distribution can be computed by solving the following Fredholm integral equation of the second kind (Lewis 1991):

$$-\frac{1}{2}\gamma_d(c) + \oint_C k(c, \tilde{c})\gamma_d(\tilde{c}) d\tilde{c} + U_\infty \cos \beta(c) = 0. \quad (1.26)$$

In the above equation,  $\beta(c)$  is the local profile slope and  $k(c, \tilde{c})$  is the velocity parallel to the surface, at  $c$ , induced by a ring vortex of unit strength located at  $\tilde{c}$ . The first term in (1.26) is precisely half the velocity jump across the sheet, the second is the velocity induced in  $c$  by all the duct vortices, and the third is the contribution of  $U_\infty$  in the tangent to the wall direction.

A classical result of the potential flow theory is that for a given body there is an infinite number of valid theoretical solutions, one for each value of the total circulation  $\Gamma$ . Therefore, the method discussed above for the description of the flow around an annular wing must be complemented by an additional condition fixing  $\Gamma$ . In order to mimic the lifting behaviour induced by the viscosity in the inviscid formulation, the circulation  $\Gamma$  has to make the flow leave the duct smoothly at the trailing edge, according to the well-known Kutta condition. In conclusion, the  $\gamma_d(c)$  distribution has to satisfy (1.26) and the Kutta condition at the trailing edge as well.

It is worth noting that an equivalent formulation of the present problem in terms of the stream function  $\Psi_d$  induced by the duct ring vortex sheet is obtained by associating the conditions at infinity and the no-penetration requirement along the solid wall contour  $C$  to the elliptic equation (1.3) having set its rhs to zero:

$$L_{(\sigma, \zeta)} \left( \frac{\Psi_d}{\sigma} \right) = 0, \quad (1.27)$$

$$\frac{1}{\sigma} \frac{\partial \Psi_d}{\partial \sigma} \rightarrow U_\infty, \quad \frac{\partial \Psi_d}{\partial \zeta} \rightarrow 0 \quad \text{at infinity}, \quad (1.28a)$$

$$\Psi_d = \Psi_0 = \text{const.} \quad \text{on } C. \quad (1.28b)$$

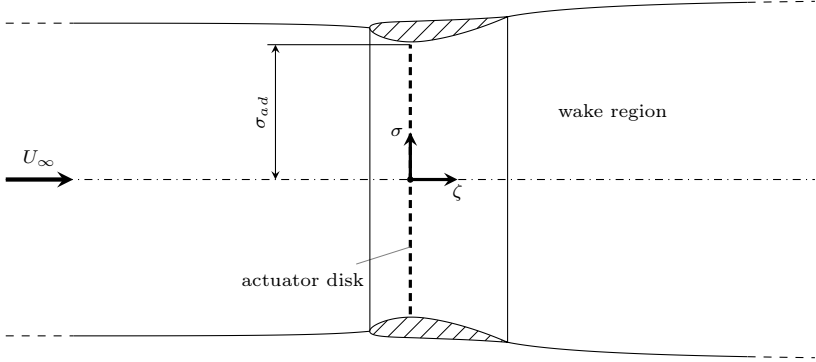


Figure 1.3: Schematic view of the ducted rotor geometrical configuration.

Owing to the linearity of problem (1.27)-(1.28), its solution can be expressed as the superposition of an infinite number of ring vortices (eq. 1.17) forming a sheet:

$$\frac{\Psi_d(\zeta, \sigma)}{\sigma} = \frac{1}{2} \oint_C \int_0^\infty \gamma_d(c) r(c) e^{-s|\zeta-z|} J_1(sr(c)) J_1(s\sigma) ds dc + \frac{U_\infty \sigma}{2}, \quad (1.29)$$

Clearly, in the above equation, the  $\gamma_d(c)$  distribution has to satisfy the boundary condition (1.26) and the Kutta condition.

## 1.4 The coupled flow model

With the assumptions adopted in §1.2 and §1.3, the differential problem (1.11)-(1.12) applies as well to the case of a ducted rotor (see Figure 1.3), provided the appropriate no-penetration boundary condition on the profile is enforced:

$$L_{(\zeta, \sigma)} \left( \frac{\Psi}{\sigma} \right) = \begin{cases} \frac{\Omega^2 \sigma^2 - \mathcal{H}}{\Omega^2} \frac{d\mathcal{H}}{d\Psi} & \text{inside the slipstream,} \\ 0 & \text{outside the slipstream,} \end{cases} \quad (1.30)$$

$$\frac{1}{\sigma} \frac{\partial \Psi}{\partial \sigma} \rightarrow U_\infty, \quad \frac{\partial \Psi}{\partial \zeta} \rightarrow 0 \quad \text{as } \zeta \rightarrow -\infty \quad \text{or } \sigma \rightarrow \infty, \quad (1.31a)$$

$$\frac{\partial \Psi}{\partial \zeta} \rightarrow 0 \quad \text{as } \zeta \rightarrow +\infty, \quad (1.31b)$$

$$\Psi = \Psi_0 = \text{const.} \quad \text{on } C. \quad (1.31c)$$

Comparing (1.30)-(1.31) with (1.11)-(1.12), an additional difficulty arises, in that a new boundary condition has to be satisfied. Similarly to the slipstream position  $\sigma_s(\zeta)$ , the unknown value  $\Psi_0$  has also to be evaluated as part of the solution. The solution of (1.30)-(1.31) in terms of stream function can again be expressed in the form (1.13), with an appropriate value of  $q(\zeta, \sigma)$  according to the new boundary condition (1.31c). As already stated,  $\Psi_d$  satisfies  $L_{(\zeta, \sigma)}\{\Psi_d(\zeta, \sigma)/\sigma\} = 0$  and the associated conditions at infinity. Therefore,  $q(\zeta, \sigma)$  coincides with  $\Psi_d(\zeta, \sigma)/\sigma$ , provided the density strength vortex distribution  $\gamma_d$  is computed by enforcing on the duct boundary the no-penetration condition. Owing to the presence of the actuator disk, the latter condition can be expressed as

$$-\frac{1}{2}\gamma_d(c) + \oint_C k(c, \tilde{c})\gamma_d(\tilde{c}) d\tilde{c} + (U_\infty + u_{ad}(c))\cos\beta(c) + v_{ad}(c)\sin\beta(c) = 0. \quad (1.32)$$

Equation (1.32) is equivalent to (1.26) except for the presence of the  $u_{ad}(c)$  and  $v_{ad}(c)$  terms representing the velocities induced by the actuator disk at  $c$  on the profile, evaluated through (1.21)-(1.22). Finally, the coupled flow solution corresponding to (1.20), using (1.29), reads

$$\begin{aligned} \frac{\Psi(\zeta, \sigma)}{\sigma} = & \frac{1}{2} \int_0^\infty \int_0^{\sigma_s(z)} \int_0^\infty e^{-s|\zeta-z|} \gamma_{ad}(z, r) r J_1(sr) J_1(s\sigma) ds dr dz + \\ & \underbrace{\frac{1}{2} \oint_C \int_0^\infty \gamma_d(c) r(c) e^{-s|\zeta-z|} J_1(sr(c)) J_1(s\sigma) ds dc + \frac{U_\infty \sigma}{2}}_{\frac{\Psi_d(\zeta, \sigma)}{\sigma}}. \end{aligned} \quad (1.33)$$

Comparing (1.20) and (1.33) it turns out that, in addition to the terms associated with the wake ring vortex distribution and to the free stream, a new contribution to the stream function, provided by the duct ring vortex sheet, appears. Similarly to (1.20), equation (1.33) represents the exact flow solution of the coupled problem.

## 1.5 Solution strategy

In §1.4 it has been shown that (1.33) is the exact coupled flow solution in the whole field. However, the direct evaluation of  $\Psi$  via (1.33) is prevented due to the implicitness of the solution. The implicitness is three-fold. Firstly,

the slipstream location  $\sigma_s(\zeta)$  depends upon the stream function field  $\Psi$  and moreover it is unknown. Secondly, the unknown density strength  $\gamma_{ad}$ , or else the angular component of the vorticity (see equation (1.23)), is also a function of the disk load  $\mathcal{H}(\Psi)$  and thus of  $\Psi$ . Thirdly, differently from the open rotor formulation, the new term  $\Psi_d$  itself depends upon  $\Psi$  through  $u_{ad,m}$  and  $v_{ad,m}$ .

One way to approach the problem consists in specifying a priori the load distribution at the disk in terms of  $\Psi$ , since by so doing the  $\gamma_{ad}$  or else  $\omega_\theta$  in (1.33) can also be expressed as a function of  $\Psi$  through (1.10). Assuming now that the load is a continuous function, a suitable polynomial approximation to arbitrary accuracy is (Conway 1998)

$$\mathcal{H}(\Psi) = \sum_{m=0}^M a_m \left( \frac{\Psi}{\Psi_{\sigma_{ad}}} \right)^m, \quad (1.34)$$

where  $\Psi_{\sigma_{ad}}$  is the stream function evaluated at  $(\zeta = 0, \sigma = \sigma_{ad})$ . It can be simply proved that  $\mathcal{H}(0) = a_0$  and, if the load distribution falls to zero at the slipstream edge, i.e.  $\mathcal{H}(\Psi_{\sigma_{ad}}) = 0$ , then  $\sum_{m=0}^M a_m = 0$ . Obviously, if  $\mathcal{H}(0) = 0$ , then  $\sum_{m=1}^M a_m = 0$ . Using (1.34) and further assuming the load  $\mathcal{H}(\Psi)$  to be  $C^1$  continuous, the  $\theta$  component of the vorticity inside the slipstream (eq. (1.10)) becomes

$$\frac{\omega_\theta(\zeta, \sigma)}{\sigma} = \left[ \frac{J^2}{\pi^2 U_\infty^2} \left( \frac{\sigma_{ad}}{\sigma} \right)^2 \sum_{m=0}^M a_m \left( \frac{\Psi}{\Psi_{\sigma_{ad}}} \right)^m - 1 \right] \sum_{m=1}^M \frac{m a_m}{\Psi_{\sigma_{ad}}} \left( \frac{\Psi}{\Psi_{\sigma_{ad}}} \right)^{m-1}. \quad (1.35)$$

In the above equation, the advance coefficient  $J$  is defined as  $J = U_\infty/nD$ , where  $D$  is the rotor diameter and  $n$  is the rotational speed. The advance coefficient  $J$  is typically used in the propeller field, while the tip speed ratio  $\lambda = \Omega\sigma_{ad}/U_\infty$  is the typical turbine rotation parameter. The previous and the following equations can be expressed in terms of  $\lambda$  simply by substituting  $J = \pi/\lambda$ . In view of the exact integration of (1.33), it is convenient to express the tangential vorticity as a function of  $\sigma$  and  $\zeta$ , a task that can be accomplished using the following polynomial expansion (Conway 1998):

$$\frac{\omega_\theta(\zeta, \sigma)}{\sigma} = \sum_{n=0}^N A_n(\zeta) \left[ 1 - \left( \frac{\sigma}{\sigma_s(\zeta)} \right)^2 \right]^n. \quad (1.36)$$

Evaluating (1.35) and (1.36) along the slipstream edge, it can be readily shown that the value of the first coefficient in (1.35) is  $A_0 = -\sum_{m=1}^M m a_m / \Psi_{\sigma_{ad}}$ .

With the help of equations (1.23) and (1.36), the Stokes stream function (1.33) can be expressed as

$$\frac{\Psi(\zeta, \sigma)}{\sigma} = \frac{\Psi_d(\zeta, \sigma)}{\sigma} + \frac{1}{2} \int_0^\infty \int_0^{\sigma_s(z)} \int_0^\infty \sum_{n=0}^N A_n(z) \left[ 1 - \left( \frac{r}{\sigma_s(z)} \right)^2 \right]^n r^2 J_1(sr) J_1(s\sigma) e^{-s|\zeta-z|} ds dr dz$$

which, making use of the linearity property of integration, returns

$$\frac{\Psi(\zeta, \sigma)}{\sigma} = \frac{\Psi_d(\zeta, \sigma)}{\sigma} + \frac{1}{2} \int_0^\infty \int_0^\infty J_1(s\sigma) e^{-s|\zeta-z|} \left\{ \sum_{n=0}^N A_n(z) \int_0^{\sigma_s(z)} r^2 \left[ 1 - \left( \frac{r}{\sigma_s(z)} \right)^2 \right]^n J_1(sr) dr \right\} ds dz$$

Applying the change of variable  $x = r/\sigma_s(z)$  to the above equation, the radial integral can be cast in the form

$$\int_0^1 x^{\nu+1} (1-x^2)^\mu J_\nu(bx) dx = 2^\mu \Gamma(\mu+1) b^{-(\mu+1)} J_{\nu+\mu+1}(b), \quad (1.37)$$

whose exact solution, appearing on the right-hand side of (1.37), is due to Sonine (1880). Moreover, in equation (1.37)  $\Gamma$  is the Gamma function.

With the help of (1.23), equations (1.33) becomes

$$\Psi(\zeta, \sigma) = \sigma \int_0^\infty \sum_{n=0}^N A_n(z) 2^{n-1} n! \sigma_s^{2-n}(z) I_{(-n+1, n+2, 1)}(\sigma_s(z), \sigma, \zeta-z) dz + \Psi_d(\zeta, \sigma), \quad (1.38)$$

Following the same analytical procedure to equations (1.21) and (1.22), the following expressions for the axial and radial velocity induced by the actuator disk wake ring vortex distribution can be found:

$$u_{ad}(\zeta, \sigma) = \int_0^\infty \sum_{n=0}^N A_n(z) 2^{n-1} n! \sigma_s^{2-n}(z) I_{(-n, n+2, 0)}(\sigma_s(z), \sigma, \zeta-z) dz, \quad (1.39)$$

$$v_{ad}(\zeta, \sigma) = \pm \int_0^\infty \sum_{n=0}^N A_n(z) 2^{n-1} n! \sigma_s^{2-n}(z) I_{(-n, n+2, 1)}(\sigma_s(z), \sigma, \zeta-z) dz. \quad (1.40)$$

The integrals  $I_{(\xi,\mu,\nu)}$  appearing in (1.38)-(1.40), with  $\xi$ ,  $\mu$  and  $\nu$  integers, are of the type:

$$I_{(\xi,\mu,\nu)} = \int_0^\infty e^{-s|\zeta-z|} s^\xi J_\mu(sr) J_\nu(s\sigma) ds$$

and can be expressed in terms of complete elliptic integrals and the Heuman Lambda function through the recursive scheme detailed in Appendix B.

Furthermore, equation (1.38) requires the evaluation of the duct contribution  $\Psi_d(\zeta, \sigma)$  through (1.29). As anticipated, the density strength  $\gamma_d(c)$  appearing in (1.29) has to be computed by making the duct boundary a stream surface. In the coupled flow case, this is obtained by satisfying (1.32), as explained in §1.4. For a body of arbitrary shape there is no closed-form analytical solution for  $\gamma_d(c)$ ; rather, the solution must be obtained numerically. Following the classical panel method approach, the discrete counterpart of (1.32) is obtained by approximating the curvilinear integral with a quadrature rule, thus dividing the profile into  $M_p$  panels with length  $\Delta c_n$ . The panels are spaced such that pivotal points on the upper and lower surface lie directly opposite to one another in pairs. Using the trapezium rule yields the following system of  $M_p \times M_p$  linear algebraic equations:

$$\left\{ \begin{array}{l} \sum_{n=1}^{M_p} K(c_1, c_n) \gamma_d(c_n) = -(U_\infty + u_{ad,1}) \cos \beta_1 - v_{ad,1} \sin \beta_1 \\ \sum_{n=1}^{M_p} K(c_2, c_n) \gamma_d(c_n) = -(U_\infty + u_{ad,2}) \cos \beta_2 - v_{ad,2} \sin \beta_2 \\ \vdots \\ \sum_{n=1}^{M_p} K(c_m, c_n) \gamma_d(c_n) = -(U_\infty + u_{ad,m}) \cos \beta_m - v_{ad,m} \sin \beta_m \\ \vdots \\ \sum_{n=1}^{M_p} K(c_{M_p}, c_n) \gamma_d(c_n) = -(U_\infty + u_{ad,M_p}) \cos \beta_{M_p} - v_{ad,M_p} \sin \beta_{M_p}. \end{array} \right. \quad (1.41)$$

In the above equations,  $u_{ad,m}$  and  $v_{ad,m}$  have to be evaluated through (1.39)-(1.40), while the entries of matrix  $K$  are equal to  $k(c_m, c_n) \Delta c_n$  when  $n \neq m$  and  $k(c_m, c_m) \Delta c_m - \frac{1}{2} \gamma_d(c_m)$  for  $n = m$ . Therefore, the coefficients  $K(c_m, c_n)$  may be interpreted as the tangent to the wall velocity induced at  $c_m$  by the ring vortex of unit strength located at  $c_n$ . Thus, denoting by  $u_{mn}$  and  $v_{mn}$  the axial and radial velocities due to the unit-strength ring vortex, the  $K(c_m, c_n)$  coefficients are (Gibson 1972)

$$K(c_m, c_n) = (u_{mn} \cos \beta_m + v_{mn} \sin \beta_m) \Delta c_n,$$

with

$$u_{mn} = -\frac{1}{2\pi\sigma_n\sqrt{\zeta^{*2} + (\sigma^* + 1)^2}} \left\{ K(k) - \left[ 1 + \frac{2(\sigma^* - 1)}{\zeta^{*2} + (\sigma^* - 1)^2} \right] E(k) \right\},$$

$$v_{mn} = \frac{\zeta^*/\sigma^*}{2\pi\sigma_n\sqrt{\zeta^{*2} + (\sigma^* + 1)^2}} \left\{ K(k) - \left[ 1 + \frac{2\sigma^*}{\zeta^{*2} + (\sigma^* - 1)^2} \right] E(k) \right\}.$$

In the above equations,  $K(k)$  and  $E(k)$  are complete elliptic integrals of the first and second kind,  $k = \sqrt{4\sigma^*/[\zeta^{*2} + (\sigma^* + 1)^2]}$ ,  $\sigma^* = \sigma_m/\sigma_n$  and  $\zeta^* = (\zeta_m - \zeta_n)/\sigma_n$ .

As proven in Martensen (1959) the matrix  $K$  is nearly singular. Moreover, the trapezoidal integration in the  $m$ th equation is reasonably accurate except for those element pairs formed with the subset of points lying on the opposite surface in closest proximity to point  $m$  (see Wilkinson (1967a) for details). There the integrand has a high and narrow peak, the area of which is typically overestimated by the trapezium rule method. To overcome this problem, the so-called back-diagonal correction, first proposed by Jacob and Riegels (1963), is used (see also Wilkinson (1967a) and Lewis (1991)). The technique operates on the back-diagonal of the matrix  $K$ , i.e. on the coefficients  $K(c_i, c_{M_p+1-i})$  with  $i = 1, \dots, M_p$ , to account for the quadrature errors. Specifically, it requires that the coupling coefficients opposite to point  $c_m$  with  $m = 1, \dots, M_p$ , i.e.  $K(c_{M_p+1-m}, c_m)$ , are replaced by a mean value derived by the condition of irrotationality in the inner of the profile:

$$\sum_{n=1}^{M_p} K(c_n, c_m) \Delta c_n = 0 \quad m = 1, \dots, M_p. \quad (1.42)$$

A detailed proof of equation (1.42) can be found in Lewis (1991). Using (1.42) the opposite coupling coefficients, which lie on the back diagonal of the matrix  $K$ , have to be replaced with

$$K(c_{M_p+1-m}, c_m) = -\frac{1}{\Delta c_{M_p+1-m}} \sum_{\substack{n=1 \\ n \neq M_p+1-m}}^{M_p} K(c_n, c_m) \Delta c_n \quad m = 1, \dots, M_p, \quad (1.43)$$

ensuring that the net circulation around the profile interior, implied by the numerical model, is made to be zero. The outcome of this procedure is a singular matrix because, from equation (1.43), it can be inferred that the





The integration of (1.38)-(1.40) still requires knowledge of  $\sigma_s(\zeta)$ . Since, on the slipstream boundary, the Stokes stream function is constant and equal to  $\Psi(0, \sigma_{ad})$ , then equation (1.38) reduces there to the following nonlinear integral equation for  $\sigma_s(\zeta)$ :

$$\begin{aligned} \Psi(0, \sigma_{ad}) &= \frac{U_\infty \sigma_s^2(\zeta)}{2} + \Psi'_d(\zeta, \sigma_s(\zeta)) \\ &+ \sigma_s(\zeta) \int_0^\infty \sum_{n=0}^N A_n(z) 2^{n-1} n! \sigma_s^{2-n}(z) I_{(-n-1, n+2, 1)}(\sigma_s(z), \sigma_s(z), \zeta - z) dz \end{aligned} \quad (1.52)$$

with  $\Psi'_d = \Psi_d - \frac{1}{2} U_\infty \sigma^2$ , to be solved iteratively. The solution procedure begins by computing and storing in a pre-processing stage the LU decomposition of the coefficient matrix  $K$  that appears in (1.47)-(1.48), which merely depends upon the duct geometry. Subsequently, the  $\gamma_{d,2}(c_m)$  distribution is evaluated once by (1.48). Assume now that provisional values of  $\sigma_s(\zeta)$  and  $\{A_n\}_{n=0, N}$  are available within the wake, for instance from the previous iteration. Likewise, assume provisional values of  $\gamma_d(c_m)$  on the profile are available. Then the Stokes stream function in the wake can be evaluated through (1.38) by performing the integration in the axial direction numerically. Next, the tangential vorticity field can be computed with (1.35) and parametrized with (1.36) through a new set of  $\{A_n\}_{n=0, N}$ , selected with the help of a least-squares minimization procedure. Then from (1.39) and (1.40) the axial and radial velocities induced by the actuator disk on the profile are evaluated, and the rhs of (1.47) and consequently  $\gamma_{d,1}(c_m)$  are updated. After that, the Kutta condition is enforced through (1.50) and a new value of  $\gamma_d(c_m)$  results from (1.49). Finally, from (1.52), the new  $\sigma_s(\zeta)$  is

$$\sigma_s(\zeta) = \sqrt{\left( \frac{\Psi'_d(\zeta, \sigma_s(\zeta))}{\sigma_s(\zeta) U_\infty} + \frac{I(\zeta, \sigma_s(\zeta))}{U_\infty} \right)^2 + \frac{2\Psi(0, \sigma_{ad})}{U_\infty} - \frac{\Psi'_d(\zeta, \sigma_s(\zeta))}{\sigma_s(\zeta) U_\infty} - \frac{I(\zeta, \sigma_s(\zeta))}{U_\infty}},$$

where

$$I(\zeta, \sigma_s(\zeta)) = \int_0^\infty \sum_{n=0}^N A_n(z) 2^{n-1} n! \sigma_s^{2-n}(z) I_{(-n-1, n+2, 1)}(\sigma_s(z), \sigma_s(z), \zeta - z) dz.$$

At the first iteration  $\gamma_d(c_m)$ ,  $\sigma_s(\zeta)$  and  $\Psi$  are calculated ignoring the presence of the disk.

From an engineering point of view, it would definitely be preferable to specify the radial distribution of the disk load  $\mathcal{H}(\sigma)$ . However, on physical

grounds, the existence of a one-to-one correspondence between  $\mathcal{H}(\sigma)$  and  $\mathcal{H}(\Psi)$  is conjectured, and therefore it is always possible to prescribe  $\mathcal{H}(\sigma)$  and then to evaluate the associated  $\mathcal{H}(\Psi)$ ; for example, it is possible to prescribe  $\mathcal{H}(\sigma)$  at the disk and then to update the coefficient  $a_m$  in (1.34) to match  $\mathcal{H}(\sigma)$  at each iteration (Conway 1998).

## 1.6 Results and applications

The method described in the previous sections provides the values of all physical quantities needed to evaluate the performance parameters of the device, namely the thrust coefficient  $C_T$  and the power coefficient  $C_P$ . Moreover another very important performance coefficient, typically employed in the propeller field, is the propulsive efficiency  $\eta = C_T/C_P$ . In particular, integrating the static pressure jump  $\Delta p_{ad}(\sigma)$  across the actuator disk and the power over the rotor plane yields

$$C_{T,rot} = \frac{T_{rot}}{\frac{1}{2}\pi\rho U_\infty^2 \sigma_{ad}^2} = \frac{1}{\frac{1}{2}\pi\rho U_\infty^2 \sigma_{ad}^2} \int_0^{\sigma_{ad}} \Delta p_{ad}(\sigma) 2\pi\sigma \, d\sigma, \quad (1.53)$$

$$C_P = \frac{P}{\frac{1}{2}\pi\rho U_\infty^3 \sigma_{ad}^2} = \frac{1}{\frac{1}{2}\pi\rho U_\infty^3 \sigma_{ad}^2} \int_0^{\sigma_{ad}} \mathcal{H}(\sigma)\rho u(0, \sigma) 2\pi\sigma \, d\sigma, \quad (1.54)$$

where  $T_{rot}$  and  $P$  are the axial force and the power experienced by the rotor. In the following, quantities denoted with a hat ( $\hat{\cdot}$ ) are made dimensionless using the reference length  $\sigma_{ad}$  and reference velocity  $U_\infty$ . Therefore, (1.53) and (1.54) can be expressed in terms of dimensionless variables, leading to

$$C_{T,rot} = 2 \int_0^1 \Delta \hat{p}_{ad}(\hat{\sigma}) \hat{\sigma} \, d\hat{\sigma}, \quad (1.55)$$

$$C_P = 2 \int_0^1 \hat{u}(0, \hat{\sigma}) \hat{\mathcal{H}}(0, \hat{\sigma}) \hat{\sigma} \, d\hat{\sigma}, \quad (1.56)$$

where  $\Delta \hat{p}_{ad} = 2\Delta p_{ad}/\rho U_\infty^2$  and  $\hat{\mathcal{H}} = 2\mathcal{H}/U_\infty^2$ . The thrust coefficient of the duct, computed by integrating over its surface the axial force due to the pressure, reads

$$C_{T,duct} = \frac{1}{\frac{1}{2}\pi\rho U_\infty^2 \sigma_{ad}^2} \oint_C p(c) \mathbf{n} 2\pi\sigma(c) \, dc \cdot \mathbf{i}_\zeta = -2 \oint_C \hat{\sigma}(\hat{c}) C_{p,w}(\hat{c}) \sin \beta(\hat{c}) \, d\hat{c}, \quad (1.57)$$

where  $C_{p,w} = 2(p-p_\infty)/\rho U_\infty^2$  is the wall pressure coefficient and  $\hat{c} = c/\sigma_{ad}$  is the dimensionless curvilinear abscissa. Finally, the overall thrust coefficient

reads

$$C_T = C_{T,rot} + C_{T,duct}. \quad (1.58)$$

In the following subsections a few relevant applications of the present method are described. More precisely, the global and local flow characteristics are detailed both for a ducted propeller and a ducted turbine. While the results of the former configuration are presented with and without slipstream rotation, those pertaining to the turbine are only given in the general case of wake rotation, for the sake of brevity. Moreover, a validation procedure of the method is carried out with the help of asymptotic solutions. A few convergence and stability results are also provided.

### 1.6.1 Ducted rotor without slipstream rotation

In the special case of a contra-rotating rotor pair or of a turbomachinery stage both with  $w(\zeta, \sigma) = 0$  in the wake, (1.35) returns

$$\frac{\omega_\theta(\zeta, \sigma)}{\sigma} = - \sum_{m=1}^M \frac{ma_m}{\Psi_{\sigma_{ad}}} \left( \frac{\Psi}{\Psi_{\sigma_{ad}}} \right)^{m-1}, \quad (1.59)$$

to be used in the iterative procedure instead of (1.35). In the downstream limit

$$\omega_\theta(\zeta \rightarrow +\infty, \sigma) = - \frac{d u}{d \sigma} \Big|_{(\zeta \rightarrow +\infty, \sigma)}. \quad (1.60)$$

Therefore, from equation (1.59) and from the definition of the Stokes stream function, the following second order variable coefficients ordinary differential equation can be obtained (Conway 1998):

$$\frac{1}{\sigma} \frac{d}{d\sigma} \left( \frac{1}{\sigma} \frac{d\Psi}{d\sigma} \right) = \sum_{m=1}^M \frac{ma_m}{\Psi_{\sigma_{ad}}} \left( \frac{\Psi}{\Psi_{\sigma_{ad}}} \right)^{m-1}, \quad (1.61)$$

with the associated boundary conditions

$$\begin{aligned} \Psi(\zeta \rightarrow +\infty, \sigma=0) &= 0 \\ \Psi(\zeta \rightarrow +\infty, \sigma=\sigma_s(\zeta \rightarrow +\infty)) &= \Psi_{\sigma_{ad}} \end{aligned} \quad (1.62)$$

To validate the method described in §1.5, equation (1.61) can be integrated, numerically or in some special cases analytically, obtaining accurate values of  $\Psi$  and  $u$  at infinity. Furthermore, a different formulation of the performance coefficients of the device can be obtained through the distribution of axial

velocity at infinity. In fact, as a classical result of actuator disk theory, these coefficients can be related to the axial velocity at infinity. In particular, from the axial momentum and energy equations  $C_T$  and  $C_P$  can be expressed as

$$\begin{aligned} C_T &= \frac{T}{\frac{1}{2}\pi\rho U_\infty^2 \sigma_{ad}^2} \\ &= \frac{1}{\frac{1}{2}\pi\rho U_\infty^2 \sigma_{ad}^2} \int_0^{\sigma_s(+\infty)} (u(+\infty, \sigma) - U_\infty) \rho u(+\infty, \sigma) 2\pi\sigma \, d\sigma \quad (1.63) \\ &= 4 \int_0^{\hat{\sigma}_s(+\infty)} \hat{u}(+\infty, \hat{\sigma}) (\hat{u}(+\infty, \hat{\sigma}) - 1) \hat{\sigma} \, d\hat{\sigma}, \end{aligned}$$

$$\begin{aligned} C_P &= \frac{P}{\frac{1}{2}\pi\rho U_\infty^3 \sigma_{ad}^2} \\ &= \frac{1}{\frac{1}{2}\pi\rho U_\infty^3 \sigma_{ad}^2} \int_0^{\sigma_s(+\infty)} (H(+\infty, \sigma) - H_\infty) \rho u(+\infty, \sigma) 2\pi\sigma \, d\sigma \quad (1.64) \\ &= 2 \int_0^{\hat{\sigma}_s(+\infty)} \hat{u}(+\infty, \hat{\sigma}) (\hat{H}(+\infty, \hat{\sigma}) - \hat{H}_\infty) \hat{\sigma} \, d\hat{\sigma}. \end{aligned}$$

With the help of (1.34), equation (1.64) can be integrated analytically to give

$$C_P = \frac{4\Psi_{\sigma_{ad}}}{U_\infty^3 \sigma_{ad}^2} \sum_{m=0}^M \frac{a_m}{m+1}. \quad (1.65)$$

In the special case of a wake without swirl, the pressure jump across the disk is directly related to the load through

$$\mathcal{H} = \frac{\Delta p_{ad}(\sigma)}{\rho} \quad (1.66)$$

thus obtaining

$$\Delta \hat{p}_{ad}(\sigma) = \hat{\mathcal{H}}(\Psi) = \frac{2}{U_\infty^2} \sum_{m=0}^M a_m \left( \frac{\Psi}{\Psi_{\sigma_{ad}}} \right)^m, \quad (1.67)$$

to be used in (1.55) in order to calculate the rotor thrust coefficient  $C_{T,rot}$ .

For the simple case of a load distribution of the type

$$\mathcal{H}(\Psi) = a_1 \left[ \frac{\Psi}{\Psi_{\sigma_{ad}}} - \left( \frac{\Psi}{\Psi_{\sigma_{ad}}} \right)^2 \right], \quad (1.68)$$

Chord/rotor diameter	$chord/D$	1/2.76
Angle between the profile chord and the $\zeta$ axis	$\alpha$	12.7°
Tip gap/rotor diameter	$\epsilon/D$	1.244%
Leading edge radial position/rotor diameter	$\sigma_{LE}/D$	0.580
Leading edge axial position/rotor diameter	$\zeta_{LE}/D$	-0.111
Load magnitude parameter	$\hat{b} = \frac{\sigma_{ad}^2 a_1}{U_\infty \Psi \sigma_{ad}}$	15
Advance coefficient (only with wake rotation)	$J$	0.5

Table 1.1: Propeller ducted with a NACA 4415 profile: geometry and operating conditions.

the solution procedure applied to a rotor ducted with a NACA 4415 (see Table 1.1 for details) returns the wall pressure coefficient and the dimensionless load radial distribution reported in Figure 1.4. While the shape of the computed dimensionless load radial distribution obtained with the simple equation (1.68), bears a good physical resemblance to that for a typical propeller, its magnitude (i.e. the particular value of  $\hat{b}$ ) has been selected in order to enhance the performance of the duct. In more detail, the value of  $\hat{b} = 15$  leads to a position of the front stagnation point in the leading edge area, so that undesired suction or pressure side velocity peaks are avoided. This is clearly visible from the duct wall pressure coefficient of Figure 1.4a.

Figure 1.5 shows the streamlines over the ducted actuator disk, denoted by the thick solid line. The dot-dashed line defines the slipstream edge  $\sigma_s(\zeta)$ . The no-penetration condition over the duct, enforced in the iterative process through equations (1.47)-(1.48), is clearly satisfied by the solution, as evident by the two streamlines flowing just above and below the profile. Moreover, the position of the front stagnation point is readily localized by the dividing streamline. Finally, the flow leaves the profile smoothly at the trailing edge according to the Kutta condition requirement.

Figure 1.6 shows the radial distributions of axial and radial dimensionless velocity at different axial stations (see also Figure 1.5 as a graphical aid to locate them). As a first remark, both distributions highlight the typical propeller slipstream contraction whose magnitude is largely dictated by the disk load. In fact the radial velocity is essentially negative in the outer part of the slipstream. Moreover, the axial velocity excess increases in the streamwise direction, while the radial velocity simultaneously approaches zero. The above features further prove the contraction of the slipstream

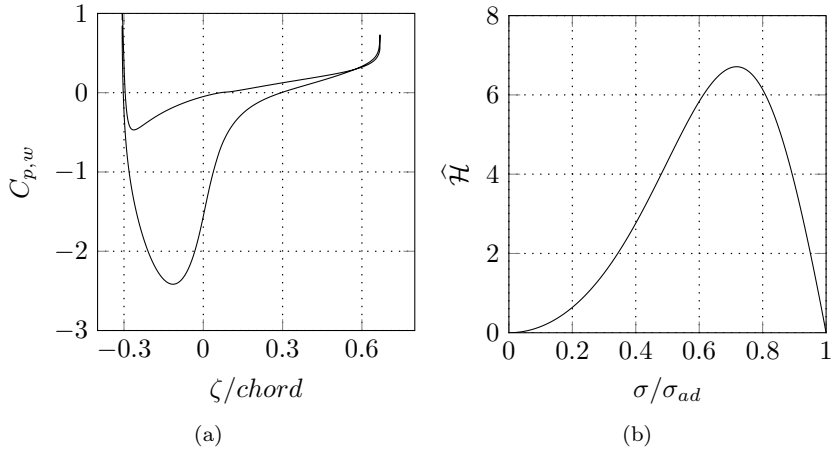


Figure 1.4: Propeller ducted with a NACA 4415 profile with  $\hat{b} = 15$ : (a) duct wall pressure coefficient; (b) radial distribution of the load.

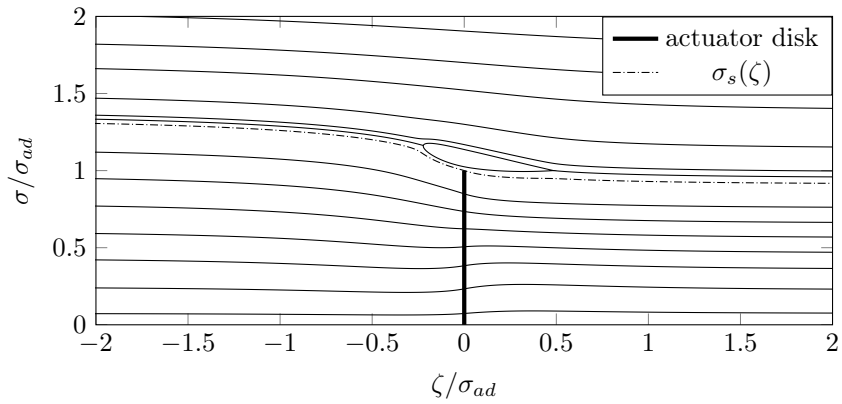


Figure 1.5: Propeller ducted with a NACA 4415 profile with  $\hat{b} = 15$ : streamlines.

$\widehat{b}$	$\omega_{rf} = 1$	$\omega_{rf} = 1/3$	$\omega_{rf} = 1/6$
5	12	27	47
10	32	32	64
15	178	39	73
20	not converged	39	78

Table 1.2: Propeller ducted with a NACA 4415 profile with  $\widehat{b} = 15$ : Number of iterations needed to reach convergence with different loads and relaxation factors  $\omega_{rf}$ .

and the establishment of the wake contraction in the downstream limit, respectively. Finally, the total, axial and radial velocity contours are shown in Figure 1.7.

The slipstream  $\sigma_s(\zeta)$  at different iterations and the convergence history are given in Figure 1.8. In the latter, the residue is defined as the absolute value of the difference between two successive slipstream radii evaluated at  $\zeta = 5\sigma_{ad}$ , normalized with  $\sigma_{ad}$ . The number of iterations needed to reach convergence with different values of  $\widehat{b}$  is detailed in Table 1.2. The convergence of the iterative process is very rapid for moderate loads and worsens for higher loads, so that under-relaxation is typically needed in order to preserve stability. In particular, the value of the slipstream radius at each iteration is updated through the relation:

$$\sigma_s(\zeta) = \sigma_s(\zeta)|_{old} + [\sigma_s(\zeta)|_{new} - \sigma_s(\zeta)|_{old}] \omega_{rf} \quad (1.69)$$

where  $\omega_{rf}$  is the relaxation factor. The latter should be fixed minimizing the number of iterations needed to reach convergence; Table 1.2 shows typical values.

In the special case of a parabolic load distribution, like the one in (1.68), equation (1.61) reduces to

$$\frac{1}{\sigma} \frac{d}{d\sigma} \left( \frac{1}{\sigma} \frac{d\Psi}{d\sigma} \right) = \frac{U_\infty \widehat{b}}{\sigma_{ad}^2} \left[ 1 - 2 \left( \frac{\Psi}{\Psi_{\sigma_{ad}}} \right) \right]. \quad (1.70)$$

The analytical solution of the above equation, with the associated boundary conditions (1.62), is detailed in Conway (1998). Figure 1.9 compares the dimensionless axial velocity distribution computed by the iterative scheme described in §1.5 with the analytical one obtained solving (1.70). It is worth noting that at four propeller radii downstream of the disk the axial velocity

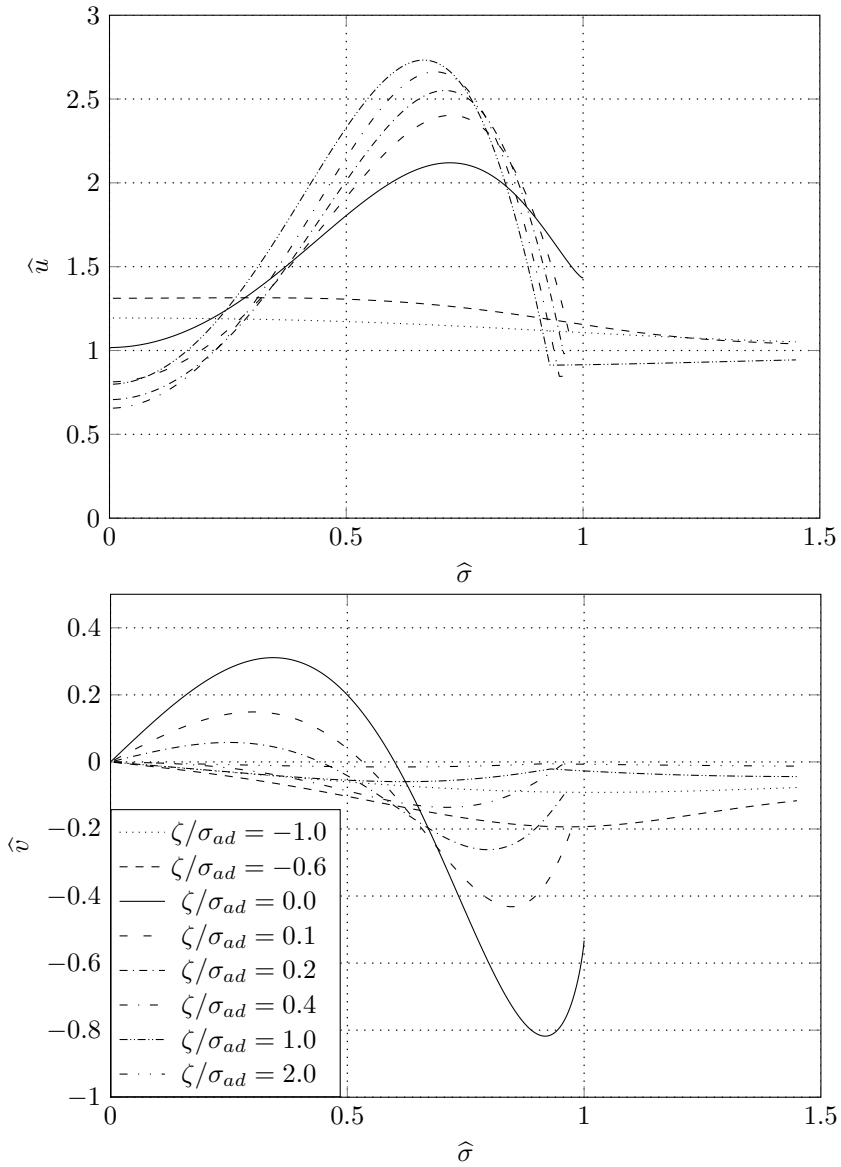


Figure 1.6: Propeller ducted with a NACA 4415 profile with  $\hat{b} = 15$ :  $\hat{u}$  (top) and  $\hat{v}$  (bottom) radial distributions at different axial stations.

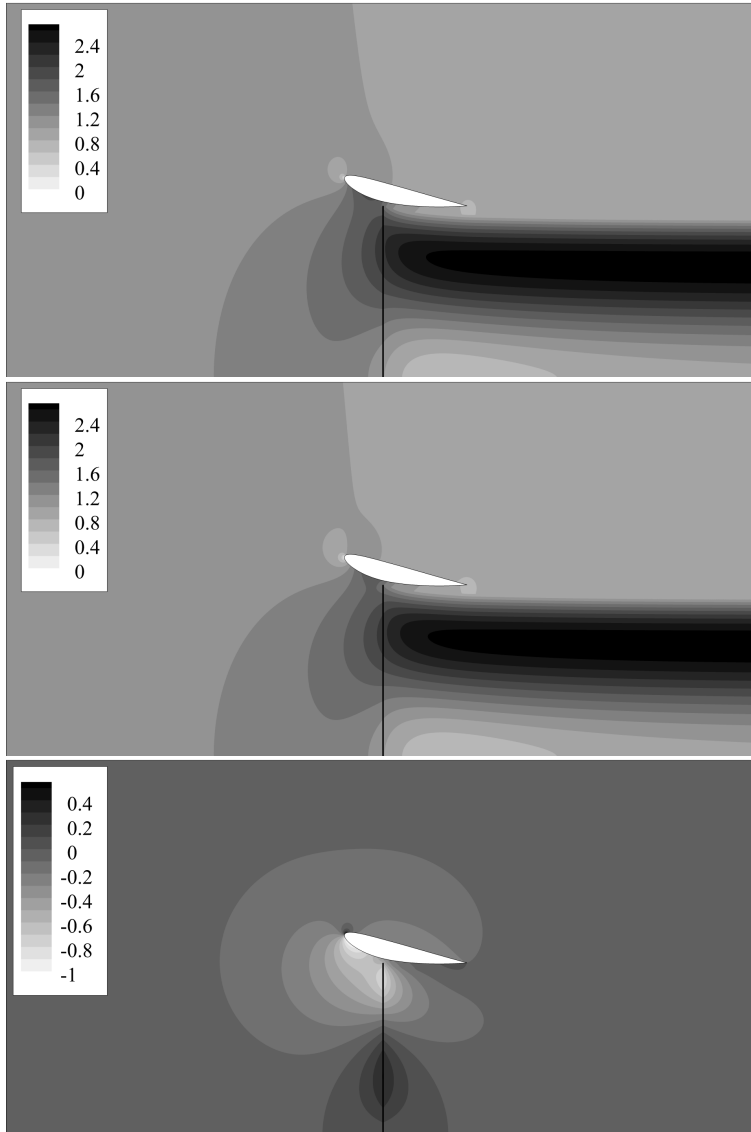


Figure 1.7: Propeller ducted with a NACA 4415 profile with  $\hat{b} = 15$ : contours of total (top), axial (middle) and radial (bottom) velocity.

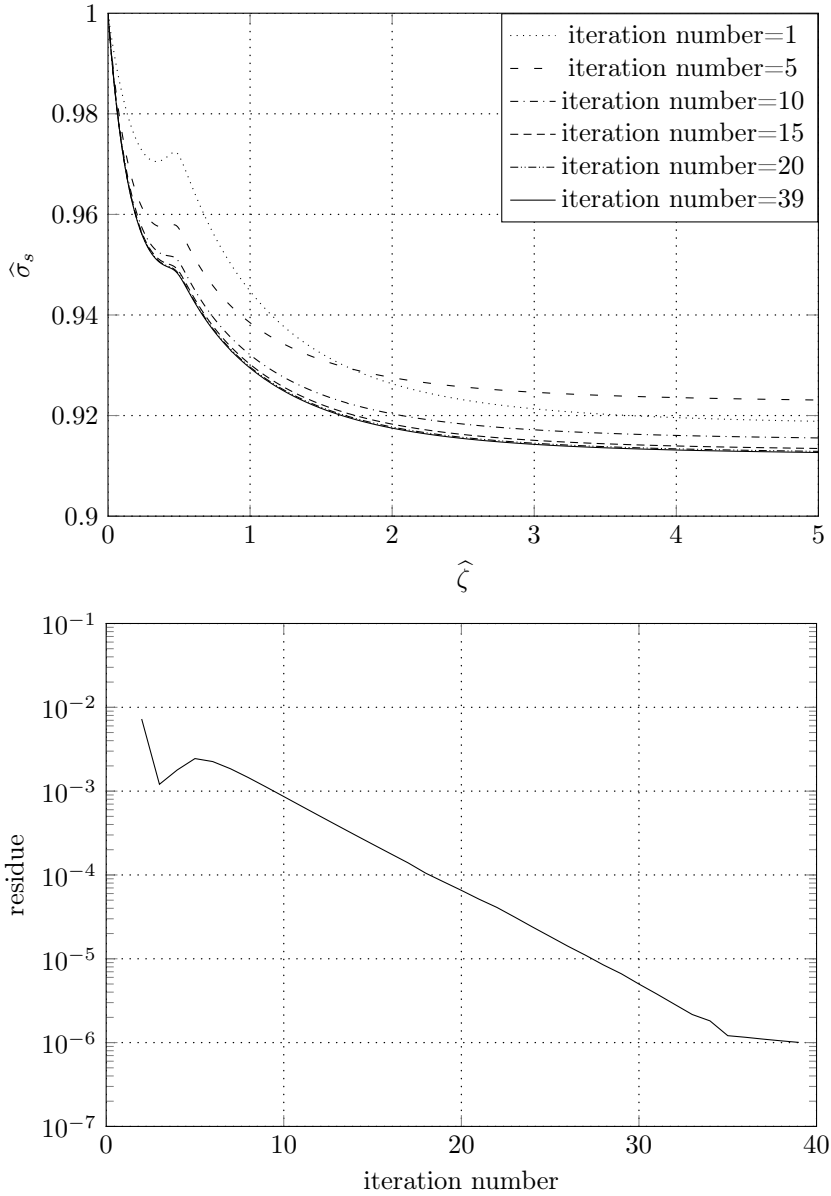


Figure 1.8: Propeller ducted with a NACA 4415 profile with  $\hat{b} = 15$ : convergence analysis.

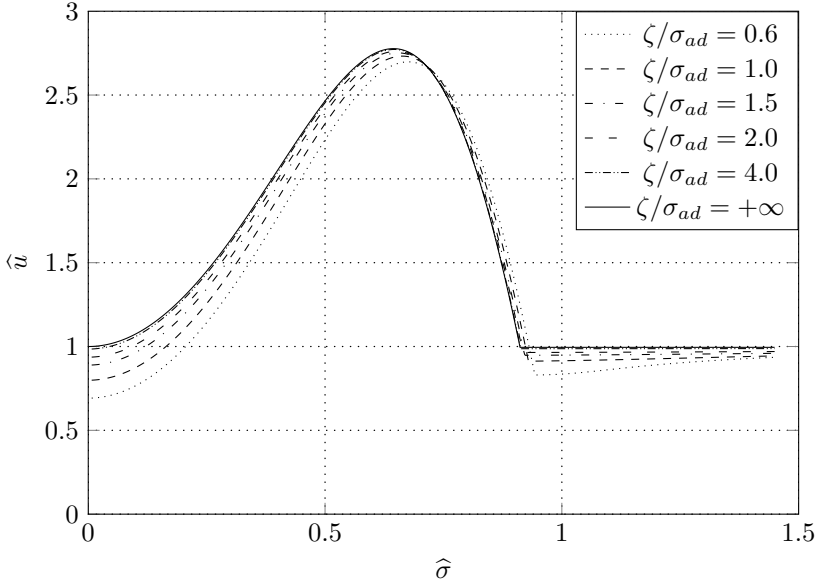


Figure 1.9: Propeller ducted with a NACA 4415 profile with  $\hat{b} = 15$ : approach of the  $\hat{u}$  radial distribution to the asymptotic one.

field has almost reached the theoretical profile at infinity. The above result provides a validation of the method and gives evidence of an appropriate control of the related numerical issues.

Finally, the global performance coefficients for the NACA 4415 case are listed in Table 1.3.

$C_T$	$C_{T,rot}$	$C_{T,duct}$	$C_P$	$\eta$
4.62	4.14	0.48	8.01	0.58

Table 1.3: Propeller ducted with a NACA 4415 profile with  $\hat{b} = 15$ : performance coefficients.

## 1.6.2 Ducted rotor with slipstream rotation

In the case with swirl, the tangential velocity  $w(\zeta, \sigma)$  is computed through the angular momentum equation (1.9), which, using (1.34), yields

$$\widehat{w}(\zeta, \sigma) = \frac{w(\zeta, \sigma)}{U_\infty} = \frac{J \sigma_{ad}}{\pi \sigma} \frac{1}{U_\infty^2} \sum_{m=0}^M a_m \left( \frac{\Psi}{\Psi_{ad}} \right)^m. \quad (1.71)$$

Recalling the expression for the  $\theta$  component of vorticity (1.35) and replacing in (1.35) its asymptotic value  $\omega_\theta(\zeta \rightarrow +\infty, \sigma)$  given by (1.60), the following second order variable coefficients ordinary differential equation is obtained:

$$\frac{1}{\sigma} \frac{d}{d\sigma} \left( \frac{1}{\sigma} \frac{d\Psi}{d\sigma} \right) = \left[ \frac{J^2}{\pi^2} \left( \frac{\sigma_{ad}}{\sigma} \right)^2 \frac{1}{U_\infty^2} \sum_{m=0}^M a_m \left( \frac{\Psi}{\Psi_{\sigma_{ad}}} \right)^m - 1 \right] \sum_{m=1}^M \frac{m a_m}{\Psi_{\sigma_{ad}}} \left( \frac{\Psi}{\Psi_{\sigma_{ad}}} \right)^{m-1} \quad (1.72)$$

with the associated boundary conditions (1.62). Like in the case without slipstream rotation, the above equation can be integrated to give an accurate solution for  $\Psi$  at downstream infinity and furthermore this result can be used to compute the performance coefficients of the device. In particular, the equivalent formula to (1.63) is

$$C_T = 2 \int_0^{\widehat{\sigma}_s(+\infty)} \left[ \frac{2\pi}{J} \widehat{\sigma} \widehat{w}(+\infty, \widehat{\sigma}) + (\widehat{u}(+\infty, \widehat{\sigma}) - 1)^2 - \widehat{w}^2(+\infty, \widehat{\sigma}) \right] \widehat{\sigma} d\widehat{\sigma}, \quad (1.73)$$

while equations (1.64)-(1.65) are still valid.

The pressure jump across the disk is related to the load radial distribution through  $\mathcal{H} = \Delta p_{ad}(\sigma) / \rho + w^2(0^+, \sigma) / 2$ . The latter equation, elaborated with the help of (1.34) and (1.9), yields

$$\Delta \widehat{p}_{ad}(\sigma) = \frac{1}{U_\infty^2} \sum_{m=0}^M a_m \left( \frac{\Psi}{\Psi_{\sigma_{ad}}} \right)^m \left[ 2 - \frac{J^2}{\pi^2} \frac{\sigma_{ad}^2}{\sigma^2} \frac{1}{U_\infty^2} \sum_{m=0}^M a_m \left( \frac{\Psi}{\Psi_{\sigma_{ad}}} \right)^m \right], \quad (1.74)$$

to be used in (1.55) in order to calculate the rotor thrust coefficient  $C_{T,rot}$ .

With reference to the geometry and operating conditions detailed in Tables 1.1 and 1.4, Figures 1.10 and 1.11 show the wall pressure coefficient and the dimensionless load radial distribution for a propeller ducted with a NACA 4415 and a turbine ducted with a NACA 5415, respectively.

The particular value of  $\widehat{b} = 15$  ( $\widehat{b} = -2$  in the turbine case) leads again to a position of the front stagnation point lying in the leading edge area (see Figures 1.10a and 1.11a).

Chord/rotor diameter	$chord/D$	0.513
Angle between the profile chord and the $\zeta$ axis	$\alpha$	$-5.0^\circ$
Tip gap/rotor diameter	$\epsilon/D$	1.039%
Leading edge radial position/rotor diameter	$\sigma_{LE}/D$	0.559
Leading edge axial position/rotor diameter	$\zeta_{LE}/D$	-0.15
Load magnitude parameter	$\hat{b} = \frac{\sigma_{ad}^2 a_1}{U_\infty \Psi \sigma_{ad}}$	-2
Tip speed ratio	$\lambda$	$2\pi$

Table 1.4: Turbine ducted with a NACA 5415 profile: geometry and operating conditions.

This latter feature of the flow, the projection of the generatrices of the stream-tubes onto the meridian plane and the converging–diverging shape of the wake are shown in Figures 1.12 and 1.13. As for the case without swirl, the no-penetration and Kutta condition compliance can also be appreciated.

Figures 1.14-1.16 present the radial distributions of dimensionless axial, radial and tangential velocities at different axial stations. Concerning the through-flow velocity distributions, the same features as pointed out when discussing Figures 1.6 are also detectable in Figures 1.14 and 1.15. The tangential velocity falls to zero at the  $\zeta$  axis and at the slipstream edge, since the load is prescribed to vanish there. The dimensionless radii where  $w = 0$  in Figure 1.16 locate the slipstream edge contraction (divergence) moving downstream. Using the angular momentum conservation law (1.9), the variation of the  $\hat{w}$  profile as  $\zeta$  increases, can be easily explained. In fact, with reference to the propeller case, the tangential velocity along a streamline increases as  $\zeta$  increases, a consequence of the load  $\mathcal{H}$  invariance along the streamline while the latter is converging. Finally, the contours of total, axial and radial velocity are shown in Figures 1.17 and 1.18.

The slipstream  $\sigma_s(\zeta)$  at different iterations and the convergence history are given in Figure 1.19. There are no considerable effects of the slipstream rotation on the convergence and stability of the iterative process.

Equation (1.72) can be numerically integrated to obtain an accurate solution for  $\Psi$  at infinity; then  $\hat{u}(+\infty, \sigma)$  and  $\hat{w}(+\infty, \sigma)$  can be computed through the definition of the Stokes stream function and equation (1.71), respectively. To validate the slipstream rotation implementation, a sequence of  $\hat{u}$  and  $\hat{w}$  profiles, as  $\zeta$  increases, are shown together with the theoretical distribution at infinity in Figures 1.16 and 1.20. At four–six disk diameters downstream, the velocity distributions have nearly attained their cor-

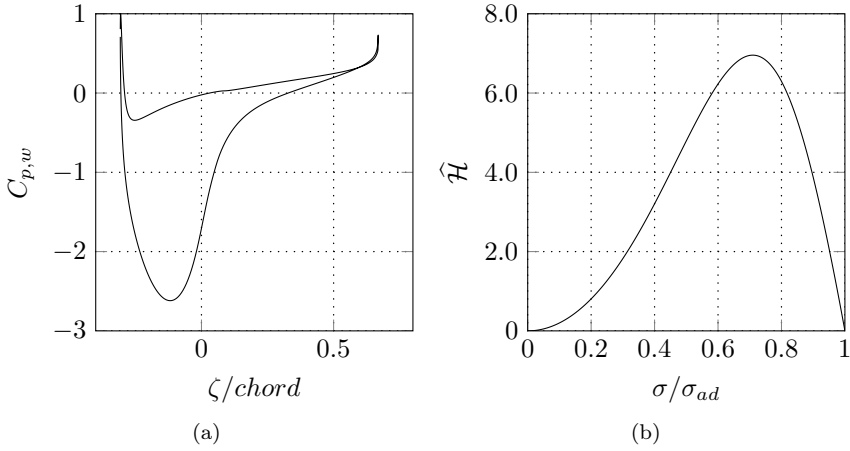


Figure 1.10: Propeller ducted with a NACA 4415 profile with  $\hat{b} = 15$  and  $J = 0.5$ : (a) duct wall pressure coefficient; (b) radial distribution of the load.

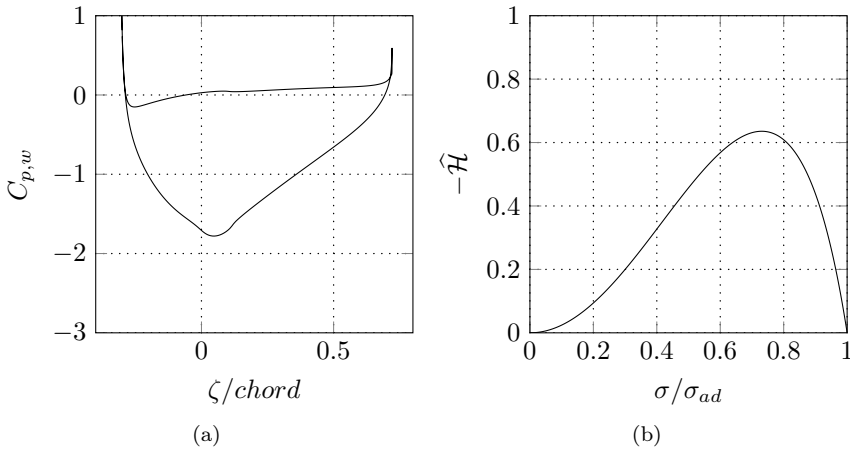


Figure 1.11: Turbine ducted with a NACA 5415 profile with  $\hat{b} = -2$  and  $\lambda = 2\pi$ : (a) duct wall pressure coefficient; (b) radial distribution of the load.

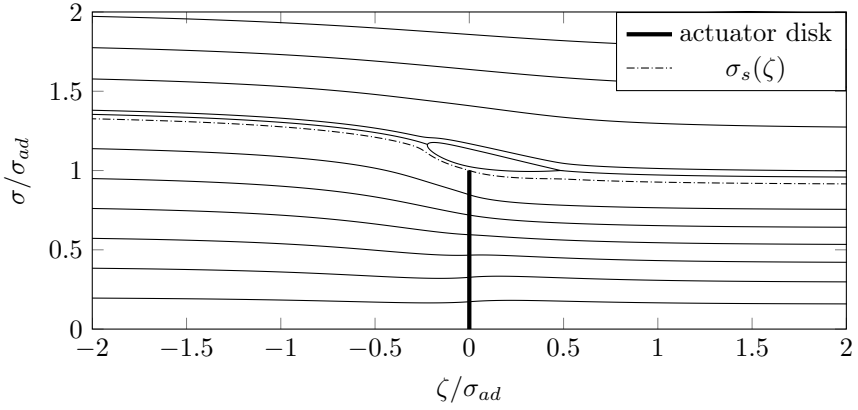


Figure 1.12: Propeller ducted with a NACA 4415 profile with  $\widehat{b} = 15$  and  $J = 0.5$ : projection of the generatrices of the stream-tubes onto the meridian plane.

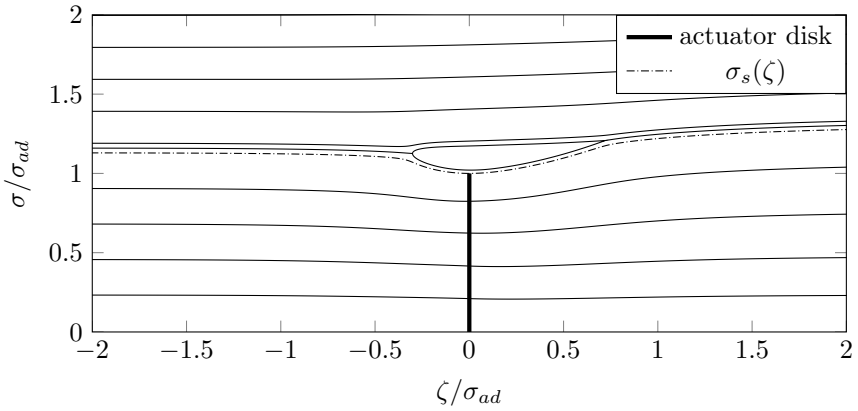


Figure 1.13: Turbine ducted with a NACA 5415 profile with  $\widehat{b} = 2$  and  $\lambda = 2\pi$ : projection of the generatrices of the stream-tubes onto the meridian plane.

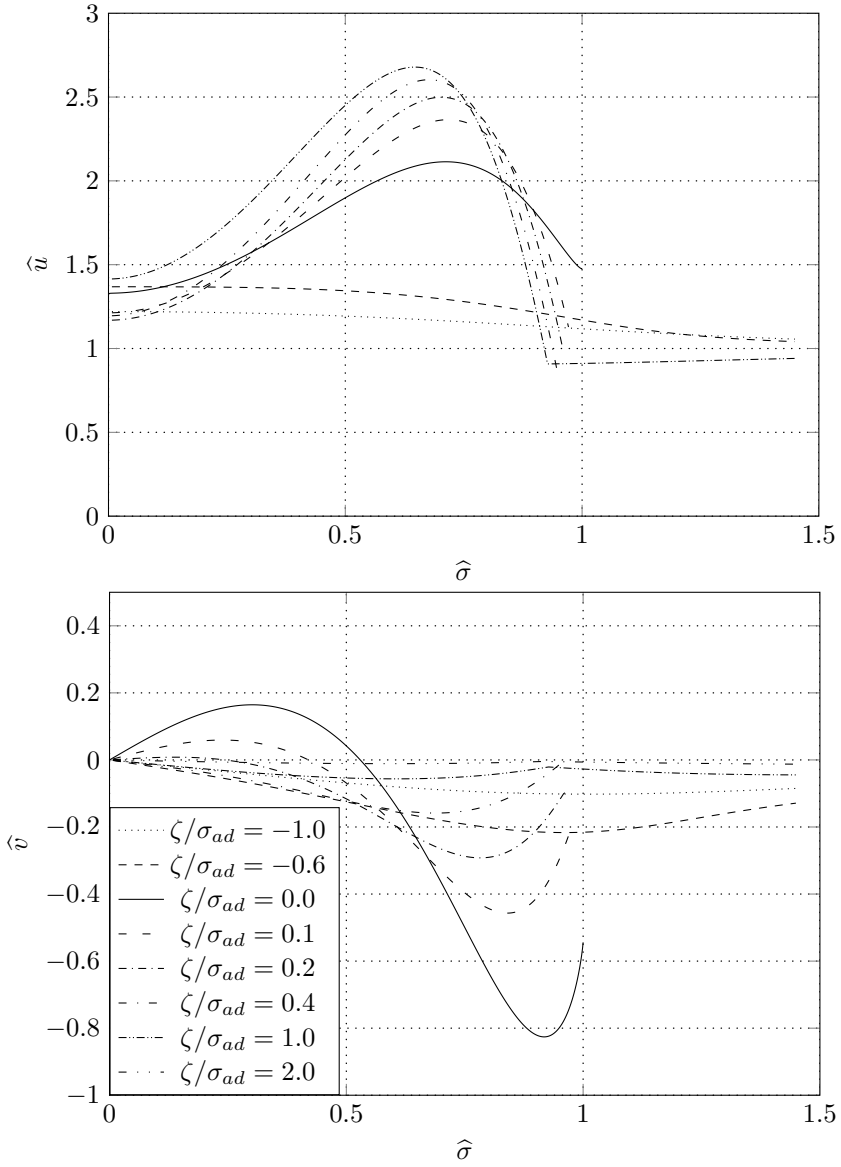


Figure 1.14: Propeller ducted with a NACA 4415 profile with  $\hat{b} = 15$  and  $J = 0.5$ :  $\hat{u}$  (top) and  $\hat{v}$  (bottom) radial distributions at different axial stations.

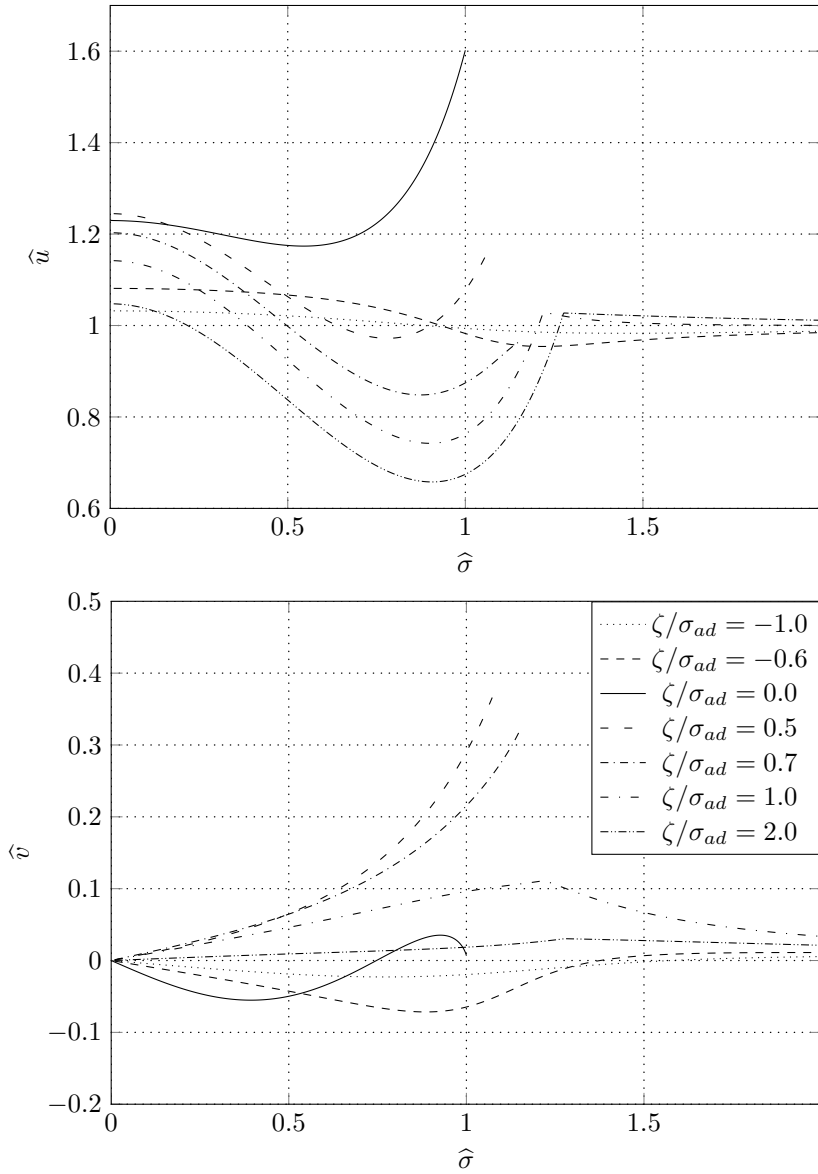


Figure 1.15: Turbine ducted with a NACA 5415 profile with  $\hat{b} = -2$  and  $\lambda = 2\pi$ :  $\hat{u}$  (top) and  $\hat{v}$  (bottom) radial distributions at different axial stations.

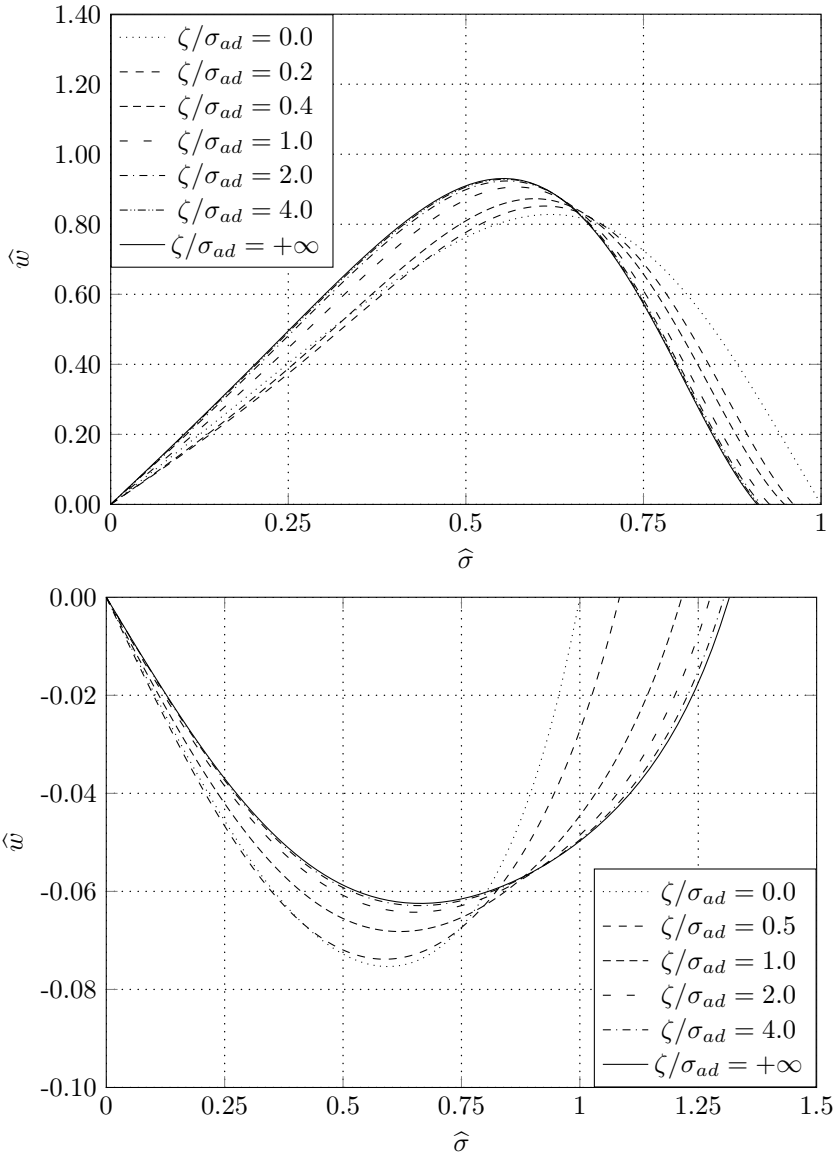


Figure 1.16:  $\hat{w}$  radial distribution at different axial stations. Top: propeller ( $\hat{b} = 15$  and  $J = 0.5$ ) ducted with a NACA 4415 profile. Bottom: turbine ( $\hat{b} = -2$  and  $\lambda = 2\pi$ ) ducted with a NACA 5415 profile.

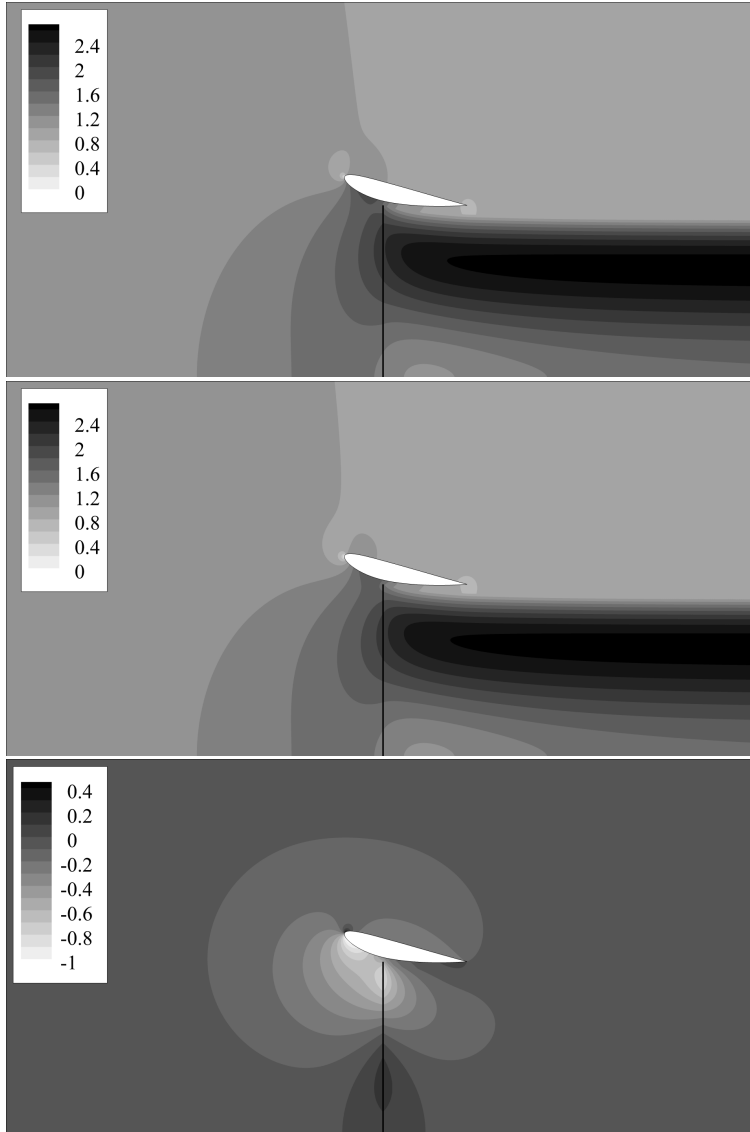


Figure 1.17: Propeller ducted with a NACA 4415 profile with  $\hat{b} = 15$  and  $J = 0.5$ : contours of total (top), axial (middle) and radial (bottom) velocity.

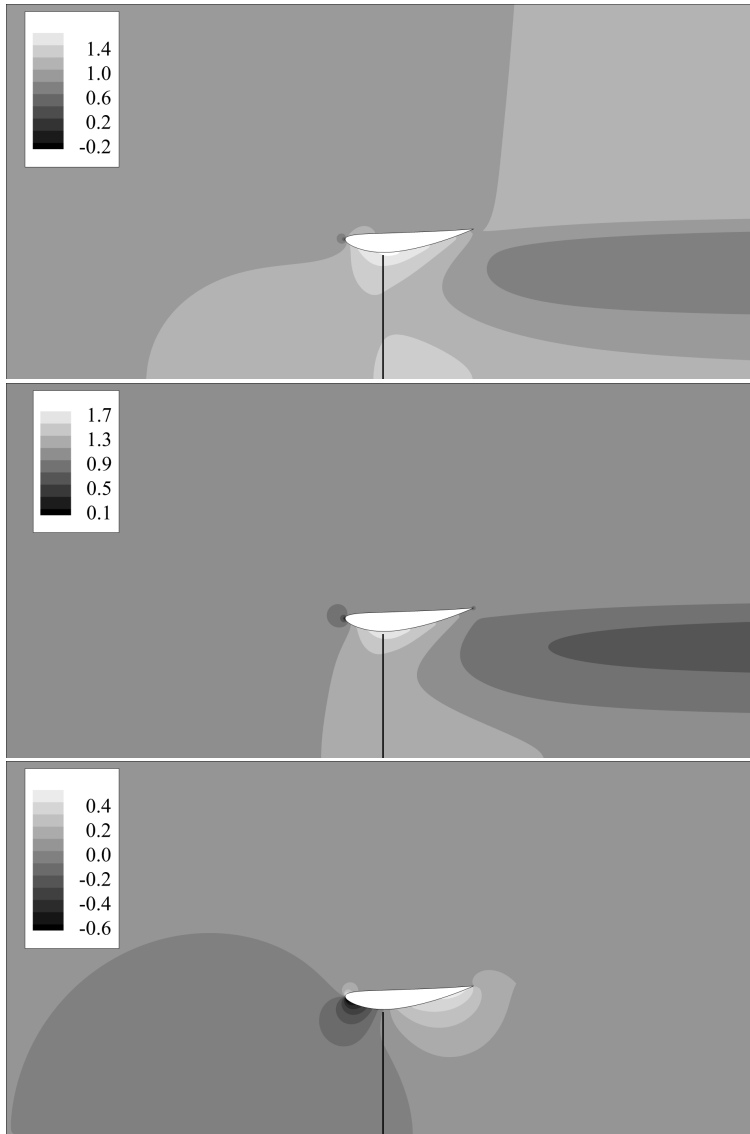


Figure 1.18: Turbine ducted with a NACA 5415 profile with  $\hat{b} = -2$  and  $\lambda = 2\pi$ : contours of total (top), axial (middle) and radial (bottom) velocity.

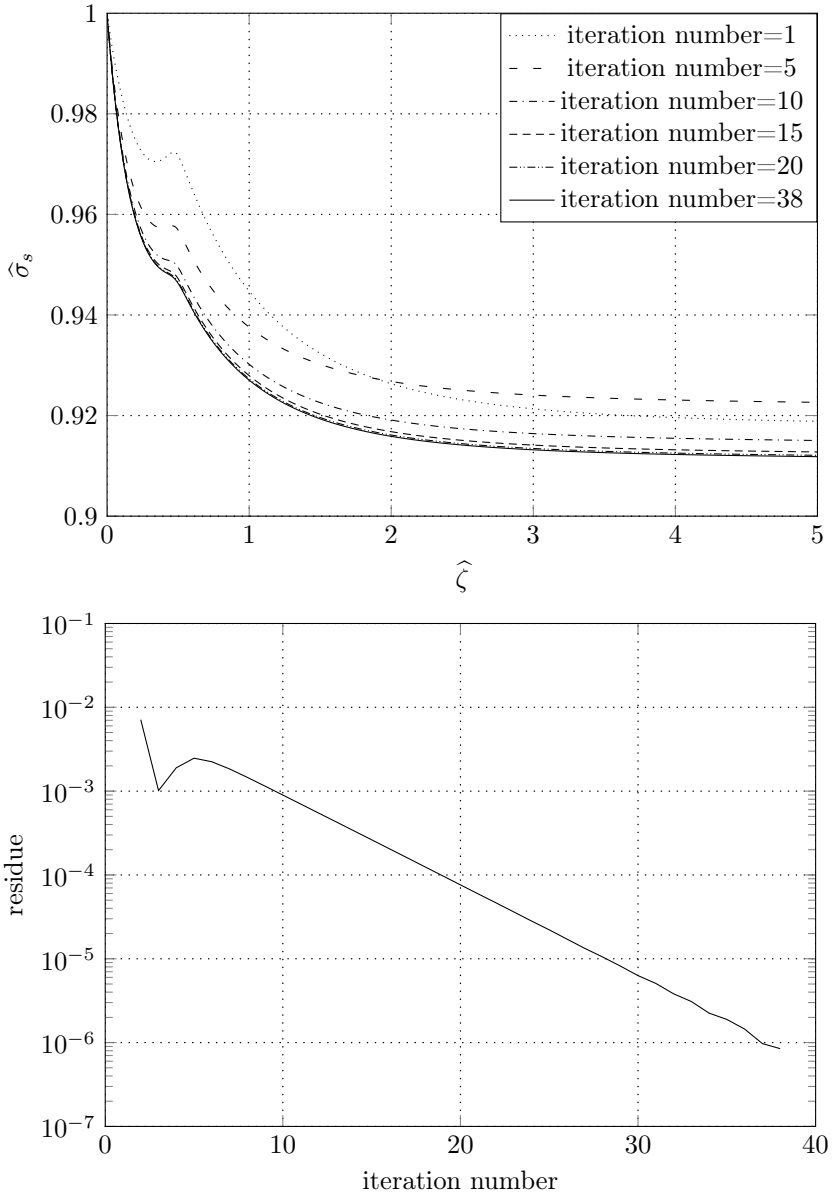


Figure 1.19: Propeller ducted with a NACA 4415 profile with  $\hat{b} = 15$  and  $J = 0.5$ : convergence analysis.

responding asymptotic values. Finally, the global performance coefficients are listed in Tables 1.6 and 1.5.

$C_T$	$C_{T,rot}$	$C_{T,duct}$	$C_P$
-0.64	-0.43	-0.21	-0.54

Table 1.5: Turbine ducted with a NACA 5415 profile with  $\hat{b} = -2$  and  $\lambda = 2\pi$ : performance coefficients.

$C_T$	$C_{T,rot}$	$C_{T,duct}$	$C_P$	$\eta$
4.57	4.02	0.55	8.60	0.53

Table 1.6: Propeller ducted with a NACA 4415 profile with  $\hat{b} = 15$  and  $J = 0.5$ : performance coefficients.

### 1.6.3 Comparison between open and ducted rotor

As mentioned in the introduction, the task of the duct is to improve the performance of the device. In particular, for a turbine with radius  $\sigma_{ad}$  and immersed in a uniform flow with free stream velocity  $U_\infty$ , the effect of the duct is to increase the power output or in dimensionless form the power coefficient  $C_P$ , that is, the ratio between the extracted and the available power. In more detail, for a turbine without slipstream rotation, the load at the disk can be expressed through equation (1.66). Consequently, the thrust and the power associated with the rotor infinitesimal surface element of area  $dA_{rot} = 2\pi\sigma d\sigma$  are  $dT_{rot} = \Delta p_{ad}(\sigma)dA_{rot} = \rho\mathcal{H}(\sigma)dA_{rot}$  and  $dP = \mathcal{H}(\sigma)d\dot{m} = (u(0, \sigma) + U_\infty)dT_{rot}$ , respectively. Finally, the local power coefficient is

$$dC_P = (\hat{u}(0, \hat{\sigma}) + 1)dC_{T,rot}. \quad (1.75)$$

The last equation shows that the power coefficient is the product of two terms related to the mass flow and the load, respectively. Hansen, Sorensen, and Flay (2000) and de Vries (1979) analysed the effects of placing a duct around a turbine without slipstream rotation through a 1D theoretical analysis and CFD results. In these works it is found that, for a ducted and open turbine with the same load, the presence of the duct can increase the mass flow passing through the disk, thus increasing the power coefficient (see equation (1.75)).

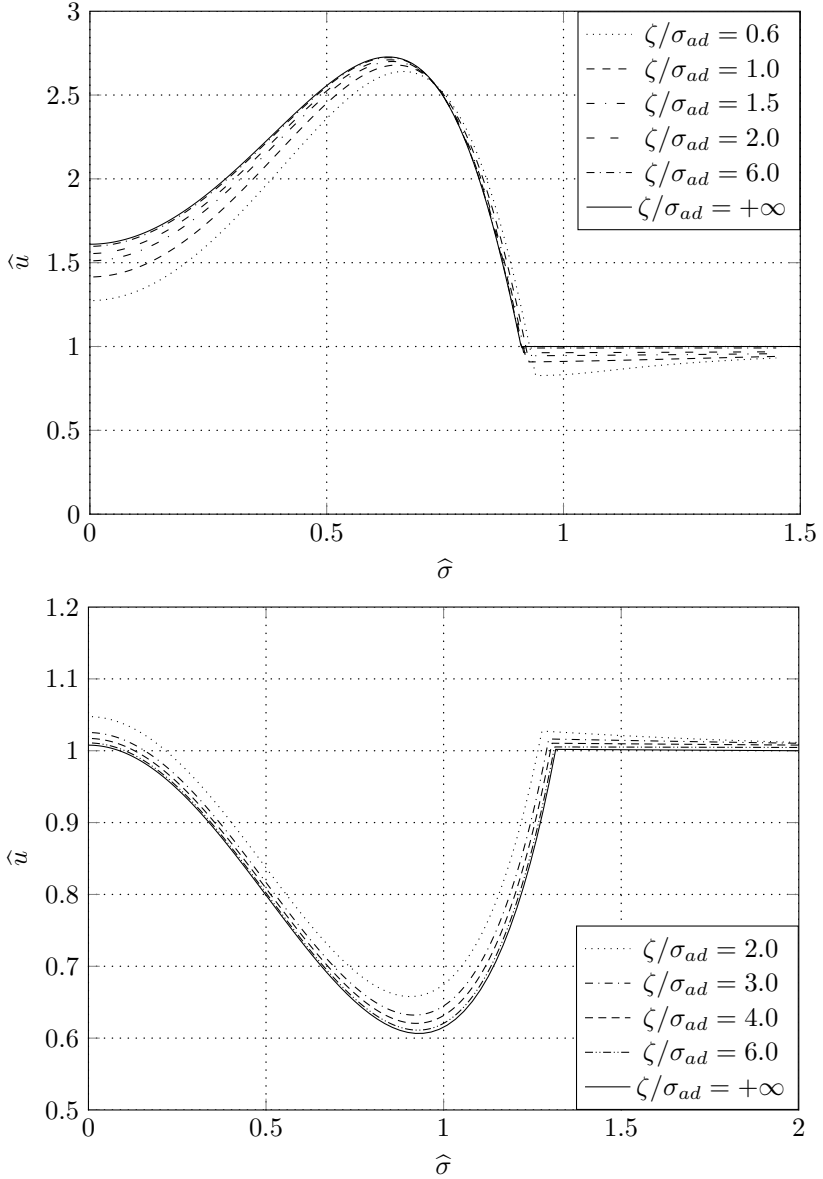


Figure 1.20:  $\hat{u}$  distribution at different axial stations for rotors with slipstream rotation. Top: propeller described in Table 1.1. Bottom: turbine described in Table 1.4.

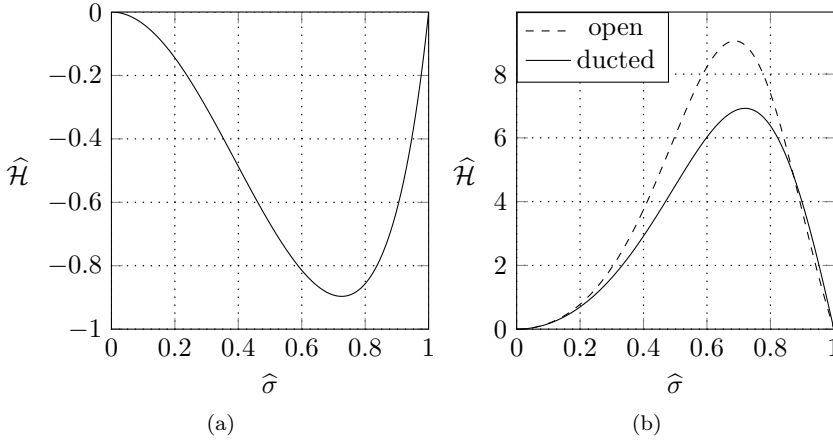


Figure 1.21: Load radial distribution for open and ducted rotors. Left: turbines. Right: propellers.

In the following, the previous issue is analysed through the method described in §1.4 and 1.5. Consider a turbine ducted with a NACA 5415 (see Table 1.4 for geometrical details) without swirl and an open turbine with the same load radial distribution (see Figure 1.21a). The results for this last configuration are obtained through the standard actuator disk method of Conway (1998). Because the radial loads  $\mathcal{H}(\sigma)$  of the two turbines are the same, they also have the same  $dC_{T,rot}$  and  $C_{T,rot}$ . However, since the presence of the duct increases the mass flow through the ducted rotor (see Figure 1.22), the power coefficient value of the ducted turbine is greater than that of the open turbine (see Table 1.7). Moreover, the  $C_P$  value of the ducted turbine is also greater than  $16/27 \simeq 0.593$ , which is the well-known maximum theoretical  $C_P$  value achievable by an open turbine (Betz limit).

Figure 1.22 also shows that, in order to obtain an increase of the mass flow, the duct slipstream  $\sigma_s(\zeta)$  has to be more divergent for  $\zeta > 0$  and more convergent for  $\zeta < 0$  in comparison with the open rotor configuration. So in the special case of a ducted turbine, the latter result points out the features of the method (which naturally takes into account the shape of the slipstream) in comparison with the 1D theory where the effects of the slipstream divergence is neglected.

For a propeller the main task of the duct is to increase the efficiency,

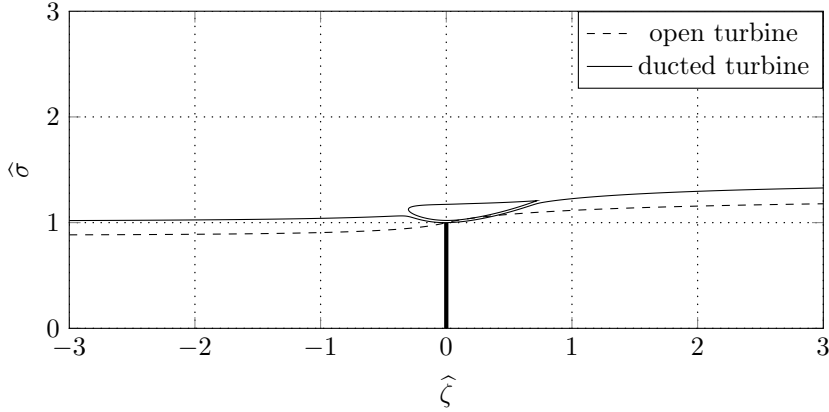


Figure 1.22: Comparison of the open and the ducted turbine slipstream edge.

notwithstanding the propulsive thrust required by the carrier. Hence, the efficiency being  $\eta = C_T/C_P$ , a well-designed duct enables the propeller to achieve a lower value of  $C_P$  without altering the total thrust coefficient  $C_T$ . Consider, then, an open propeller without slipstream rotation and with a parabolic load radial distribution. The performance coefficients obtained when setting  $\hat{b} = 22.025$  are detailed in Table 1.8. These results are obtained using the standard actuator disk method of Conway (1998). Consider now a propeller ducted with a NACA 5415 (see Table 1.9 for geometrical details) with the same radius  $\sigma_{ad}$  and radial load distribution ( $\hat{b} = 14.0$ ) as the open propeller. Such a propeller achieves the same  $C_T$  value as the open one (see Table 1.8), but now the thrust is split up between the duct and the rotor. In turn, the power coefficient  $C_P$  is lower than that of the open propeller alone and this results in a higher efficiency. Figures 1.23 and 1.21b show the slipstream edge and the load radial distribution for the open and the ducted propeller. From Figure 1.23, it is easily inferred that the ducted propeller swallows a greater mass flow. Despite this latter feature, its overall power, or rather its power coefficient  $C_P$ , is lower than the open propeller one, because of the rotor load reduction (see Figure 1.21b).

	Open turbine	Ducted turbine	$\Delta C_P/C_{P,open}$
$C_{T,rot}$	-0.62	-0.62	
$C_T$	-0.62	-0.82	
$C_{T,duct}$	-	-0.20	
$C_P$	-0.46	-0.61	32.61%

Table 1.7: Comparison of the open and ducted turbine performance coefficients.

	Open propeller	Ducted propeller	$\Delta\eta/\eta_{open}$
$C_T$	5.22	5.22	
$C_{T,rot}$	5.22	4.31	
$C_{T,duct}$	-	0.91	
$C_P$	9.90	9.14	
$\eta$	0.53	0.57	7.55%

Table 1.8: Comparison of the open and ducted propeller performance coefficients

axial chord/rotor diameter	$chord_\zeta/D$	0.5
angle between the profile chord and the $\zeta$ axis	$\alpha$	12.7°
tip gap/rotor diameter	$\epsilon/D$	1.019%
leading edge radius/rotor diameter	$\sigma_{LE}/D$	0.625
load magnitude parameter	$\hat{b} = \frac{\sigma_{ad}^2 a_1}{U_\infty \Psi \sigma_{ad}}$	14

Table 1.9: Propeller ducted with a NACA 5415 profile: geometry and operating condition

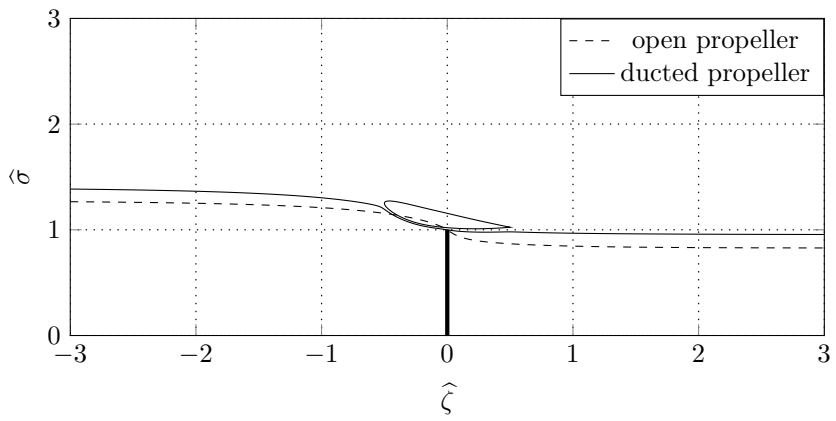


Figure 1.23: Comparison of the open and the ducted propeller slipstream edge.

---

# FLOW ANALYSIS OF OPEN AND DUCTED TURBINES AND COMPARISON WITH CFD

---

## 2.1 Introduction

Although the linearised actuator disk of Rankine (1865) and Froude (1889) represents the oldest analytical performance analysis method for propellers and turbines, it still constitutes a widely diffused and employed design and/or analysis tool, especially in the wind turbine field.

As reported in Chapter 1, in 1962 Wu (1962) introduced the first non-linear actuator disk model and, although he did not carry out numerical calculations, the theoretical basis of his approach still represent a reference in this specific field. Greenberg (1972) and Greenberg and Powers (1970), and Conway (1995, 1998) proposed significant improvements in the analytical and numerical treatment to the theory of Wu (1962). In the previous chapter an extension to ducted rotors of the actuator disk of Conway (1998) has been presented and extensively discussed (see also Bontempo and Manna (2013)). The exact solution furnished in Chapter 1 results from the superposition of ring vortices properly arranged along the duct surface and the wake region. The method can deal with ducts of general shape, wake rotation and rotors characterised by non-uniform, heavy load distributions.

Moreover, the shape of the slipstream and the nonlinear mutual interaction between the duct and the rotor are naturally accounted for and, the method being cost effective, it is well-suited for the design and/or analysis of ducted rotors.

Recent developments in the field of wind turbine wake modelling are directed towards the combined use of actuator disk and CFD techniques (here and after referred to as “CFD actuator disk”). The first works employing numerical actuator disk computations are due to J. N. Sørensen and Myken (1992) and J. N. Sørensen and Kock (1995). In these papers the unsteady and axysymmetric Navier-Stokes equations are solved outside the rotor plane, while the actuator disk is modelled through volume forces computed from tabulated airfoil data. Madsen (1996) investigated the accuracy of the results of the blade element method (see for example Lanzafame and Messina (2013)) comparing them with those obtained solving the Navier-Stokes equations for the flow through an actuator disk. As a preliminary step in the development of a computational method for the analysis of wind turbine farms, Masson, Ammara, and Paraschivoiu (1997) predicted the steady, incompressible and axysymmetric flow around a isolated wind turbine by solving the Navier-Stokes equations. J. N. Sørensen, Shen, and Munduate (1998) combined the actuator disk model with the Navier-Stokes equations to analyse various wake states like the turbulent wake and the vortex ring state. Further numerical improvements are due to Réthoré and N. N. Sørensen (2008). More recent developments of the method are the so-called 3D actuator line or actuator surface model (Dobrev, Massouh, and Rapin 2007; Ivanell 2009; Ivanell, J. N. Sørensen, et al. 2009; Leclerc and Masson 2004; R. Mikkelsen 2003; Shen, J. H. Zhang, and J. N. Sørensen 2009; Sibuet Watters and Masson 2007; J. N. Sørensen and Shen 2002; Troldborg 2008; Troldborg, J. N. Sørensen, and R. Mikkelsen 2010). The CFD actuator disk method is also employed to study several flow cases like yawed rotors (R. F. Mikkelsen and J. N. Sørensen 2000), coned rotors (Madsen and Rasmussen 1999; R. Mikkelsen, J. N. Sørensen, and Shen 2001), wake meandering (Larsen et al. 2008) and wind farm simulations (Ammara, Leclerc, and Masson 2002; Calaf, Meneveau, and Meyers 2010; Castellani and Vignaroli 2013; Ivanell, R. Mikkelsen, et al. 2008; R. Mikkelsen, J. N. Sørensen, Øye, et al. 2007). Finally Hansen, Sorensen, and Flay (2000) applied the CFD actuator disk technique to a ducted wind turbine showing how the method is well suited to capture the main features of the flow. From the foregoing it appears that the actuator disk is still considered a successful and widely used model to simulate open and ducted wind turbine wakes. Nevertheless, accurate and well defined data obtained

from nonlinear actuator disk theory are rarely available, so that meaningful comparisons with CFD actuator disk technique are missing, especially for ducted rotors. This is the focus of the present chapter which deals with open and ducted wind turbines characterised by load distribution and ducts of general shape. In particular, in §2.2 the semi-analytical actuator disk extensively described in Chapter 1 is shortly summarized and in §2.3 it is employed to investigate the characteristics of the flow around ducted wind turbines for different operating conditions. A great attention is also paid to the comparison between open and ducted wind turbines and to the opportunity to get a significant increase of the power extracted by the rotor. Finally, in §2.4 the results of the semi-analytical ducted and open actuator disk model are compared with the results of the more conventional CFD actuator disk model. To this aim the commercial code ANSYS Fluent is used and the actuator disk is modelled with the help of the so-called “fan boundary condition” (ANSYS 2009).

## 2.2 The ducted actuator disk flow model

The following is a theoretical section aimed at synthesizing the ducted actuator disk flow model and at laying down the foundation of the forthcoming sections (more details about the model are reported in Chapter 1).

### 2.2.1 The ducted actuator disk flow model: theoretical background

As already stated in §2.1, the presence of the turbine is modelled through an actuator disk with radius  $\sigma_{ad}$ , center at the origin of a cylindrical coordinate system  $(\zeta, \sigma, \theta)$  and with an arbitrary load radial distribution (see Figure 1.3). The flow is supposed to be steady, axisymmetric, inviscid and incompressible with the free-stream velocity  $U_\infty$  in the  $\zeta$ -axis direction. Since the flow is axisymmetric the vorticity vector can be expressed as

$$\boldsymbol{\omega} = (\omega_\zeta, \omega_\sigma, \omega_\theta) = \left( \frac{1}{\sigma} \frac{\partial(\sigma w)}{\partial \sigma}, -\frac{\partial w}{\partial \zeta}, \frac{\partial v}{\partial \zeta} - \frac{\partial u}{\partial \sigma} \right), \quad (2.1)$$

where  $\mathbf{u} = (u, v, w)$  is the velocity vector. Substituting the definition of the Stokes stream function  $\Psi$

$$u = \frac{1}{\sigma} \frac{\partial \Psi}{\partial \sigma}, \quad v = -\frac{1}{\sigma} \frac{\partial \Psi}{\partial \zeta} \quad (2.2)$$

in (2.1), the  $\theta$ -component of the vorticity becomes

$$\frac{\partial^2 \Psi}{\partial \sigma^2} - \frac{1}{\sigma} \frac{\partial \Psi}{\partial \sigma} + \frac{\partial^2 \Psi}{\partial \zeta^2} = -\omega_\theta \sigma. \quad (2.3)$$

It is noteworthy that, differently from the steady, inviscid, incompressible 2D planar flow, the governing equation of the axisymmetric formulation (2.3) is different from the well-known Poisson equation due to the presence of the minus sign in the first order derivative term.

From an engineering point of view it would definitely be preferable to express the governing equation of the motion (2.3) through the turbine operating condition, i.e. the tip speed ration  $\lambda = \Omega \sigma_{ad} / U_\infty$  and the load radial distribution  $\mathcal{H}(\Psi) = \Delta H_{\text{across the disk}} = H(\Psi)|_{(\zeta > 0, \sigma < \sigma_s(\zeta))} - H_\infty$ , where  $\Omega$  is the angular velocity,  $\sigma_s(\zeta)$  is the slipstream location, and  $H = p/\rho + (u^2 + v^2 + w^2)/2$ . To this end the  $\theta$ -component of the vorticity, in the right-hand side of (2.3), can be elaborated through the momentum equation ( $\mathbf{u} \times \boldsymbol{\omega} = \nabla H$ ) to obtain (Wu 1962)

$$-\omega_\theta \sigma = \begin{cases} \frac{\Omega^2 \sigma^2 - \mathcal{H} \, d\mathcal{H}}{\Omega^2 \, d\Psi} & \text{inside the slipstream,} \\ 0 & \text{outside the slipstream.} \end{cases} \quad (2.4)$$

Finally, replacing (2.4) into (2.3) yields the following nonlinear partial differential equation:

$$\frac{\partial^2 \Psi}{\partial \sigma^2} - \frac{1}{\sigma} \frac{\partial \Psi}{\partial \sigma} + \frac{\partial^2 \Psi}{\partial \zeta^2} = \begin{cases} \frac{\Omega^2 \sigma^2 - \mathcal{H} \, d\mathcal{H}}{\Omega^2 \, d\Psi} & \text{inside the slipstream,} \\ 0 & \text{outside the slipstream.} \end{cases} \quad (2.5)$$

Moreover, equation (2.5) has to be associated to the following conditions at infinity (Wu 1962):

$$\frac{1}{\sigma} \frac{\partial \Psi}{\partial \sigma} \rightarrow U_\infty, \quad \frac{\partial \Psi}{\partial \zeta} \rightarrow 0 \quad \text{as } \zeta \rightarrow -\infty \text{ or } \sigma \rightarrow \infty, \quad (2.6a)$$

$$\frac{\partial \Psi}{\partial \zeta} \rightarrow 0 \quad \text{as } \zeta \rightarrow +\infty. \quad (2.6b)$$

From the definition (2.2) the requirements imposed by the previous conditions can be easily understood, namely the radial velocity has to vanish everywhere at infinity and the axial velocity outside the wake has to reach the free stream velocity value  $U_\infty$ . In the case of a ducted wind turbine a

further boundary condition at the duct wall surface  $C$  has to be imposed (see Chapter 1), that is

$$\Psi = \Psi_0 = \text{const.} \quad \text{on } C, \quad (2.6c)$$

The last condition requires that the duct boundary is a streamsurface so satisfying the classical no-penetration requirement at the solid wall. Finally, once the angular velocity  $\Omega$  (or the tip speed ratio  $\lambda$ ) and load radial distribution  $\mathcal{H}$ , two key physical quantities, have been prescribed, the formulation of the through-flow differential problem (2.5)-(2.6) is complete. Indeed the value of  $\Psi_0$  and the slipstream location  $\sigma_s(\zeta)$ , defining the region inside which the right-hand side of (2.5) does not vanish, are not known in advance and they must be determined as a part of the solution through the iterative method described in the following. Finally, once the through-flow problem (2.5)-(2.6) has been solved, the azimuthal component of the velocity  $w$  is computed through the well-known angular momentum equation

$$\mathcal{H}(\Psi) = H(\Psi) - H_\infty = \Omega\sigma w. \quad (2.7)$$

## 2.2.2 The ducted actuator disk flow model: the solution as superposition of ring vortex

The through-flow around a ducted actuator disk can be described by the superposition of appropriate flow singularities whose strength has to be capable to reproduce the vorticity field  $\omega_\theta(\zeta, \sigma)$  imposed by the disk load  $\mathcal{H}(\Psi)$  (see equation (2.4)) and to satisfy the requirements of the boundary conditions (2.6). Since, inside the slipstream, the only non-zero component of the vorticity of the axisymmetric field  $(u, v, 0)$  is  $\omega_\theta$ , a suitable singularity, generating such a vorticity, is the ring vortex with axis parallel to the  $\zeta$ -axis. In fact it can be shown (see Chapter 1 and references therein) that the stream function of this kind of singularity can be related to the Green function of the linear elliptic operator (2.5). In particular the stream function and the velocity field  $(u', v')$  induced by a single ring vortex of radius  $r$ , strength  $\kappa$  and located at  $\zeta = z$  and  $\sigma = 0$ , are (Basset 1888; Lamb 1932):

$$\frac{\Psi'(\zeta, \sigma)}{\sigma} = \frac{\kappa r}{2} \int_0^\infty e^{-s|\zeta-z|} J_1(sr) J_1(s\sigma) ds, \quad (2.8)$$

$$u'(\zeta, \sigma) = \frac{\kappa r}{2} \int_0^\infty e^{-s|\zeta-z|} {}_sJ_1(sr) J_0(s\sigma) ds, \quad (2.9)$$

$$v'(\zeta, \sigma) = \pm \frac{\kappa r}{2} \int_0^\infty e^{-s|\zeta-z|} {}_sJ_1(sr) J_1(s\sigma) ds, \quad (2.10)$$

where  $J$  is the Bessel function of the first kind and the positive sign is for  $\zeta - z \geq 0$  and vice versa. Once the ring vortex singularity and its properties have been defined, it can be used to model the duct and the turbine wake flow. More in details, following the classical approach of Martensen (1959), the flow around the duct is described by a sheet of ring vortex covering the profile and with an appropriate density strength  $\gamma_d(c)$ , where  $c$  is the curvilinear abscissa along the section of the duct (see Figure 1.2). In turn, to reproduce a vortical region like the turbine wake, a continuum surface singularity distribution covering the wake space region is introduced. Defining  $\gamma_{ad}(\zeta, \sigma)$  as the actuator disk wake ring vortex density strength and integrating equation (2.8) over the wake and over the duct profile, leads to the exact solution for the overall flow (see Chapter 1):

$$\frac{\Psi(\zeta, \sigma)}{\sigma} = \frac{1}{2} \int_0^\infty \int_0^{\sigma_s(z)} \int_0^\infty e^{-s|\zeta-z|} \gamma_{ad}(z, r) r J_1(sr) J_1(s\sigma) ds dr dz + \underbrace{\frac{1}{2} \oint_C \int_0^\infty \gamma_d(c) r(c) e^{-s|\zeta-z|} J_1(sr(c)) J_1(s\sigma) ds dc}_{\frac{\Psi_d(\zeta, \sigma)}{\sigma}} + \frac{U_\infty \sigma}{2}. \quad (2.11)$$

The above equation is the exact solution of the coupled flow and the three terms on the right-hand side represent the contribution to the stream function due to the wake ring vortex, to the duct ring vortex and to the free stream, respectively. Obviously, in an open turbine configuration the second term vanishes.

As already stated the singularities have to be capable to reproduce the vorticity field  $\omega_\theta(\zeta, \sigma)$  imposed by the disk load  $\mathcal{H}(\Psi)$  and to satisfy the boundary conditions (2.6). It can be shown (see again Chapter 1 and references therein for details) that in order to reproduce the vortical turbine wake the vorticity density strength  $\gamma_{ad}(\zeta, \sigma)$  has to be equal to the tangential vorticity  $\omega_\theta(\zeta, \sigma)$ . This result is fully justifiable by the fact that the only non-zero component of the vorticity of the through-flow field  $(u, v, 0)$  is  $\omega_\theta$ . In turn, a ring vortex with axis parallel to the  $\zeta$ -axis, being a closed and circular line vortex, has, by definition, a vorticity strength vector always tangent to it and so directed in the  $\theta$ -direction. Obviously, the single ring vortex solution (2.8)–(2.10) satisfies the condition at infinity (2.6a) and (2.6b). Due to the linearity of (2.6a) and (2.6b) they are also satisfied by a superposition of ring vortices like those used in the wake of the turbine and at the duct surface. It can be shown (Lewis 1991; Martensen 1959) that the no-penetration requirement along the solid wall is satisfied by the homoge-

neous Dirichlet boundary condition on the tangent to the wall velocity just beneath the duct vorticity sheet. To this end the  $\gamma_d(c)$  distribution has to satisfy the following Fredholm second kind integral equation (see Chapter 1):

$$-\frac{1}{2}\gamma_d(c) + \oint_C k(c, \tilde{c})\gamma_d(\tilde{c}) d\tilde{c} + (U_\infty + u_{ad}(c)) \cos \beta(c) + v_{ad}(c) \sin \beta(c) = 0, \quad (2.12)$$

where  $\beta(c)$  is the local profile slope and  $k(c, \tilde{c})$  is the velocity parallel to the surface, at  $c$ , induced by a ring vortex of unit strength located at  $\tilde{c}$ . The first term in (2.12) is precisely half the velocity jump across the sheet, the second is the velocity induced in  $c$  by all the duct vortices, and the third is the contribution of the wake ring vortex distribution and of the free stream in the tangent to the wall direction. More in detail the velocity  $u_{ad}(c)$  and  $v_{ad}(c)$  can be evaluated integrating equations (2.9) and (2.10) over the wake space region, respectively (see Chapter 1). Furthermore, in order to mimic the lifting behaviour induced by the viscosity in an inviscid formulation, the  $\gamma_d(c)$  distribution has to satisfy the Kutta condition at the trailing edge, too.

### 2.2.3 The ducted actuator disk flow model: solution strategy

A close inspection to equation (2.11) readily shows that, the direct evaluation of  $\Psi$  through (2.11) is prevented due to the implicitness of the solution, i.e. the unknowns  $\sigma_s(\zeta)$ ,  $\gamma_{ad}(\zeta, \sigma)$  and  $\Psi_d(\zeta, \sigma)$  depend upon the Stokes stream function  $\Psi$ . For this reason an iterative solution strategy was implemented and detailed in Chapter 1. Assuming that the load is a continuous function, the procedure starts by expressing the load  $\mathcal{H}$  through the following algebraic polynomial:

$$\mathcal{H}(\Psi) = \sum_{m=0}^M a_m \left( \frac{\Psi}{\Psi_{\sigma_{ad}}} \right)^m, \quad (2.13)$$

where  $\Psi_{\sigma_{ad}}$  is the stream function evaluated at  $(\zeta = 0, \sigma = \sigma_{ad})$ . Further, assuming  $\mathcal{H}(\Psi)$  to be  $C^1$  continuous, equations (2.13) and (2.4) yield:

$$\frac{\omega_\theta(\zeta, \sigma)}{\sigma} = \left[ \frac{1}{\lambda^2 U_\infty^2} \left( \frac{\sigma_{ad}}{\sigma} \right)^2 \sum_{m=0}^M a_m \left( \frac{\Psi}{\Psi_{\sigma_{ad}}} \right)^m - 1 \right] \sum_{m=1}^M \frac{m a_m}{\Psi_{\sigma_{ad}}} \left( \frac{\Psi}{\Psi_{\sigma_{ad}}} \right)^{m-1}. \quad (2.14)$$

In order to perform the exact integration of the two inner actuator disk integrals in equation (2.11), the tangential component of the vorticity can be expressed through the following polynomial expansion (Conway 1998):

$$\frac{\omega_\theta(\zeta, \sigma)}{\sigma} = \sum_{n=0}^N A_n(\zeta) \left[ 1 - \left( \frac{\sigma}{\sigma_s(\zeta)} \right)^2 \right]^n, \quad (2.15)$$

leading to

$$\begin{aligned} \Psi(\zeta, \sigma) &= \Psi_d(\zeta, \sigma) \\ &+ \sigma \int_0^\infty \sum_{n=0}^N A_n(z) 2^{n-1} n! \sigma_s^{2-n}(z) I_{(-(n+1), n+2, 1)}(\sigma_s(z), \sigma, \zeta - z) dz, \end{aligned} \quad (2.16)$$

$$u_{ad}(\zeta, \sigma) = \int_0^\infty \sum_{n=0}^N A_n(z) 2^{n-1} n! \sigma_s^{2-n}(z) I_{(-n, n+2, 0)}(\sigma_s(z), \sigma, \zeta - z) dz, \quad (2.17)$$

$$v_{ad}(\zeta, \sigma) = \pm \int_0^\infty \sum_{n=0}^N A_n(z) 2^{n-1} n! \sigma_s^{2-n}(z) I_{(-n, n+2, 1)}(\sigma_s(z), \sigma, \zeta - z) dz, \quad (2.18)$$

for the overall flow stream function and the actuator disk induced velocities, respectively. The integrals  $I_{(\xi, \mu, \nu)}$  appearing in (2.16)-(2.18), with  $\xi$ ,  $\mu$  and  $\nu$  integers, are of the following type:

$$I_{(\xi, \mu, \nu)} = \int_0^\infty e^{-s|\zeta-z|} s^\xi J_\mu(sr) J_\nu(s\sigma) ds, \quad (2.19)$$

and they can be expressed in terms of complete elliptic integrals and Heuman Lambda function through the recursive scheme detailed in Conway (2000).

The evaluation of  $\Psi$  through equation (2.16) still requires the knowledge of  $\Psi_d(\zeta, \sigma)$  (see equation (2.11)) which depends on the duct ring vortex density strength  $\gamma_d(c)$ . In order to make the duct boundary a stream surface, the  $\gamma_d(c)$  distribution has to satisfy equation (2.12). Dividing the profile in  $M_p$  panels with length  $\Delta c_n$  and using the trapezium rule on each of them, yields the following system of  $M_p \times M_p$  linear algebraic equations:

$$\sum_{n=1}^{M_p} K(c_m, c_n) \gamma_d(c_n) = -(U_\infty + u_{ad,m}) \cos \beta_m - v_{ad,m} \sin \beta_m \quad m = 1, \dots, M_p. \quad (2.20)$$

In the above equations  $u_{ad,m}$  and  $v_{ad,m}$  have to be evaluated through (2.17)-(2.18), while the entries of matrix  $K$  are equal to  $k(c_m, c_n) \Delta c_n$  when  $n \neq m$

and  $k(c_m, c_m)\Delta c_m - \frac{1}{2}\gamma_d(c_m)$  for  $n = m$ . The full expressions for the  $k$  coefficients are detailed in Chapter 1. The implementation of the Kutta condition, deeply described in the first chapter of this thesis, is not relevant to the present discussion and it will be omitted for the sake of brevity. Finally, the inner integral in the definition of  $\Psi_d$  (see equation (2.11)) can be exactly solved (Gradshteyn and Ryzhik 1980) so that, using the trapezium rule, the following expression for  $\Psi_d$  can be obtained (Bontempo and Manna 2013):

$$\Psi_d(\zeta, \sigma) = \sum_{m=1}^{M_P} \frac{\gamma_d(c_m)\Delta c_m \sqrt{\sigma\sigma_m}}{2\pi} Q_{1/2}(\omega_m) + \frac{U_\infty \sigma^2}{2}, \quad (2.21)$$

to be used in (2.16). In equation (2.21),  $Q_{1/2}$  is the Legendre function of the second kind and  $\omega_m = 1 + [(\sigma_m - \sigma)^2 + (\zeta - \zeta_m)^2]/(2\sigma_m\sigma)$ .

The integration of (2.16)-(2.18) presents a further difficulty, i.e. the  $\sigma_s(\zeta)$  distribution is also unknown and must be determined as a part of the solution. To overcome this problem the following iterative procedure was proposed. First of all, since the Stokes stream function is constant on  $\sigma_s(\zeta)$ , equation (2.16) reduces thereon to the following nonlinear integral equation for  $\sigma_s(\zeta)$ :

$$\begin{aligned} \Psi(0, \sigma_{ad}) &= \frac{U_\infty \sigma_s^2(\zeta)}{2} + \Psi'_d(\zeta, \sigma_s(\zeta)) + \\ \sigma_s(\zeta) \int_0^\infty \sum_{n=0}^N A_n(z) 2^{n-1} n! \sigma_s^{2-n}(z) I_{(-(n+1), n+2, 1)}(\sigma_s(z), \sigma_s(z), \zeta - z) dz \end{aligned} \quad (2.22)$$

with  $\Psi'_d = \Psi_d - \frac{1}{2}U_\infty \sigma^2$ .

To summarize, the procedure consists of the following steps:

1. Compute and store the matrix  $K$  (which merely depends upon the duct geometry) and its LU decomposition.
2. Assume that provisional values of  $\gamma_d(c_m)$  are available from the previous iteration.
3. Assume that provisional values of  $\sigma_s(\zeta)$  and  $\{A_n(\zeta)\}_{n=0, N}$  are available from the previous iteration at  $n_z$  axial station.
4. Mesh the wake through a  $n_{zs} \times n_{rs}$  grid, where  $n_{zs}$  and  $n_{rs}$  are the number of axial and radial stations, respectively.

5. Numerically integrate (2.16) in the  $\zeta$  direction with an adaptive Simpson quadrature scheme (Lyness 1970) thus computing  $\Psi$  at all grid points.
6. Compute  $\omega_\theta$  at all grid points through equation (2.14).
7. With the help of a least-squares minimization procedure, parametrize the  $\omega_\theta$  distributions, computed at step 9, with a new set of  $\{A_n(\zeta)\}_{n=0,N}$ .
8. Compute the axial and radial velocities induced by the actuator disk (equations (2.17) and (2.18)) at the profile.
9. Update the right-hand side of (2.20) and consequently  $\gamma_d(c_m)$  for  $m = 1, \dots, M_P$ .
10. From (2.22), the new  $\sigma_s(\zeta)$  is re-evaluated through:

$$\sigma_s(\zeta) = \sqrt{\left(\frac{\Psi'_d(\zeta, \sigma_s(\zeta))}{\sigma_s(\zeta)U_\infty} + \frac{I(\zeta, \sigma_s(\zeta))}{U_\infty}\right)^2 + \frac{2\Psi(0, \sigma_{ad})}{U_\infty}} - \frac{\Psi'_d(\zeta, \sigma_s(\zeta))}{\sigma_s(\zeta)U_\infty} - \frac{I(\zeta, \sigma_s(\zeta))}{U_\infty},$$

where

$$\begin{aligned} I(\zeta, \sigma_s(\zeta)) &= \\ &= \int_0^\infty \sum_{n=0}^N A_n(z) 2^{n-1} n! \sigma_s^{2-n}(z) I_{(-(n+1), n+2, 1)}(\sigma_s(z), \sigma_s(z), \zeta - z) dz. \end{aligned}$$

11. Go to item 5 until convergence of the slipstream  $\sigma_s(\zeta)$  is reached.

At the first iteration  $\gamma_d(c_m)$ ,  $\sigma_s(\zeta)$  and  $\Psi$  are calculated ignoring the presence of the disk. The solution procedure for the open rotor configuration can be simply obtained setting  $\Psi'_d(\zeta, \sigma_s(\zeta)) = 0$  in equation (2.22) and dropping points 3, 4, 11 and 12 from the previous list.

## 2.3 Flow analysis of open and ducted turbines

In the following the method described in §2.2 is employed to investigate the characteristics of the flow around open and ducted wind turbines. Emphasis is given to the comparison between ducted and open rotors to exploit the

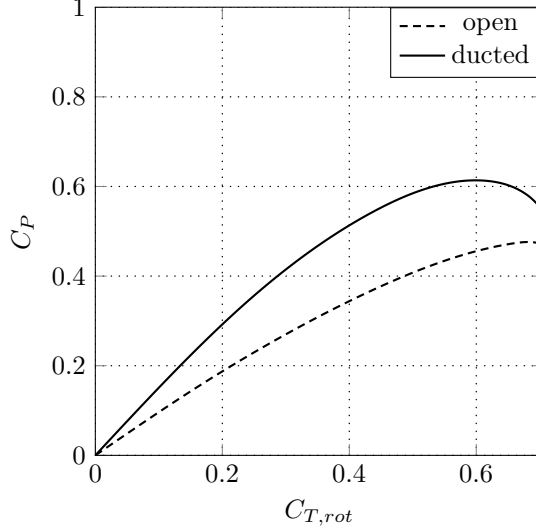


Figure 2.1: Computed power coefficient versus rotor thrust coefficient for open and ducted turbines.

beneficial effects that could arise ducting the turbine. As customary, the following definition are used for the thrust and power coefficients:

$$C_T = \frac{T}{\frac{1}{2}\rho U_\infty^2 \pi \sigma_{ad}^2}, \quad C_P = \frac{P}{\frac{1}{2}\rho U_\infty^3 \pi \sigma_{ad}^2},$$

where  $T$  and  $P$  are the magnitudes of the thrust and the power experienced by the device, respectively. In particular for the ducted wind turbine the total thrust can be divided into the duct and the rotor thrust so that the overall thrust coefficient becomes

$$C_T = C_{T,rot} + C_{T,duct}. \quad (2.23)$$

For the sake of simplicity, an actuator disk without slipstream rotation ( $\lambda \rightarrow \infty$ ) and with a parabolic load radial distribution will be analysed. In particular the load  $\mathcal{H}$  will be expressed as

$$\mathcal{H}(\Psi) = a_1 \left[ \frac{\Psi}{\Psi_{\sigma_{ad}}} - \left( \frac{\Psi}{\Psi_{\sigma_{ad}}} \right)^2 \right] = \frac{U_\infty \Psi_{\sigma_{ad}} \hat{b}}{\sigma_{ad}^2} \left[ \frac{\Psi}{\Psi_{\sigma_{ad}}} - \left( \frac{\Psi}{\Psi_{\sigma_{ad}}} \right)^2 \right], \quad (2.24)$$

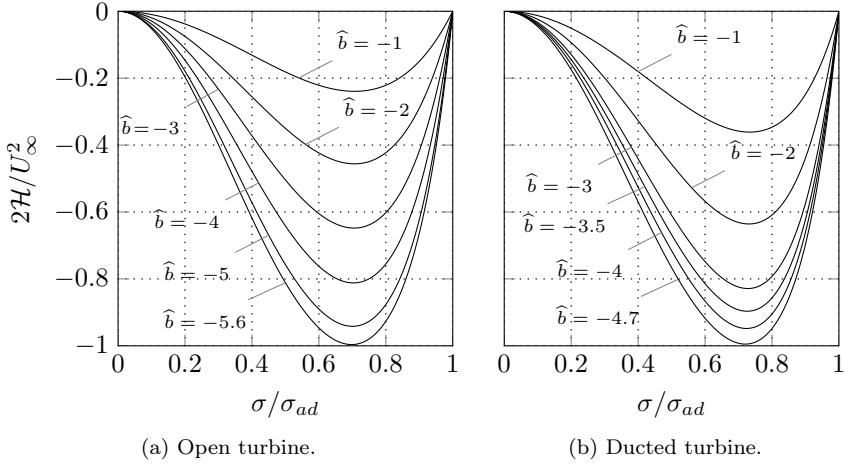


Figure 2.2: Load radial distributions related to simulations reported in Fig 2.1.

chord/rotor diameter	$chord/D$	0.513
angle between the chord and the axial direction	$\alpha$	$-5.0^\circ$
tip gap/rotor diameter	$\epsilon/D$	1.039%
leading edge radial position/rotor diameter	$\sigma_{LE}/D$	0.559
leading edge axial position/rotor diameter	$\zeta_{LE}/D$	-0.15

Table 2.1: Turbine ducted with a NACA 5415 profile: geometry.

where  $\hat{b} = \sigma_{ad}^2 a_1 / U_\infty \Psi_{\sigma_{ad}}$  is a load magnitude parameter (Conway 1998).

Recall that for an actuator disk without wake rotation the pressure jump across the disk is directly related to the work extracted by the turbine through

$$W(\sigma) = -\mathcal{H}(0, \sigma) = -\frac{\Delta p_{ad}(\sigma)}{\rho}. \quad (2.25)$$

Consequently, the extracted power becomes:

$$P = -\int_0^{\sigma_{ad}} \frac{\Delta p_{ad}(\sigma)}{\rho} \rho u(0, \sigma) 2\pi\sigma \, d\sigma = -\int_0^{\sigma_{ad}} \frac{\Delta p_{ad}(\sigma)}{\rho} \, d\dot{m}, \quad (2.26)$$

where  $d\dot{m}$  is the mass flow rate passing through the elemental area  $2\pi\sigma d\sigma$ .

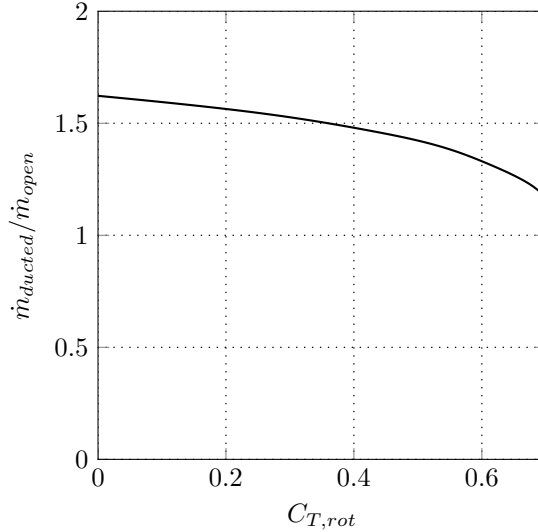


Figure 2.3: Computed mass flow ratio  $\dot{m}_{ducted}/\dot{m}_{open}$ .

As well known from the classical momentum theory, an increase in the rotor thrust, i.e. in the pressure jump across the disk, leads to a decrease in the mass flow swallowed by the rotor. The conflicting trend of those two quantities suggest the presence of an optimum for the power extraction. In the linearised actuator disk theory applied to a bare turbine this optimum is the well-known Lanchester-Betz-Joukowsky maximum for the power coefficient corresponding to  $C_P = 16/27$ . In the nonlinear open actuator disk case the situation is more involved; in fact the relevant phenomenon of the wake divergence has to be accounted for. These properties make it impossible to attain an explicit and analytical solution of the governing equation and, therefore, more complex analysis methods have to be employed. Figure 2.1 reports the power coefficient obtained employing the nonlinear actuator disk method of §2.2 and the parabolic load radial distributions (see equation (2.24)) reported in Figure 2.2a.

Consider now a ducted and open turbine characterised by the same rotor thrust; in the former case under appropriate circumstances the duct can increase the mass flow swallowed by the rotor leading to an enhanced power extraction. As stated by de Vries (1979) the mass flow increase is due to the sectional lift of the duct (the overall lift is zero for symmetry reason) and to

the related circulation which induces an increased velocity through the area enclosed by the duct. Figure 2.1 also shows the power coefficient of a turbine ducted with a NACA5415 (see Table 2.1 for geometrical details) obtained through the nonlinear actuator disk (§2.2) characterised by the parabolic load radial distributions reported in Figure 2.2b. For each value of the rotor thrust coefficient the ducted turbine achieves a higher value of the power in comparison with the open turbine. Finally, Figure 2.3 shows the ratio between the mass flow swallowed by the ducted turbine ( $\dot{m}_{duct}$ ) and the one of the bare turbine ( $\dot{m}_{open}$ ) thus explaining the enhanced power extraction of the ducted turbine due to the increased mass flow passing through the rotor.

It is noteworthy that Figures 2.1, 2.2 and 2.3 span the entire range of validity of the actuator disk theory. More precisely, this means that the rotor load can vary from zero to a given maximum value corresponding to a vanishing velocity at downstream infinity. In fact the maximum value of the load coefficient  $\hat{\mathcal{H}} = 2\mathcal{H}/U_\infty^2 = -1$ , achieved in Figure 2.2 for  $\hat{b} = -5.6$  and  $\hat{b} = -4.7$ , yields a zero value of the velocity at downstream infinity. In order to prove the previous statement consider that, for an actuator disk without slipstream rotation, the static pressure at downstream infinity  $p(+\infty, \sigma)$  is assumed to be equal to  $p_\infty$  and thus the load coefficient can be expressed as

$$\hat{\mathcal{H}} = \left( \frac{u(+\infty, \sigma)}{U_\infty} \right)^2 - 1.$$

The above equation implies that when  $u(+\infty, \sigma) \rightarrow 0$  the load coefficient  $\hat{\mathcal{H}} \rightarrow -1$  which proves the claim. Finally, the robustness of the iterative procedure, and more in general of the method, is demonstrated by the fact that full convergence of the iterative procedure has always been achieved in the entire range of validity of the actuator disk theory and in particular for heavy loads.

## 2.4 Error analysis and comparison with CFD

As anticipated in the introduction, one of the most diffused and studied wind turbine wake analysis tool combines a CFD flow solver with an actuator disk model simulating the presence of the rotor. In this approach the Navier-Stokes or Euler equations are typically solved, while the rotor geometry and the flow through it are modelled. The turbine effects are parametrised with a distribution of surface forces acting in the rotor plane which are determined

<i>#case</i>	$n_z$	$n_{zs}$	$n_{rs}$	$\widehat{b} = \sigma_{ad}^2 a_1 / U_\infty \Psi_{\sigma_{ad}}$
SAOT-1	51	11	11	-5.0
SAOT-2	101	51	51	-5.0
SAOT-3	201	101	101	-5.0
SAOT-4	401	201	201	-5.0
SAOT-5	501	251	251	-5.0

Table 2.2: Open rotor configuration: numerical parameters and operating condition.

using a blade-element method. With the CFD actuator disk many relevant physical phenomena, like the generation and downstream propagation of the blade wakes are disregarded. Nevertheless, this methodology represents a valid compromise between the very costly three dimensional rotor geometry resolved approach, and the over simplified one dimensional model. The available literature undoubtedly shows that the CFD actuator disk is still a widely diffused method, a fact that fully justify the forthcoming study based on the implementation of the so-called “fan boundary condition” in the commercial CFD code ANSYS Fluent (ANSYS 2009). With this approach the user directly inputs a radial distribution of the pressure jump across the disk which simulates the effect of the turbine energy extraction.

The first two parts of the present section are therefore devoted to the quantification of the numerical uncertainties characterizing the semi-analytical procedure and the CFD actuator disk method, while in the last part a thorough comparison of the results is carried out.

### 2.4.1 The semi-analytical actuator disk method: error analysis

Although equation (2.11) represents the exact solution of the differential problem (2.5)–(2.6), the direct evaluation of the stream function  $\Psi(\zeta, \sigma)$  is carried out through a semi-analytical procedure which introduces three (four for ducted rotors) numerical parameters, i.e.  $n_z, n_{zs}, n_{rs}$  ( $M_p$ ), whose meaning is detailed in §2.2.3. In order to investigate the effects of these parameters onto the solution, they are made to vary in a five-levels range. For the sake of clarity and conciseness only the combinations of parameters obtained simultaneously increasing each of them are analysed (see Table 2.2 for details). Table 2.3 reports the relative errors of the global performance

#case	Performance coefficients relative error		Axial velocity $L^2$ discrete norm of the error		
	$C_T$	$C_P$	$u _{\zeta=-1}$	$u _{\zeta=0}$	$u _{\zeta=1}$
SAOT-1	2.727E-3	8.899E-3	7.614E-4	4.027E-3	5.473E-3
SAOT-2	3.882E-4	2.731E-4	5.405E-4	3.552E-3	4.498E-4
SAOT-3	2.826E-4	3.714E-4	5.401E-4	2.120E-4	4.417E-4
SAOT-4	1.560E-5	2.212E-5	1.189E-5	1.800E-5	2.455E-5
SAOT-5	0	0	0	0	0

Table 2.3: Open turbine: error analysis.

#case	$n_z$	$n_{zs}$	$n_{rs}$	$M_p$	$\hat{b} = \sigma_{ad}^2 a_1 / U_\infty \Psi_{\sigma_{ad}}$
SADT-1	51	11	11	100	-2.0
SADT-2	101	51	51	200	-2.0
SADT-3	201	101	101	400	-2.0
SADT-4	401	201	201	600	-2.0
SADT-5	501	251	251	800	-2.0

Table 2.4: Turbine ducted with a NACA 5415 profile: numerical parameters and operating condition.

coefficients along with the  $L^2$  discrete norm of the error obtained comparing the axial velocity profiles at  $\zeta = -1, 0, 1$ . All errors are computed assuming SAOT-5 as reference.

For the ducted configuration (see Table 2.4) the influence of the number of panels  $M_p$  is also investigated. In particular, Tables 2.5 and 2.6 present the relative errors of the performance coefficients and the  $L^2$  discrete norm of the errors of the axial velocity at different axial stations for a turbine ducted with a NACA 5415 profile (see Table 2.1 for geometrical details). Obviously, for the ducted configuration, all errors are computed assuming SADT-5 as reference.

## 2.4.2 The CFD actuator disk method: error analysis

As already mentioned, the CFD actuator disk analysis is carried out through the commercial CFD code ANSYS Fluent in which the actuator disk is modelled with the help of the so-called ‘‘fan boundary condition’’ (ANSYS

<i>#case</i>	Performance coefficients relative error			
	$C_T$	$C_{T,rot}$	$C_{T,duct}$	$C_P$
SADT- 1	5.471E-2	1.117E-2	0.145	2.305E-2
SADT- 2	2.088E-2	8.502E-3	4.654E-2	1.726E-2
SADT- 3	6.628E-3	2.825E-3	1.451E-2	5.742E-3
SADT- 4	2.180E-3	9.314E-4	4.768E-3	1.903E-3
SADT- 5	0	0	0	0

Table 2.5: Turbine ducted with a NACA 5415: performance coefficients error analysis.

<i>#case</i>	Axial velocity $L^2$ discrete norm of the error		
	$u _{\zeta=-1}$	$u _{\zeta=0}$	$u _{\zeta=1}$
SADT- 1	3.736E-3	1.313E-2	5.326E-3
SADT- 2	2.916E-3	1.032E-2	4.564E-3
SADT- 3	1.076E-3	3.450E-3	1.623E-3
SADT- 4	3.212E-4	1.137E-3	5.329E-4
SADT- 5	0	0	0

Table 2.6: Turbine ducted with a NACA 5415: axial velocity error analysis.

<i># case</i>	representative grid size/ $\sigma_{ad}$	<i># cells</i>	<i># cells</i>
	inner domain	inner domain	full-size domain
CFDOT-1	0.04	31250	78310
CFDOT-2	0.02	125000	224400
CFDOT-3	0.01	500000	829330

Table 2.7: Characteristics of the mesh employed in the CFD grid dependence analysis for open turbine.

# case	representative grid size/ $\sigma_{ad}$	# cells	# cells
	inner domain	inner domain	full-size domain
CFDDT-1	0.04	30647	75072
CFDDT-2	0.02	121570	218180
CFDDT-3	0.01	494375	716048

Table 2.8: Characteristics of the mesh employed in the CFD grid dependence analysis for ducted turbine.

#case	Axial velocity $L^2$			Radial velocity $L^2$		
	discrete norm of the error			discrete norm of the error		
	$u _{\zeta=-1}$	$u _{\zeta=0}$	$u _{\zeta=1}$	$v _{\zeta=-1}$	$v _{\zeta=0}$	$v _{\zeta=1}$
CFDOT-1	9.115E-5	2.409E-3	8.591E-3	1.176E-4	6.100E-4	9.309E-3
CFDOT-2	2.252E-5	7.285E-4	2.928E-3	3.276E-5	1.990E-4	3.257E-3
CFDOT-3	0	0	0	0	0	0

Table 2.9: Open turbine: mesh dependence analysis.

#case	Axial velocity $L^2$			Radial velocity $L^2$		
	discrete norm of the error			discrete norm of the error		
	$u _{\zeta=-1}$	$u _{\zeta=0}$	$u _{\zeta=1}$	$v _{\zeta=-1}$	$v _{\zeta=0}$	$v _{\zeta=1}$
CFDDT-1	2.050E-3	4.843E-3	7.167E-3	1.175E-3	4.200E-3	1.384E-3
CFDDT-2	5.027E-4	1.245E-3	2.191E-3	2.843E-4	1.369E-3	4.894E-3
CFDDT-3	0	0	0	0	0	0

Table 2.10: Turbine ducted with a NACA 5415: mesh dependence analysis.

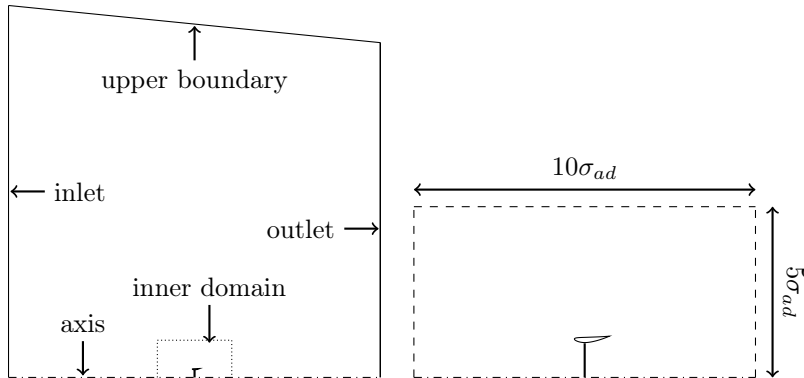


Figure 2.4: Computational domain. Left: full size; right: inner domain.

2009). The “fan boundary condition” is a lumped parameter model that can be used to determine the impact of a fan and/or a turbine with known characteristics upon some larger scale flow field. In fact, as anticipated, the fan model does not provide an accurate description of the detailed flow through the fan blades. Instead, it predicts the amount of flow through the rotor which is considered to be infinitely thin and therefore represented as an interface between cells. Thus the fan is a special type of internal face zone (where the faces are line segments in 2D or triangles/quadrilaterals in 3D). The pressure jump across the rotor can be freely specified as a function of the velocity through the fan or of the rotor span. In the first case, the relationship between the pressure rise and the velocity through the rotor may be a polynomial, a piecewise-polynomial, or a user-defined function. In the case of a polynomial, the relationship is of the form

$$\Delta p_{ad} = \sum_{j=1}^J f_j u^{j-1},$$

where  $f_j$  are the pressure-jump polynomial coefficients and  $u$  is the magnitude of the local fluid velocity normal to the rotor. In the second case, the fan boundary condition allows the user to directly input the pressure jump across the disk as a function of the radial distance from the centre of the rotor, i.e.

$$\Delta p_{ad} = g(\sigma) \quad 0 < \sigma < \sigma_{ad}. \quad (2.27)$$

In the simplified case of a rotor without a wake rotation the pressure jump across the disk is directly related to the radial distribution of the load  $\mathcal{H}$ , as reported in equation (2.25). For this reason, in the present subsection, the load radial distributions obtained in the reference cases SAOT-5 and SADT-5 are prescribed at the actuator disk plane through (2.27) for the open and ducted configurations, respectively.

As detailed in Tables 2.7 and 2.8, the error analysis is carried out increasing the mesh density in the region of interest. The 2D computational domain used in ANSYS Fluent to simulate the steady, axisymmetric and inviscid flow around an open or a ducted actuator disk is shown in Figure 2.4. The inlet and outlet boundaries are located at a distance of  $25\sigma_{ad}$  from the actuator disk plane, while the upper boundary is placed at  $50\sigma_{ad}$  from the  $\zeta$  axis. At the inlet boundary a uniform axial velocity  $U_\infty$  is imposed, while both the upper and outlet edges of the computational domain are treated as uniform pressure boundaries. The domain is discretized with a structured curvilinear mesh characterized by a finer spacing in the  $10\sigma_{ad} \times 5\sigma_{ad}$  inner domain highlighted in Figure 2.4. Finally, the mesh is smoothly coarsened moving towards the outer edges of the domain. The extension of the inner domain was also investigated through a grid dependence study (results not shown). Time integration is performed with a pressure correction method, while spatial discretization is carried out with a second order scheme.

The characteristics of the mesh employed in the grid dependence analysis, both for the open and ducted configurations, are listed in Tables 2.7 and 2.8 (the grid size has to be intended as area averaged) while the  $L^2$  discrete norm of the error in the axial and radial velocities are detailed in Tables 2.9 and 2.10.

### 2.4.3 Semi-analytical and CFD actuator disk methods: comparison of the results

Once the error analyses have been performed, the results of the so-called “reference cases”, i.e. SAOT-5, SADT-5, CFDOT-3, and CFDDT-3 which are obtained using the richest combination of the selected numerical parameters (see Tables 2.2, 2.4, 2.7 and 2.8), can be compared one another. This allows to verify the closeness of the semi-analytical and CFD actuator disk results, both for the open and ducted configurations. The aim of this comparison is two-fold. Firstly, it can be used to test how well the fan boundary condition works in a set up representative of a realistic turbine configuration. Secondly, it opens the perspective to control the relevant numerical issues by allowing the extraction of detailed information about the local errors.

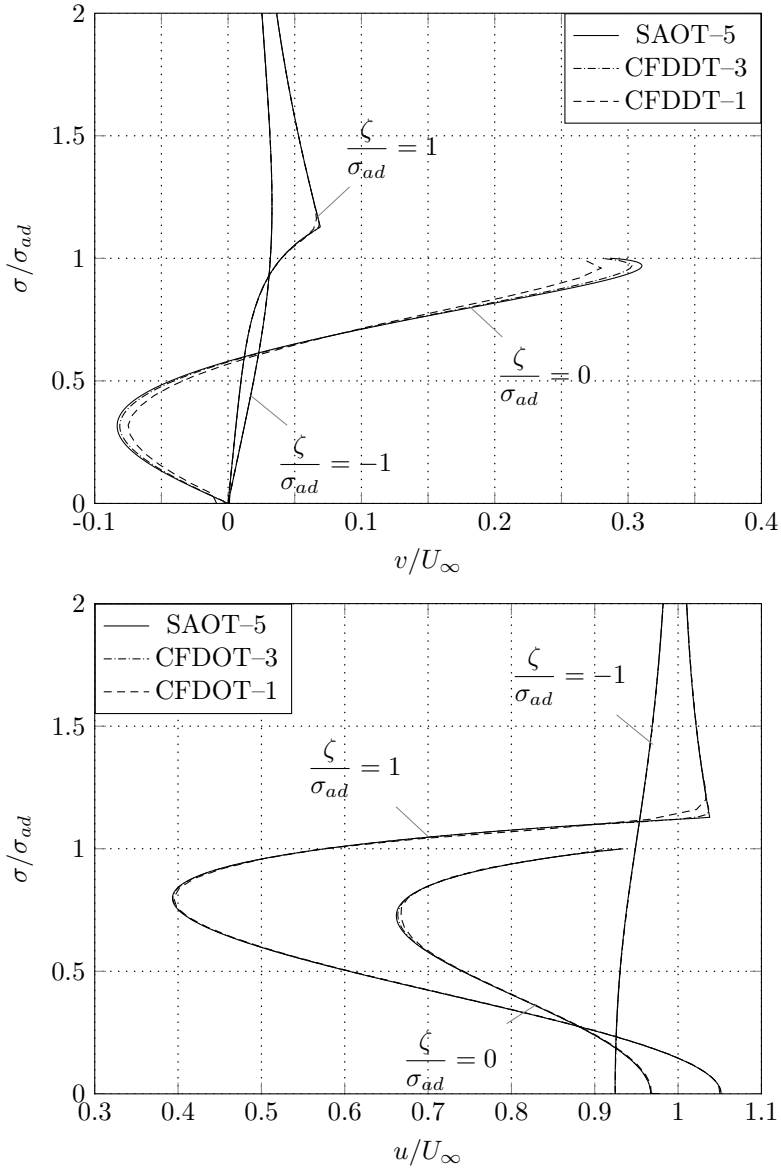


Figure 2.5: Open turbine: comparison of the radial (top) and axial (bottom) velocity profiles obtained through the semi-analytical (SAOT-5) and CFD (CFDDT-3 and CFDDT-1) actuator disk methods.

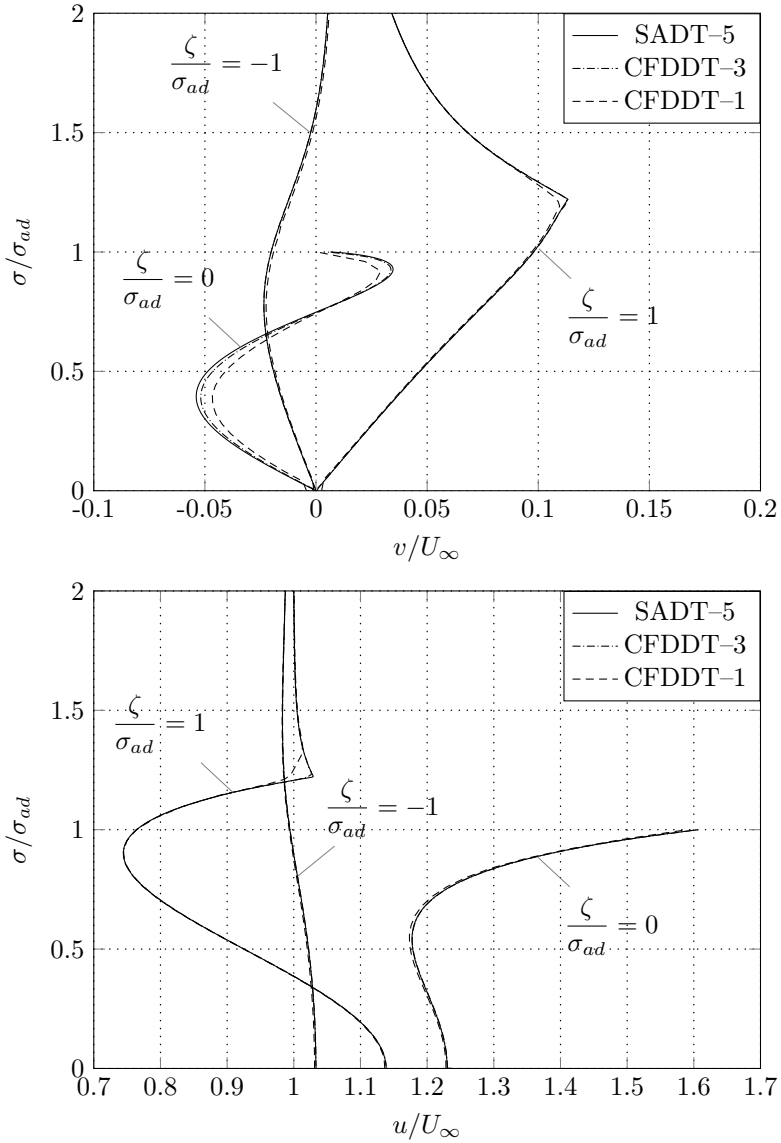


Figure 2.6: Turbine ducted with a NACA5415: comparison of the radial (top) and axial (bottom) velocity profiles obtained through the semi-analytical (SADT-5) and the CFD (CFDDT-3 and CFDDT-1) actuator disk methods.

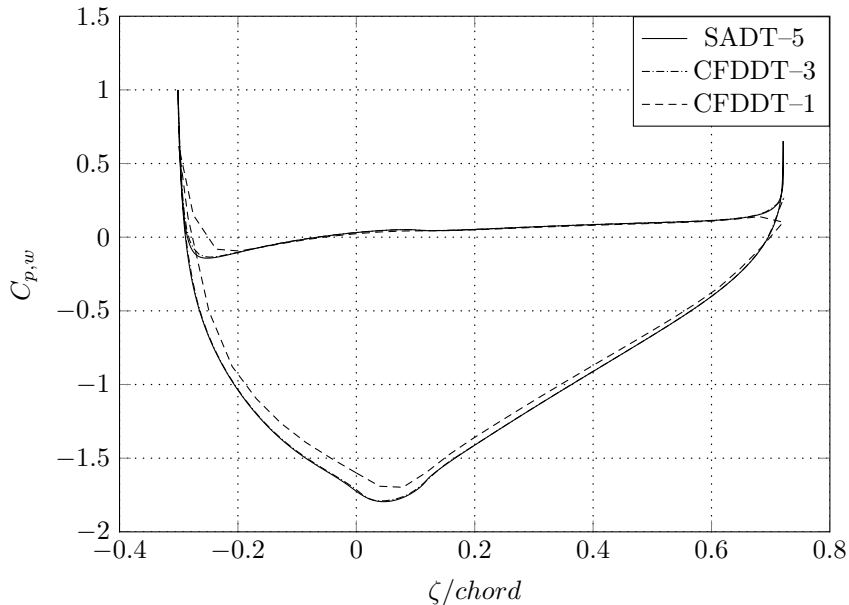


Figure 2.7: Turbine ducted with a NACA5415: comparison of the wall pressure coefficient profile obtained through the semi-analytical (SADT-5) and the CFD (CFDDT-3 and CFDDT-1) actuator disk methods.

In particular, in Chapter 1 the semi-analytical actuator disk method was validated at downstream infinity, i.e.  $\zeta \rightarrow +\infty$ , with the help of asymptotic relations. Conversely, the comparison proposed hereafter allows to validate the procedure at all points of the domain and not only at downstream infinity. Figures 2.5 and 2.6 show the radial profiles of the radial and axial velocities at different axial stations obtained with the semi-analytical and CFD actuator disk models. First of all, the typical turbine wake divergence can be recognized from the velocity distributions. In fact, not only is the radial component always positive in the slipstream, but also the deficit of the axial component increases in the streamwise direction. Furthermore, comparing the radial velocity profile of the open and the ducted turbine, the role played by the duct can be further outlined. In fact, in the open rotor case, the radial velocity is always positive both ahead ( $\zeta/\sigma_{ad} = -1$ ) and behind ( $\zeta/\sigma_{ad} = 1$ ) the disk, which means that the dividing streamline  $\sigma_s(\zeta)$  is always divergent. Instead, in the ducted configuration, the presence

		$\zeta = -1.0$	$\zeta = 0.0$	$\zeta = 1.0$
open	radial velocity	1.119E-5	3.201E-3	1.319E-4
	axial velocity	3.889E-4	8.101E-4	1.936E-3
ducted	radial velocity	5.495E-5	1.461E-3	1.878E-4
	axial velocity	2.722E-4	6.204E-4	9.117E-4
	wall pressure coefficient	1.530E-2		

Table 2.11:  $L^2$  discrete norm of the difference between semi-analytical (SAOT-5 and SADT-5) and CFD actuator disk (CFDOT-3 and CFDDT-3) velocity and pressure fields.

of the annular wing induces a negative radial velocity in front of the rotor (see  $\zeta/\sigma_{ad} = -1$  profile in the top of Figure 2.6), thus witnessing the opportunity to increase the mass flow swallowed by the device. Moreover for the ducted configuration, Figure 2.7 presents the comparison of the wall pressure coefficients  $C_{p,w} = (p - p_\infty)/\frac{1}{2}\rho U_\infty^2$  as obtained by the two methods. In all cases the agreement between the two reference solutions is excellent. Furthermore, to quantify the differences between the results of the two models, Table 2.11 summarizes the  $L^2$  discrete norm of the error related to the reference cases reported in Figures 2.5, 2.6 and 2.7.

For the sake of completeness, all Figures 2.5–2.7 also report the CFD actuator disk solutions obtained with the coarse mesh, i.e. CFDOT-1 and CFDDT-1. It can be observed that twice doubling the mesh count results in a appreciable reduction of the truncation errors associated with the spatial discretisation of the convective operator in the governing equations. This is most evident from the wall pressure distribution which is largely affected by the local quality of the grid. Because the wall pressure distribution is directly related to the duct thrust coefficient which mainly influences the performance of the device, a mesh density higher than the coarse one (CFDOT-1) would be advisable to properly take into account the effects of the duct. Nevertheless, since the magnitude of the cross sectional velocity profile errors is comfortably small it is speculated that the impact of the numerical errors generated in the duct neighbourhood is negligible in a global sense.

Turning now to the comparison between the semi-analytical and the CFD actuator disk solutions, it can be safely stated that the former, due to its low computational costs, is certainly preferable for design purposes. Indeed the

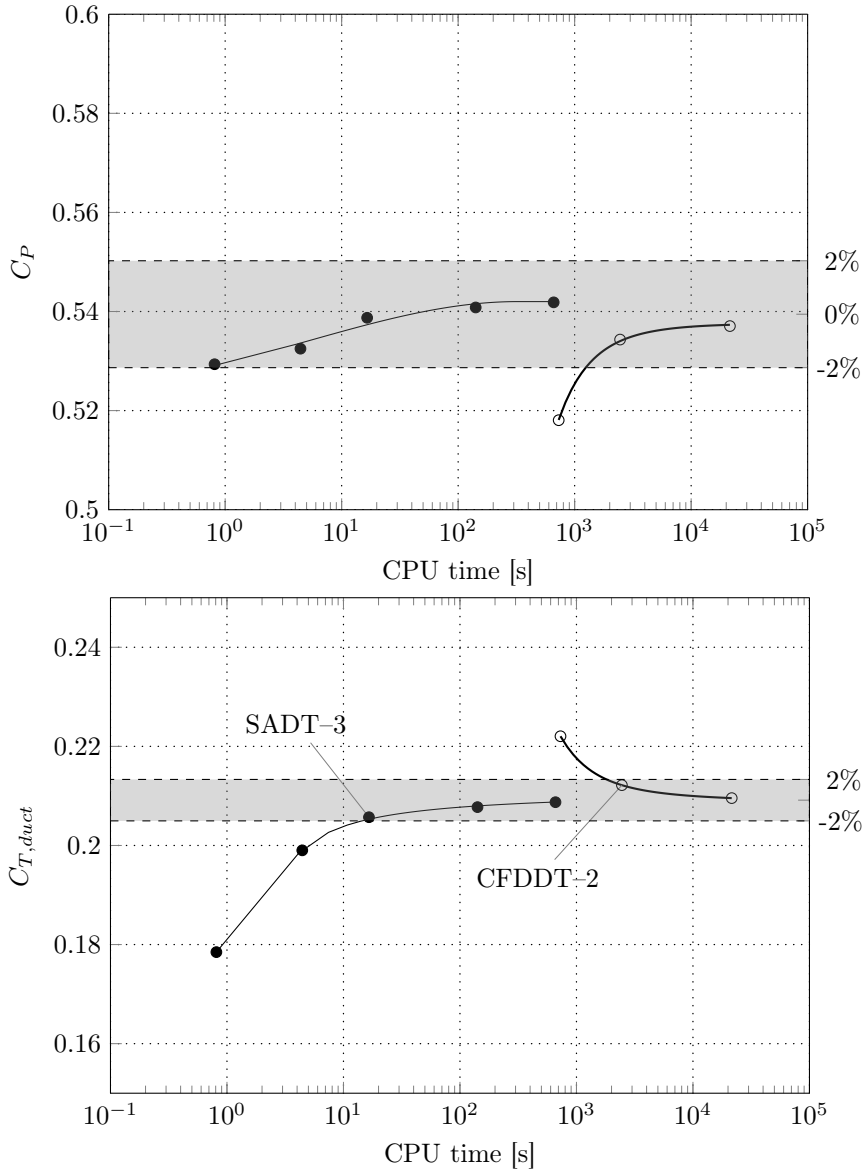


Figure 2.8: Computational cost of the semi-analytical and CFD actuator disk methods.

computational cost of the mesh generation process and of the whole CFD simulation is much larger than that of the semi-analytical method. This is best understood from Figure 2.8 reporting the performance coefficients of all ducted turbine simulations (Tables 2.4 and 2.8) as a function of the run time on an Intel Xeon CPU E5-1620 v2 3.70GHz. All data have also been normalized with a reference value determined as the arithmetic average of SADT-5 and CFDDT-3, and their deviation from this average is shown on the right axis as percentage change. The shaded area denotes a  $\pm 2\%$  uncertainty band. On account of this uncertainty it can be readily inferred that the few seconds run time of SADT-3 are to be compared with tens of minutes of CFDDT-2. This feature is particularly appealing whenever the analysis tool has to be integrated into design systems based on the repeated analysis scheme of hierarchical type, where, depending on the size of the search space, several hundreds of simulations may be required.

---

## FLOW ANALYSIS OF OPEN AND DUCTED PROPELLERS AND COMPARISON WITH CFD

---

### 3.1 Introduction

Ducted propellers consist of a combination of two principal components. The first is an annular wing which can be either symmetric with respect to the rotation axis or asymmetric to accommodate for the wake flow field variations. The second component, i.e. the propeller, differs from a typical open propeller because it has to be designed taking into account the mutual interaction between the duct and the rotor. In general, there are two main type of ducts: the accelerating (also called the Kort nozzle) and the decelerating duct (also referred to as pumpjet). The former, commonly employed on tugs, trawlers, large tankers and supply vessel, develops a propulsive thrust thus increasing the device efficiency and the inflow velocity of the propeller (for this reason it goes by the name of “accelerating duct”). The second, typically used on fast carrier, yields a negative propulsive thrust with a consequent decrease of the efficiency and of the inflow velocity of the propeller (for this reason it goes by the name of “decelerating duct”). However, thanks to the latter feature, the decelerating duct ensures an high pressure at the rotor inlet thus reducing the danger of cavitation. Since the accelerating

duct is the most diffused and studied configuration, in this chapter only this kind of duct is analysed. The early form of ducted propeller was patented by Ludwig Kort in 1924. In this preliminary concept the rotor was installed in a long channel passing through the ship hull. The main drawback of this configuration was the significant increase of the frictional resistance due to the presence of the channel. In the course of the time, the outline of the device was developed by transforming the long channel into the nozzle ring characterizing the present day ducted propellers. Finally, Stipa (1931) and Kort (1934) experimentally proved the increase of the efficiency which can be obtained by ducting the propeller with an accelerating nozzle.

Although, for many years, the design and/or analysis of ducted propellers was mainly carried out on the basis of extensive experimental campaigns (Oosterveld 1970; Van Manen 1957, 1962; Van Manen and Oosterveld 1966; Van Manen and Superina 1959), several theoretical procedures have also been developed since the pioneering work of Horn (1940), and Horn and Amtsberg (1950). Most of these theoretical methods are generally based on the combination of different representations of the velocity field induced by the duct (lumped vortex, thin airfoil theory, panel methods etc.) with the one induced by the rotor (actuator disk, lifting line, lifting surface, boundary element methods, etc.). Some examples are due to: Küchemann and Weber (1953), Tachmindji (1958), Ordway, Sluyter, and Sonnerup (1960), Morgan (1961), Morgan (1962), Dyne (1967), Ryan and Glover (1972), Morgan and Caster (1968), Caracostas (1978), Tsakonas, Jacobs, and Ali (1978), Van Houten (1986), Kerwin, Kinnas, et al. (1987), Kinnas and Coney (1988), Coney (1989), Kinnas and Coney (1992), Baltazar and Falcão de Campos (2009), and Çelik, Güner, and Ekinçi (2010). More recently, computational fluid dynamic (CFD) based methods have also been frequently used to study several aspects of the flow around ducted propellers (Abdel-Maksoud and Heinke 2002; Haimov, Vicario, and Del Corral 2011; Hoekstra 2006; J. Kim, Paterson, and Stern 2003; Sánchez-Caja, Pylkkänen, and Sipilä 2008; T. Wang, Zhou, and X. Zhang 2003).

Although, among the previously mentioned methods, the linearised actuator disk undoubtedly represents the oldest and easiest model used to analyse the flow around a propeller (Froude 1889; Rankine 1865), it is still widely employed both in its linear (Conway 1995) and nonlinear formulation (Conway 1998; Greenberg and Powers 1970; Wu 1962). Remarkable examples of ducted propellers modelled through an actuator disk are due to: Dickmann and Weissinger (1955), Chaplin (1964), Van Gunsteren (1973), Gibson and Lewis (1973) and Falcão de Campos (1983). More recently, the actuator disk method has also been frequently adopted in combination with

modern CFD techniques (referred to as "CFD actuator disk") as a way to alleviate the computational costs related to the simulation of geometrically resolved propellers. In fact, the complexity of the mesh generation process as well as the requirements associated with an appropriate resolution of the boundary layers can be disregarded employing this simplified model which is recognized to yield satisfactorily accurate results.

As a matter of fact this approach has been extensively applied to the study of propeller/hull and propeller/hull/rudder interactions problems.

Schetz and Favin (1977, 1979) attempted to model the propeller by means of an axisymmetric distribution of body-forces one-way coupled to the incompressible Navier-Stokes equations cast in a stream-function formulation.

Stern et al. (1988a) solved the partially parabolic RANS equations for an axisymmetric propeller/hull interaction problem representing the propeller through a set of radial body-forces distributed over a disk of finite thickness. More in detail, Stern et al. (1988a) coupled in an interactive and iterative manner the partially-parabolic method of Chen and Patel (1985) with the vortex-lattice lifting-surface model developed by Kerwin and C. S. Lee (1978). The former method was used to simulate the ship-stern viscous flow, while the latter was employed to calculate the radial distribution of the blade circulation along the propeller span. In Stern et al. (1988b) the method of Stern et al. (1988a) was applied to a propeller-shaft configuration and validated comparing computational results with the many available experimental data of M. H. Wang (1985). Further validation of the method of Stern et al. (1988a) has been provided by Stern, Toda, and H. T. Kim (1991) and Stern, H. T. Kim, D. H. Zhang, et al. (1994) through a detailed comparison with experimental data for the well-known configuration of the Iowa axisymmetric body and the Series 60  $C_B = 0.6$  ship model, respectively. The approach of Stern et al. (1988a) has also been used by Piquet, Queutey, and Visonneau (1987), Watanabe, Masuko, and Shiorose (1994), Weems et al. (1994), and D. H. Zhang et al. (1991) and Badoe, Phillips, and Turnock (2012) to study several aspects of the propeller/hull flow problem. To further extend the work of Stern et al. (1988a) to off-design conditions, Chen and S. K. Lee (2003a,b) coupled the chimera RANS method of Chen, T. Liu, and Huang (2002) with the MPUF-3A propeller analysis program of H. Lee and Kinnas (2001) and applied it to the simulation of propeller-ship interaction problems. Calculations were performed and validated for the Series 60  $C_B = 0.6$  ship hull equipped with the MAU propeller (Toda et al. 1900) under various operating conditions. Moreover the method of Chen and S. K. Lee (2003a,b) has been further applied to a cavitating propeller

(S. K. Lee and Chen 2005).

Kerwin, Keenan, et al. (1994) developed a propeller design method in which the flow field is decomposed into an axisymmetric and a non-axisymmetric part. The axisymmetric flow field was obtained with a Reynolds-averaged-Navier-Stokes code, while the non-axisymmetric part was obtained with a vortex-lattice lifting-surface code. In order to carry out the coupling of the two solvers, the propeller was represented by a set of axial and tangential body forces distributed over the swept volume of the blade rows.

Kawamura, Miyata, and Mashimo (1997) simulated the flow around five tankers introducing the Nakatake (1989) simplified actuator disk propeller model into the finite-volume method WISDAM-V developed by Miyata, Zhu, and Watanabe (1992). In the above procedure, the interaction between the two flow models is handled through a time-marching procedure which should converge towards the steady self-propelling condition.

In order to predict the non-axisymmetric effective wake of a propeller, J. K. Choi and Kinnas (2001) coupled a fully three-dimensional finite volume Euler solver with a lifting-surface vortex lattice method (Kinnas, Griffin, et al. 1998) for the analysis of unsteady cavitating propeller flows. Once again the propeller is represented by an appropriate distribution of body forces over the disk propeller area and the results are validated against both analytical solutions and experimental data.

Sadat-Hosseini et al. (2011) used a CFD actuator disk model to predict broaching, surf-riding, and periodic motion for the ONR Tumblehome model. The above work also includes captive and free model test validation studies.

J. E. Choi et al. (2010) examined the performance of various types of commercial ships analysing the resistance and propulsion characteristics as a function of the advance coefficient. An asymmetric body-force propeller is applied where the effect of a finite number of blades is neglected. The incoming flow velocity on the propeller plane obtained from the commercial RANS solver ANSYS Fluent is used as input data for the potential-flow solver MPUF-3A (Kinnas, Griffin, et al. 1998). After getting thrust and torque distribution acting on an actuator disk and induced velocities from the potential solver, the thrust and torque are substituted for the body forces which are the source terms of RANS. These iterative processes are performed until the thrust and torque converge. User-defined function was used to implement the asymmetric body-force propeller model to the Fluent code.

Greve et al. (2012) also reported the development and application of a

coupling procedure based on the interaction between a RANS method and a boundary element method. The procedure was applied to the analysis of the unsteady behaviour of the propeller thrust and torque induced by large amplitude ship motions. To this aim, the time-accurate propeller loads computed by the inviscid method are directly applied to the RANS solver without any circumferential or radial averaging.

Recently, also the blade element momentum theory (BEM) has been adopted in CFD actuator disk methods. Phillips, Turnock, and Furlong (2009) developed a coupled BEM-RANS procedure to determine the manoeuvring coefficients of a self-propelled ship travelling straight ahead, at a drift angle and for differing rudder angles. More in detail, the BEM is used to model the effects of the propeller, without tackling its geometric complexity, with a set of forces which are then inserted in the RANS domain which may include the ship hull and the rudder. An averaged RANS-calculated nominal wake fraction evaluated at prescribed radial positions serves as input to the BEM. Then, the calculated thrust and torque values obtained from the BEM are transformed into radius-averaged momentum source terms distributed over a disk of finite thickness at the propeller position inside the RANS domain. With these body forces, the steady RANS simulation is iterated to convergence. In order to predict the free turning manoeuvre of a tanker-like ship, Broglia et al. (2013) coupled different propeller actuator disk models with an in-house uRANS code. More in detail, two models were considered: a modified Hough and Ordway (1964) approach and a model based on the blade element momentum theory.

The CFD actuator disk methods are also widely used for the analysis of the flow around ducted propellers. In addition to the aforementioned paper of Kerwin, Keenan, et al. (1994), Yang, Hartwich, and Sundaram (1991) and Dai, Gorski, and Haussling (1991) applied the approach of Stern et al. (1988a) with a prescribed radial distribution of the load to the analysis/design of ducted propellers interacting with the hull and the shaft. In the past several authors carried out experimental investigations about ducted propellers (see for instance Hughes, Kinnas, and Kerwin (1992), Luttmmer and Jassen (1982), and Oosterveld (1970)) and many useful data on the performance characteristics of this type of propulsion unit are available. However, the experiments have often been performed at model scale and consequently the data may suffer from scale effects. In order to investigate the scale effects, which often significantly affect the duct performance, Hoekstra (2006) proposed a RANS-based computational model. In this approach the duct is kept in its true shape, while the propeller is represented as an actuator disk of finite thickness and with a prescribed distribution of

axial and tangential forces. Moreover, the author analysed the effects on the duct performance of the swirl in the propeller slipstream, of the hub presence and shape, of the radial loading distribution and of the tip gap. Finally, the computed velocity fields are validated against the LDV measurements reported in Falcão de Campos (1983).

Sileo and Steen (2009) conducted a numerical investigation of the interference between a stern tunnel thruster and two ducted main propellers. In fact, this interaction phenomenon is reckoned to be responsible for a considerable performance decay of the ducted propeller system during manoeuvring operations, in terms of drop of turning moment with increasing loading on the main propellers. The study is carried out with the commercial solver ANSYS Fluent which is used to study the viscous turbulent flow around the ship hull. The two propellers in the ducts as well as the one in the tunnel are represented by an actuator disk approximation (the so called “fan boundary condition”) with appropriate distributions of thrust and tangential velocity over the fan disk. The latter are obtained from the distribution of the blade circulation calculated by potential methods for an open water propeller close to bollard condition. A single radial thrust distribution is used for all the considered test cases, while the actual values are scaled to achieve in the calculations the same total thrust of the corresponding model tests.

The extensive literature review presented above proves that the actuator disk is still considered a successful and widely used model to simulate open and ducted propeller wakes. Therefore, in order to bring out the beneficial effects of the duct on the efficiency, in this chapter the semi-analytical actuator disk method (extensively described in Chapter 1) is applied to compare the performance of ducted and open propellers. Insight about the matching conditions of the ducted configuration are provided analysing the local flow features at the duct inlet. Moreover, with regards to swirled flows, the results of the semi-analytical actuator disk and of the CFD actuator disk model are compared in §3.3. To this aim the so-called “fan boundary condition” of the commercial code ANSYS Fluent is adopted with a prescribed pressure jump and tangential velocity radial profiles at the disk plane.

## 3.2 The duct effect: linear and nonlinear analysis

As stated in the introduction, ducted propellers are widely diffused devices which are mainly employed to improve the propulsive efficiency of heavily loaded rotors. Significant and meaningful insights into the possibility to

obtain an increase of the efficiency can be gained by the one dimensional linearised actuator disk theory with no wake rotation (see for example Von Mises (1945), Küchemann and Weber (1953) and Oosterveld (1970)). First of all, the following typical definitions are used for the thrust and power coefficients:

$$C_T = \frac{T}{\frac{1}{2}\rho U_\infty^2 \pi \sigma_{ad}^2}, \quad C_P = \frac{P}{\frac{1}{2}\rho U_\infty^3 \pi \sigma_{ad}^2},$$

where  $T$  and  $P$  are the magnitude of the thrust and the power experienced by the device. For the ducted propeller the overall thrust can be divided into the duct and the rotor thrust  $\mathbf{T} = \mathbf{T}_{rot} + \mathbf{T}_{duct}$ , thus obtaining  $C_T = C_{T,rot} + C_{T,duct}$ . With the help of the classical hypothesis of the one dimensional linearised actuator disk theory, the magnitude of the work done by the propeller can be expressed as

$$W = \mathcal{H} = \frac{\Delta p_{rot}}{\rho} = \frac{1}{2}(u_e^2 - U_\infty^2). \quad (3.1)$$

In the above equation  $\Delta p_{rot}$  is the pressure difference across the rotor and  $u_e$  is the wake velocity at infinity downstream. Making use of equation (3.1), the power absorbed by the propeller reads

$$P = \dot{m}W = \rho u_{rot} A_{rot} \frac{\Delta p_{rot}}{\rho} = u_{rot} T_{rot}, \quad (3.2)$$

where  $A_{rot} = \pi \sigma_{ad}^2$ ,  $u_{rot}$  is the axial velocity at the rotor plane and  $T_{rot} = \Delta p_{rot} A_{rot}$  is the magnitude of the rotor thrust. From the axial momentum equation, the expression for the magnitude of the overall thrust can be obtained

$$T = \dot{m}(u_e - U_\infty) = \rho u_{rot} A_{rot} U_\infty (\hat{u}_e - 1), \quad (3.3)$$

where  $\hat{u}_e = u_e/U_\infty$  is the dimensionless wake velocity downstream at infinity. Using equations (3.1), (3.2) and (3.3), the performance coefficients of the device can be cast in the following form:

$$C_{T,rot} = \frac{T_{rot}}{\frac{1}{2}\rho U_\infty^2 A_{rot}} = \frac{2\mathcal{H}}{U_\infty^2} = \hat{u}_e^2 - 1, \quad (3.4)$$

$$C_T = \frac{T}{\frac{1}{2}\rho U_\infty^2 A_{rot}} = 2\hat{u}_{rot}(\hat{u}_e - 1), \quad (3.5)$$

$$C_P = \frac{P}{\frac{1}{2}\rho U_\infty^3 A_{rot}} = \hat{u}_{rot} C_{T,rot} = \frac{C_T}{2}(\hat{u}_e + 1). \quad (3.6)$$

chord/rotor diameter	$chord/D$	0.5
angle between the chord and the axial direction duct D1	$\alpha$	6.0°
angle between the chord and the axial direction duct D2	$\alpha$	12.7°
angle between the chord and the axial direction duct D3	$\alpha$	20.0°
tip gap/rotor diameter	$\epsilon/D$	0.75%
advance coefficient	$J$	0.5

Table 3.1: Propeller ducted with a NACA 4415 profile: geometry.

Finally, the propulsive efficiency is

$$\eta = \frac{C_T}{C_P} = \frac{2}{\hat{u}_e + 1} = \frac{2}{1 + \sqrt{1 + C_{T,rot}}}. \quad (3.7)$$

The aim of the duct is to increase the efficiency for a prescribed propulsive thrust required by the carrier. Therefore, from equation (3.7), it is clear that this result is achieved decreasing the rotor thrust, while the missing axial force must be delivered by the duct. In fact, in order to keep constant the overall propulsive thrust of the device (given by  $\mathbf{T} = \mathbf{T}_{rot} + \mathbf{T}_{duct}$ ), the duct must be designed in such a way that  $\mathbf{T}_{duct}$  and  $\mathbf{T}_{rot}$  have the same direction. Conversely, if the direction of  $\mathbf{T}_{duct}$  is opposite to that of  $\mathbf{T}_{rot}$ , then the latter has to be increased with a consequent drop in the efficiency. At the end, it is noteworthy that the duct improves the efficiency by reducing the rotor load, but increasing the mass flow rate swallowed by the propeller. In fact from equation (3.4) a decrease in the rotor thrust implies a decrease in the wake velocity downstream at infinity which, the total thrust in equation (3.3) being constant, leads to an increase in the mass flow rate.

Turning now to the more accurate and realistic nonlinear actuator disk theory described in Chapter 1, Figure 3.1 shows the comparison between the propulsive efficiency of the ducted propellers described in Table 3.1 and the open propeller at different values of  $C_T$ . In particular, all the calculations are carried out with a parabolic load radial distribution (see equation (1.68)) and with an advance coefficient  $J = 0.5$ . Figure 3.2 presents the thrust coefficient of the ducts of Table 3.1 at different values of  $C_T$ ; as customary the  $C_{T,duct}$  coefficient is considered positive (negative) if  $\mathbf{T}_{duct}$  and  $\mathbf{T}_{rot}$  have the same (opposite) direction. As showed in Figure 3.1, the propellers equipped with the duct D1 is characterised by an higher efficiency, regardless of the  $C_T$  value. This is due to the positiveness of  $C_{T,duct}$  for all  $C_T$  (see Figure 3.2). Otherwise ducts D2 and D3, for small  $C_T$  values, exert an axial force with opposite direction in comparison to the rotor thrust thus obtaining,

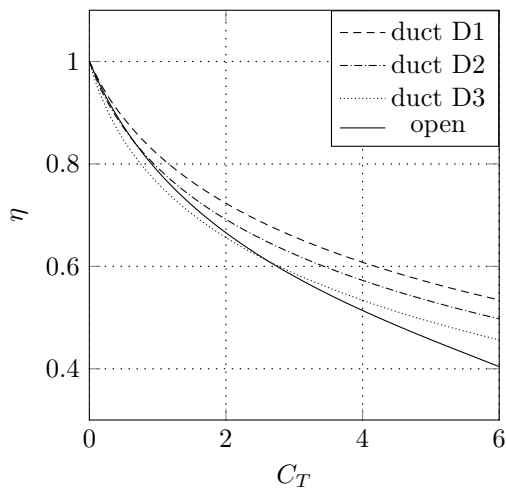


Figure 3.1: Efficiency comparison between open and ducted propellers.

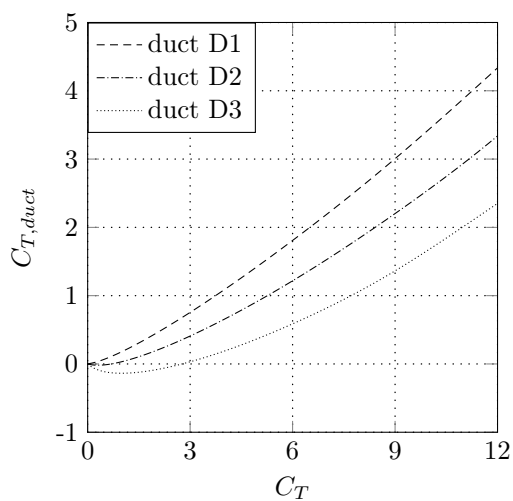


Figure 3.2: Duct thrust coefficient for ducted propellers.

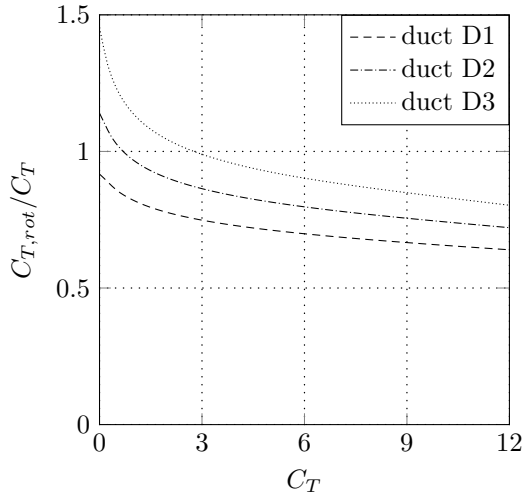


Figure 3.3: Rotor thrust contribution to the overall propulsive thrust for ducted propellers.

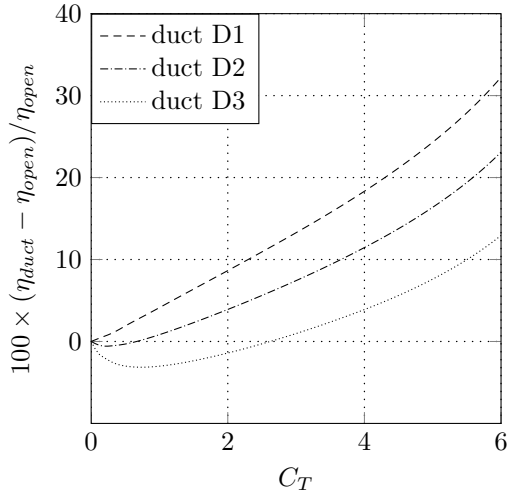


Figure 3.4: Percentage variation in efficiency for ducted and open propellers.

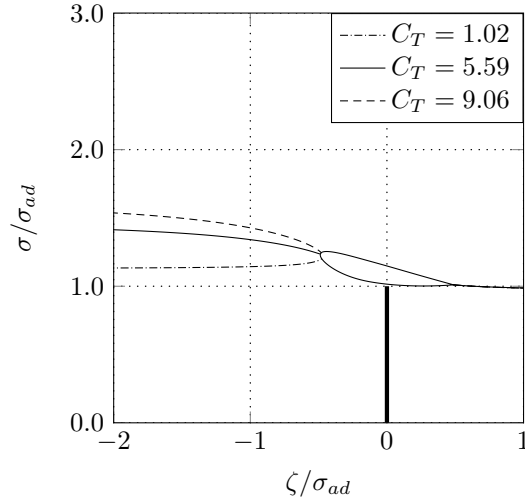


Figure 3.5: Streamlines for duct D2 at different values of the thrust coefficient  $C_T$ .

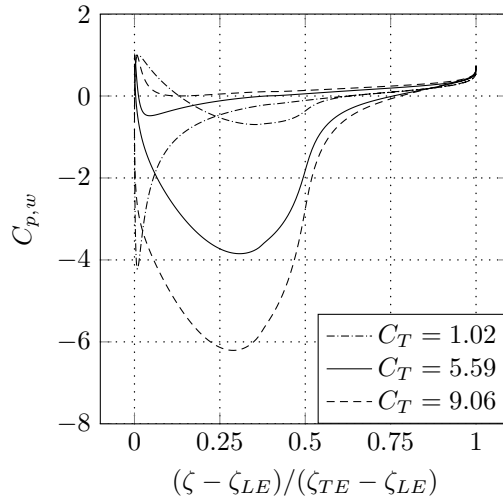


Figure 3.6: Wall pressure coefficient for duct D2 at different values of the thrust coefficient  $C_T$ .

in accordance with the linearised theory, a lower efficiency compared with that of the open propeller. Furthermore, the relative contribution of the duct to the propulsive thrust becomes larger and larger as the overall thrust increases (see Figure 3.3). Consequently, compared with the open propeller, the efficiency increases as well (see Figure 3.4).

Another very important aspect that deserves to be investigated is the appropriate matching between the rotor and the duct at different operating conditions. In particular, as already stated, the duct shape and its arrangement have to be devised as to increase the efficiency. From this point of view, it is essential to avoid flow separation on both sides (inner and outer) of the duct which is likely to occur for heavily loaded nozzles at off-design conditions. In more detail, if the rotor load and consequently the mass flow swallowed by the propeller are much lower (larger) than the design one, then the front stagnation point is located on the internal (external) surface of the duct thus promoting flow separation on the external (internal) surface. The displacement of the stagnation point in the leading edge region as the load is changed is clearly visible in Figure 3.5 reporting the stagnation streamlines for duct D2 at different  $C_T$  values. Figure 3.6 shows instead the wall pressure coefficient  $C_{p,w} = (p - p_\infty) / \frac{1}{2} \rho U_\infty^2$  distribution for duct D2 at different values of  $C_T$ . As anticipated, for high and low values of the rotor load the  $C_{p,w}$  profiles point out the presence of undesired velocity peaks that could lead to flow separation. Always with reference to duct D2, the value of  $C_T$  for which the leading edge is unloaded (optimum incidence) is  $C_T \approx 5.59$ .

On the other side, from a design point of view, if the target  $C_T$  value is significantly higher or lower than  $C_T = 5.59$ , then the geometry of the duct should be changed in order to prevent flow separation. One way to overcome this problem is to modify the angle  $\alpha$  between the profile chord and the  $\zeta$  axis for a prescribed shape of the profile itself (see Table 3.1). For  $C_T < 5.59$  a duct with a lower value of the  $\alpha$  angle should be employed and vice versa. In fact, for ducts D1 and D3 the optimum incidences are those associated to the following  $C_T$  values:  $C_T \approx 1.59 < 5.59$  and  $C_T \approx 8.71 > 5.59$ .

### 3.3 Comparison between the semi-analytical and the CFD actuator disk for swirled flows

As discussed in the introduction, the CFD actuator disk is a widely employed analysis method which provides the solution of the Navier-Stokes or Euler equations in a domain comprising a propeller which is represented through

a body force distribution over a disk area. From a computational point of view these distributions are obtained pursuing several approaches like an iterative and interactive coupling with lifting-surface, boundary element or blade element methods. However, as recommended in Stern et al. (1988a), many researchers often applied a prescribed body force distribution over the disk area (see for instance Hoekstra (2006), Piquet, Queutey, and Visonneau (1987), Yang, Hartwich, and Sundaram (1991), Dai, Gorski, and Haussling (1991), but this list should not be regarded as exhaustive). In this section the so-called “fan boundary condition” implemented in the commercial CFD code ANSYS Fluent has been used to simulate the presence of the rotor. To this aim a pre-defined radial distribution of the pressure jump across the disk has been prescribed. Moreover, only for three dimensional computations, the “fan boundary condition” also allows to specify a radial profile for the tangential velocity just behind the disk. In the following section, the results obtained by modelling the rotor through the “fan boundary condition” are compared with those of the semi-analytical procedure with swirl described in Chapter 1. To this end an in-depth analysis of the error generated by the two methods is presented in §3.3.1 and §3.3.2. Finally, in §3.3.3 a detailed comparison between the results of the two procedures is carried out both for the open and the ducted configuration.

### 3.3.1 The semi-analytical actuator disk method with swirl: error analysis

As detailed in Chapter 1, the evaluation of the Stokes stream function  $\Psi$  via the exact solution of the governing equation (1.33) is prevented due to the implicitness of this equation. In particular, the slipstream location  $\sigma_s$ , the density strength  $\gamma_{ad}$  and the duct induced stream function  $\Psi_d$  all depend upon  $\Psi$ . The solution can be made explicit through the semi-analytical procedure developed and validated in Chapter 1. This procedure introduces three (four for ducted propellers) numerical parameters, i.e.  $n_z$ ,  $n_{zs}$ ,  $n_{rs}$  (and  $M_p$ ) whose effects onto the solution is investigated in the following error analysis. More in detail, for the sake of conciseness, the numerical parameters are simultaneously made to increase in a five-levels range as shown in Tables 3.3 and 3.4 for the open and ducted configuration, respectively. Assuming case SAOP-5 (SADP-5) of Table 3.3 (3.4) as reference, the open (ducted with the NACA 4415 profile of Table 3.2) propeller relative errors of the performance coefficients and the  $L^2$  discrete norm of the errors of the axial velocity at different axial stations are computed and listed in Table 3.5 (3.6 and 3.7).

chord/rotor diameter	$chord/D$	0.5
angle of attack	$\alpha$	12.7°
tip gap/rotor diameter	$\epsilon/D$	1.539%
leading edge radial position/chord	$\sigma_{LE}/d$	1.230
leading edge axial position/chord	$\zeta_{LE}/d$	-0.488

Table 3.2: Propeller ducted with a NACA 4415 profile: main geometrical parameters.

$\#case$	$n_z$	$n_{zs}$	$n_{rs}$	$\hat{b} = \sigma_{ad}^2 a_1 / U_\infty \Psi_{\sigma_{ad}}$	J
SAOP-1	101	51	51	10.0	0.5
SAOP-2	201	101	101	10.0	0.5
SAOP-3	301	151	151	10.0	0.5
SAOP-4	401	201	201	10.0	0.5
SAOP-5	501	251	251	10.0	0.5

Table 3.3: Open rotor configuration: numerical parameters and operating conditions.

$\#case$	$n_z$	$n_{zs}$	$n_{rs}$	$M_p$	$\hat{b} = \sigma_{ad}^2 a_1 / U_\infty \Psi_{\sigma_{ad}}$	J
SADP-1	101	51	51	200	15.0	0.5
SADP-2	201	101	101	400	15.0	0.5
SADP-3	301	151	151	600	15.0	0.5
SADP-4	401	201	201	800	15.0	0.5
SADP-5	501	251	251	1000	15.0	0.5

Table 3.4: Propeller ducted with a NACA 4415 profile: numerical parameters and operating conditions.

3.3 Comparison between the semi-analytical and the CFD actuator disk method

<i>#case</i>	Performance coefficients relative error			Axial velocity $L^2$ discrete norm of the error		
	$C_T$	$C_P$	$\eta$	$u _{\zeta=-1}$	$u _{\zeta=0}$	$u _{\zeta=1}$
SAOP-1	2.259E-3	3.306E-3	1.043E-3	4.850E-4	3.858E-3	1.563E-3
SAOP-2	2.872E-4	3.135E-4	2.628E-5	5.123E-5	5.722E-4	1.530E-4
SAOP-3	6.557E-5	4.198E-5	2.359E-5	7.023E-6	1.478E-4	2.347E-5
SAOP-4	6.690E-6	1.110E-5	1.780E-5	1.063E-6	4.067E-5	1.008E-5
SAOP-5	0	0	0	0	0	0

Table 3.5: Open propeller: error analysis.

<i>#case</i>	Performance coefficients relative error				
	$C_T$	$C_{T,rot}$	$C_{T,duct}$	$C_P$	$\eta$
SADP-1	1.561E-2	8.937E-3	4.330E-2	1.936E-2	3.831E-3
SADP-2	4.772E-3	2.692E-3	1.341E-2	5.788E-3	1.021E-3
SADP-3	1.857E-3	1.067E-3	5.138E-3	2.275E-3	4.190E-4
SADP-4	7.101E-4	4.098E-4	1.957E-3	8.670E-4	1.570E-4
SADP-5	0	0	0	0	0

Table 3.6: Propeller ducted with a NACA 4415: performance coefficients error analysis.

<i>#case</i>	Axial velocity $L^2$ discrete norm of the error		
	$u _{\zeta=-1}$	$u _{\zeta=0}$	$u _{\zeta=1}$
SADP-1	7.229E-3	1.885E-2	1.616E-2
SADP-2	2.148E-3	5.512E-3	4.738E-3
SADP-3	9.668E-4	2.172E-3	1.849E-3
SADP-4	3.237E-4	8.402E-4	7.209E-4
SADP-5	0	0	0

Table 3.7: Propeller ducted with a NACA 4415: axial velocity error analysis.

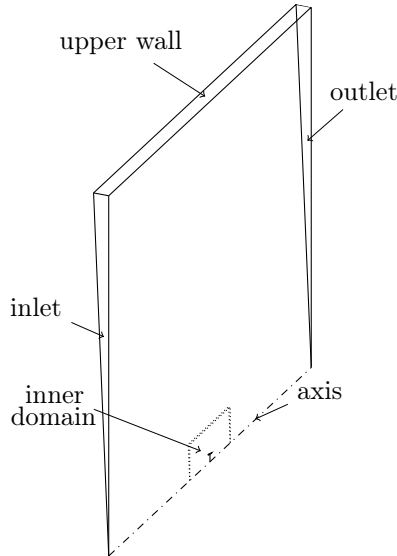


Figure 3.7: Computational domain.

### 3.3.2 The 3D CFD actuator disk method with swirl: error analysis

The CFD code ANSYS Fluent is a general purpose and widely spread analysis software which can handle a variety of complex problems. Unfortunately, in its actual form the software is unable to handle an actuator disk flow with swirl in an axisymmetric formulation through the already mentioned “fan boundary condition”. In other words, the “fan boundary condition” with swirl, prescribing both a pressure jump and a tangential velocity profiles at the disk, is operational only for a three-dimensional configuration. For this reason a 3D computational domain is generated rotating the meridian plane 2 degrees around the propeller axis (see Figure 3.7). Besides the two lateral surfaces, the domain is bounded by an inlet and an outlet boundary placed at  $25\sigma_{ad}$  from the actuator disk plane, and by an upper boundary located at  $50\sigma_{ad}$  from the  $\zeta$  axis. At the inlet a uniform axial velocity  $U_\infty$  is imposed, whereas the outlet is treated as a no constant pressure

### 3.3 Comparison between the semi-analytical and the CFD actuator disk method

# case	Open		# case	Ducted	
	# cells inner domain	# cells full-size domain		# cells inner domain	# cells full-size domain
CFDOP-1	20250	70200	CFDDP-1	59044	145314
CFDOP-2	78500	204288	CFDDP-2	218688	415188
CFDOP-3	308000	580293	CFDDP-3	855768	1294159

Table 3.8: Characteristics of the mesh employed in the CFD grid dependence analysis for open propeller.

#case	$u _{\zeta=-1}$	$u _{\zeta=1}$	$v _{\zeta=-1}$	$v _{\zeta=1}$	$w _{\zeta=1}$
CFDOP-1	1.931E-4	1.657E-2	1.667E-4	5.251E-4	3.106E-1
CFDOP-2	1.263E-4	6.101E-3	9.669E-5	2.067E-4	1.155E-3
CFDOP-3	0	0	0	0	0

Table 3.9: Open propeller:  $L^2$  discrete norm of the error.

#case	$u _{\zeta=-1}$	$u _{\zeta=1}$	$v _{\zeta=-1}$	$v _{\zeta=1}$	$w _{\zeta=1}$
CFDDP-1	2.928E-3	1.328E-2	1.711E-3	7.412E-4	6.385E-3
CFDDP-2	7.965E-4	4.003E-3	4.755E-4	2.064E-4	1.666E-3
CFDDP-3	0	0	0	0	0

Table 3.10: Propeller ducted with a NACA 4415:  $L^2$  discrete norm of the error.

		$\zeta = -1.0$	$\zeta = 1.0$
open	radial velocity	1.353E-4	1.942E-4
	axial velocity	5.455E-4	4.319E-3
	tangential velocity	–	6.711E-4
ducted	radial velocity	5.530E-4	2.112E-3
	axial velocity	5.547E-4	1.071E-2
	tangential velocity	–	9.181E-3
wall pressure coefficient		1.752E-2	

Table 3.11: Comparison between semi-analytical (SAOP-5 and SADP-5) and CFD actuator disk (CFDOP-3 and CFDDP-3):  $L^2$  discrete norm of the error.

outflow boundary. An inviscid wall treatment is used for the upper and the duct surfaces, while the two lateral faces are considered as rotationally periodic. Finally, the pressure jump and the tangential velocity radial profiles, obtained for the reference cases SAOP-5 and SADP-5, are prescribed at the actuator disk plane through the “fan boundary condition”. The error analysis is performed discretizing the domain through a body-fitted curvilinear grid system, whose density is increased in the region inside which the flow interaction takes place. This region, termed “inner domain”, is  $10\sigma_{ad} \times 5\sigma_{ad}$  large (see Figure 3.7). The effects of the extension of the inner and outer domains were also investigated through a separate study whose results are not reported for the sake of brevity. The computations are carried out with a pressure correction method for the time integration, and a second order scheme for the spatial discretization. Table 3.8 shows the number of elements of the meshes employed in the grid dependence analysis, both for the open and ducted configurations. Finally, the  $L^2$  discrete norm of the error in the axial and radial velocities are listed in Tables 3.9 and 3.10.

### 3.3.3 Semi-analytical and CFD actuator disk methods: comparison of the results

In order to prove the accordance of the semi-analytical and CFD actuator disk methods, the results of the simulations termed as “reference case”, i.e. SAOP-5, SADP-5, CFDOP-3 and CFDDP-3 which are obtained using the densest combination of the selected numerical parameters, are compared

3.3 Comparison between the semi-analytical and the CFD actuator disk method

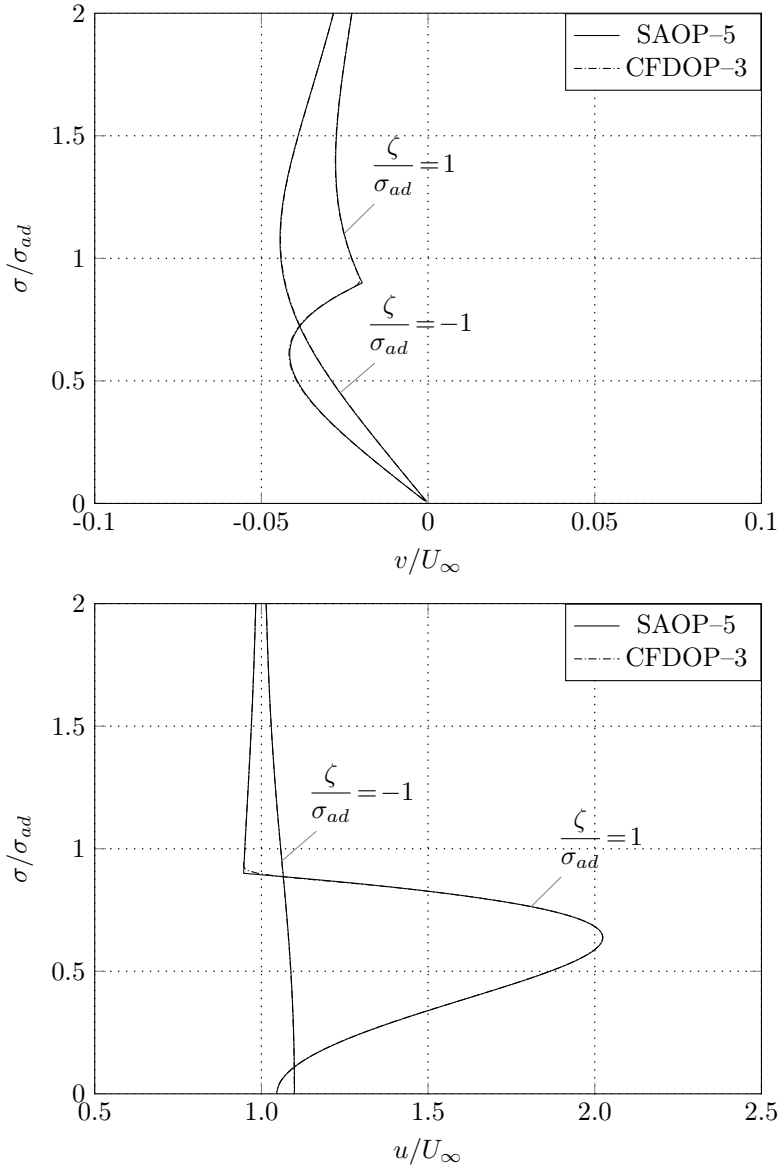


Figure 3.8: Open propeller: comparison of the radial (top) and axial (bottom) velocity profiles obtained through the semi-analytical (SAOP-5) and CFD (CFDOP-3) actuator disk methods.

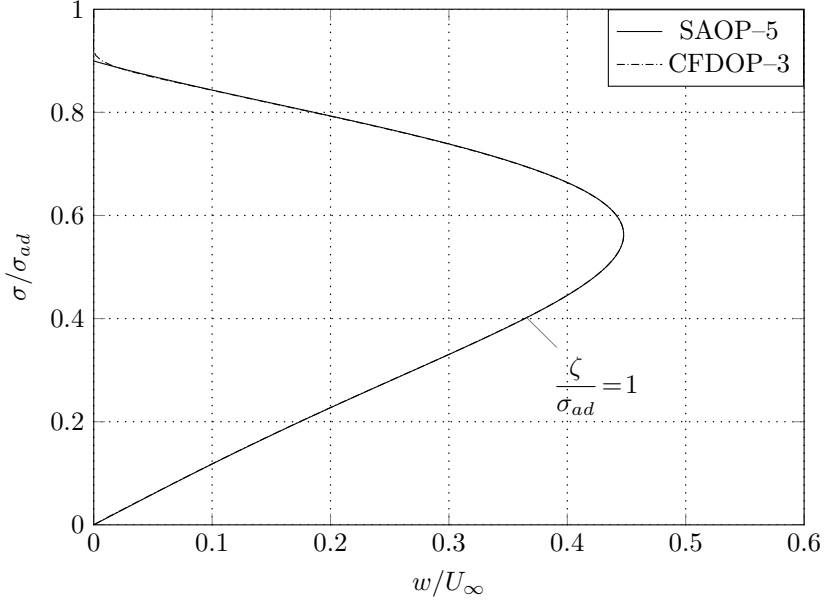


Figure 3.9: Open propeller: comparison of the tangential velocity profiles obtained through the semi-analytical (SAOP-5) and CFD (CFDOP-3) actuator disk methods.

one another, both for the open and ducted configuration. The comparison allows to test how well the fan boundary condition works and to validate the semi-analytical actuator disk method at all points of the domain and not only at downstream infinity as previously reported in Chapter 1. Regarding the open configuration, the radial profiles of the radial, axial and tangential velocities at different axial stations obtained with the semi-analytical and CFD actuator disk models are presented in Figures 3.8, 3.9. Likewise, for the ducted configuration, the radial profiles of the radial, axial and tangential velocities at different axial stations are showed in Figures 3.10 and 3.11. Furthermore, the comparison of the wall pressure coefficients  $C_{p,w} = (p - p_\infty)/\frac{1}{2}\rho U_\infty^2$  is also shown in Figure 3.11. Although, the agreement seems to be very good in all cases, the differences between the results of the two models is also quantified in Table 3.11 which listed the  $L^2$  discrete norm of the error related to the cases reported in Figures 3.8, 3.9, 3.10 and 3.11.

3.3 Comparison between the semi-analytical and the CFD actuator disk method

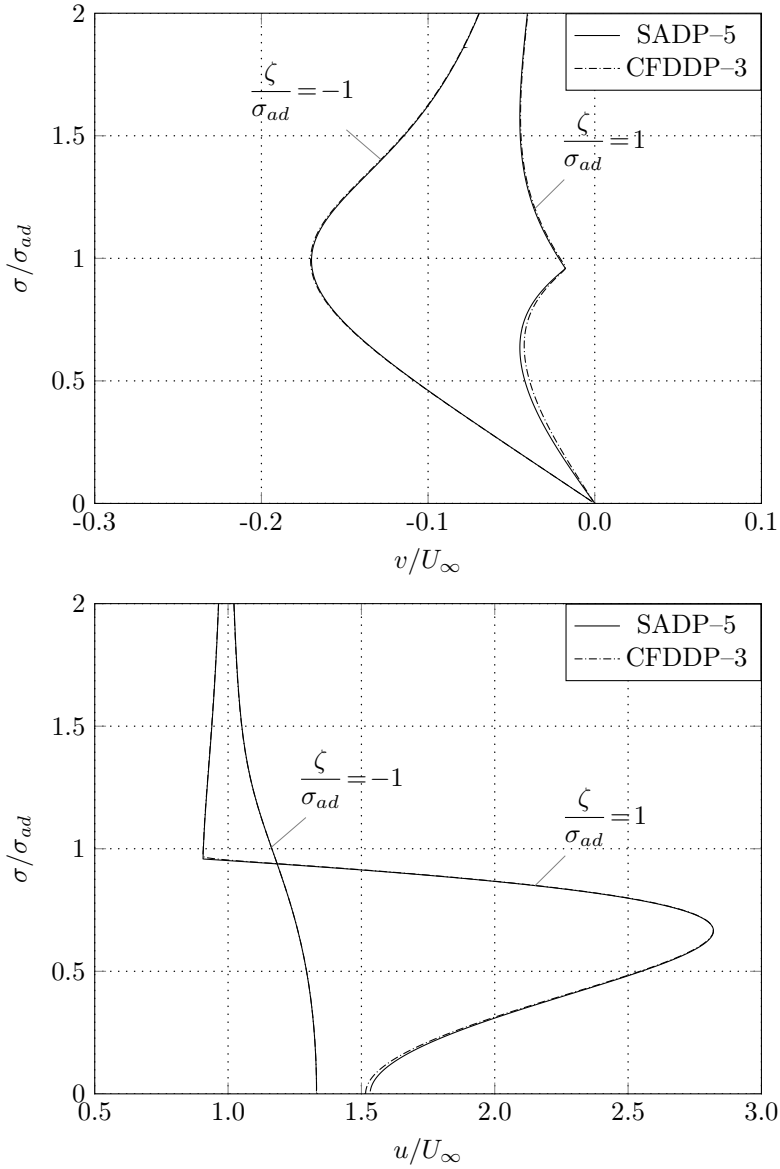


Figure 3.10: Ducted propeller: comparison of the radial (top) and axial (bottom) velocity profiles obtained through the semi-analytical (SADP-5) and CFD (CFDDP-3) actuator disk methods.

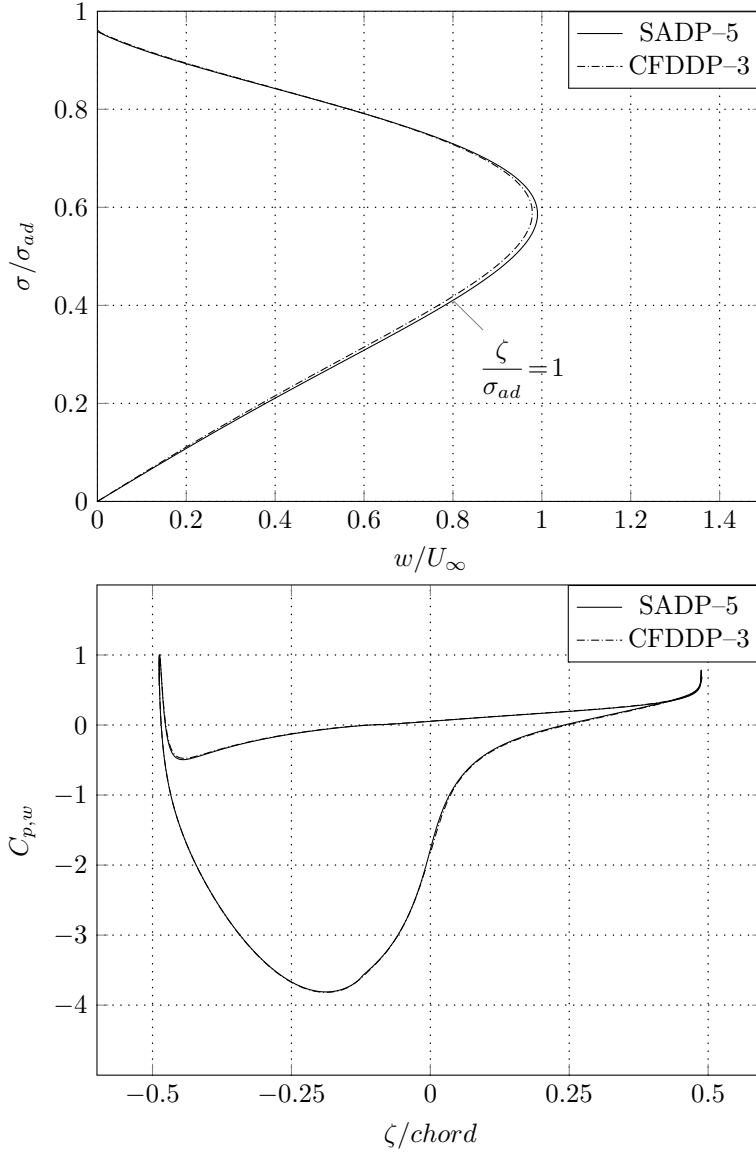


Figure 3.11: Ducted propeller: comparison of the tangential velocity (top) and of the wall pressure coefficient (bottom) distributions obtained through the semi-analytical (SADP-5) and CFD (CFDDP-3) actuator disk methods.

---

**EXACT SOLUTION OF THE FLOW OVER A  
NON-UNIFORM HEAVILY LOADED ACTUATOR  
DISK WITH FINITE HUB**

---

## 4.1 Introduction

In most of the flow analysis methods for open rotors the presence of the hub is often overlooked or taken into account in an approximate manner. As a matter of fact, the availability of a numerical model which could properly handle a prescribed hub geometry is mandatory for all those applications characterised by a appreciable value of the hub/propeller radii ratio, as frequently encountered in the marine propeller field. For instance, the hub of a controllable pitch propeller (CPP) generally has a larger radius than that of a fixed pitch propeller (FPP). This is due to the necessity to accommodate the blade actuation mechanism and to withstand the propulsive force supplied to and transmitted from the propeller blades to the shaft. Typically, the hub/propeller radii ratio for a CCP is in the range 0.24–0.32, but for some applications this may reach values as high as 0.4 or even 0.5 (Carlton 2007). In contrast, hub/propeller radii ratios for a FPP are generally smaller, i.e. within the range 0.16 to 0.25. Moreover, the hub radii of azimuthing and podded propulsors are also very large in order to house the

drive mechanisms or the electric motor. Finally, it is always very important to take into account the hub presence in all those applications in which the hub is part of the stern (submarine propellers, torpedoes, autonomous underwater vehicles and so on).

Not disregarding the three dimensional and geometry resolved computational fluid dynamics (CFD) based methods, in the course of the years several studies were devoted to the analysis of the flow around a propeller with a finite hub. Since the pioneering work of Lerbs (1952), where first the presence of an infinitely log hub of constant radius was taken into account through the use of corrective induction factors, much work both of theoretical and numerical nature has been carried out. McCormick (1955) extended the Goldstein (1929) analysis of the Betz optimum propeller to the case where the hub is represented by an infinitely long cylinder with an appreciable hub radius relative to the propeller one. In particular, McCormick (1955) calculated the distribution of the bound circulation of a rotor satisfying the Betz condition for minimum energy losses. McCormick (1955) gave the solution in terms of velocity potential expressed as an infinite series of modified Bessel and Lommel functions. Tachmindji (1956) investigated the same flow problem with a somewhat different boundary conditions treatment than the one proposed by McCormick (1955). Kerwin and Leopold (1964), assuming a zero slope for the bound circulation at the hub, coupled the trailing vortex system of the propeller, modelled through a vortex lattice method, with a image system for the hub vortex. J. B. Andrews and Cummings (1972) developed a design procedure for propellers with large hubs based upon a flow analysis method in which the hub is modelled with a line sink whose strength and position were calculated in such a way to satisfy the boundary condition at the hub surface. Ryan and Glover (1972) also presented a theoretical design method for ducted propellers based on a flow analysis system in which the duct and the boss are represented through a surface vorticity distribution, while the propeller is modelled with a modified lifting-line theory. The method was also applied to investigate the size of the boss required to produce a significant interaction effect with the duct. In Ludolph (1977) the hub was modelled through constant ring sources whose strength was determined in such a way that the average normal velocity vanished at the hub surface. Hess and Valarezo (1985) applied a surface panel method to study the flow about propellers with a center-body and a zero slope of the bound circulation at the hub. The body surfaces were approximated by a large number of flat quadrilateral panels distributed on the actual surface of the body. More in details, the propeller blades were modelled with sources and dipoles singularities, while the hub with sources

singularities. M. H. Wang (1985) proposed a numerical model for the design of propeller blade shape with a prescribed hub geometry. The blades and their wakes are modelled by means of the vortex lattice approach, while the hub is represented by a distribution of dipoles ending at the hub apex. The numerical results were also compared with experimental data. As a preliminary approach to predict propeller-hull interaction, Stern et al. (1988b) applied an actuator disk method in combination with modern CFD techniques to a propeller-shaft configuration. Stern et al. (1988b) solved RANS equations for a rotor with a finite hub by representing the propeller through a set of radial body-force distributed over the span of a disk with finite thickness. More in detail, Stern et al. (1988b) coupled in an interactive and iterative manner the partially-parabolic method of Chen and Patel (1985) with the vortex-lattice lifting-surface model developed by Kerwin and C. S. Lee (1978). Finally, the method was validated comparing computational results with the experimental data of M. H. Wang (1985). Further validation of the method of Stern et al. (1988b) has been provided by Stern, Toda, and H. T. Kim (1991) who carried out a detailed comparison with experimental data for the practical configuration of the Iowa axisymmetric body. The approach of Stern et al. (1988b) was also adopted by D. H. Zhang et al. (1991) to study a few propeller-hub configurations. Y. H. Liu and Ikehata (1995) investigated the flow around a propeller using the surface vortex lattice method for the hub and the ordinary vortex lattice method for the blade. Moreover, to avoid the strong interference effects between the blade root vortex and the hub surface vortex lattices, the latter were placed inside the actual hub surface. In order to investigate the scale effects, which often affect the experimental data for ducted propeller, Hoekstra (2006) employed a RANS-based computational model by representing the propeller as an actuator disk of finite thickness with a prescribed distribution of axial and tangential forces. A great attention was devoted by the author to analysis of the effects of a few geometrical parameters like the presence and shape of the hub, the radial loading distribution, and the influence of the tip gap.

This chapter presents an extension of the semi-analytical actuator disk of Conway (1998) capable to deal with hub of finite thickness. As reported in Chapter 1 for a ducted rotor without an hub, the method strongly couples the semi-analytical actuator disk of Conway (1998) (employed to model the rotor effect) with the classical vortex method of Martensen (1959) (adopted to simulate the hub presence). Comparing this method with the classical linearised actuator disk theory, it immediately appears that the present procedure can fully take into account the mutual interaction between the hub and the rotor, and the convergence/divergence of the slipstream with the

associated nonlinear effects which become more and more significant as the rotor load increases. Furthermore, the method can deal with hubs of general shape, rotors with variable radial distribution of the load, and wakes with and without slipstream rotation. The method being cost effective, it is well suited for the design and/or analysis of rotors with a finite hub. Finally, the results obtained with the semi-analytical actuator disk are reported in §4.3 and validated against the results obtained with a CFD actuator disk based method in §4.4.

## 4.2 The nonlinear actuator disk flow model with finite hub

In the following section, a brief description of the theoretical aspects characterising the flow problem is firstly presented. More in particular, in the first subsection, the mathematical treatment developed in Chapter 1 for the flow around an actuator disk coupled with an axisymmetric duct is summarized and generalized to allow the treatment of an open actuator disk with finite and axisymmetric hub. Therefore, the detailed and thorough analysis of the mathematical aspects related to this issue can be found in Chapter 1 and references therein. At the end of the first subsection, the exact solution of the through-flow problem, although in an implicit formulation, is furnished. Finally, in the second and last subsection a semi-analytical procedure aimed at computing the solution in the entire field is developed and discussed in details.

### 4.2.1 Theoretical aspects

Consider an actuator disk centered in the origin of a cylindrical coordinate system  $(\zeta, \sigma, \theta)$  where  $\zeta$  is the axial,  $\sigma$  is the radial and  $\theta$  is the tangential coordinate, respectively. Consider then an axisymmetric body with axis in the  $\zeta$  direction. Following the classical approach of Wu (1962), Bontempo and Manna (2013) (see Chapter 1) proved that the governing equation of the steady, axisymmetric, incompressible, and inviscid flow around the actuator disk and the axisymmetric body reads

$$\frac{\partial^2 \Psi}{\partial \sigma^2} - \frac{1}{\sigma} \frac{\partial \Psi}{\partial \sigma} + \frac{\partial^2 \Psi}{\partial \zeta^2} = -\omega_\theta \sigma \quad (4.1)$$

where  $\Psi$  is the Stokes stream function defined as

$$u = \frac{1}{\sigma} \frac{\partial \Psi}{\partial \sigma}, \quad v = -\frac{1}{\sigma} \frac{\partial \Psi}{\partial \zeta}, \quad (4.2)$$

and  $\boldsymbol{\omega} = (\omega_\zeta, \omega_\sigma, \omega_\theta) = (0, 0, \omega_\theta)$  is the vorticity vector. Moreover, making use of the momentum equation, the tangential vorticity  $\omega_\theta$  can be expressed as (Wu 1962)

$$\frac{\omega_\theta}{\sigma} = \left( \frac{\mathcal{H}}{\Omega^2 \sigma^2} - 1 \right) \frac{d\mathcal{H}}{d\Psi} \quad (4.3)$$

inside the slipstream, while  $\omega_\theta/\sigma = 0$  outside the slipstream. In the above equation  $\mathcal{H}(\Psi)$  is the jump through the disk of the Bernoulli constant  $H = p/\rho + 1/2(u^2 + v^2 + w^2)$ , where  $(u, v, w)$  is the velocity vector field and  $\rho$  is the density. Note that the slipstream edge  $\sigma_s(\zeta)$  dividing the rotor wake from the rest of the domain is not known in advance and must be determined iteratively through the procedure described in §4.2.2.

Returning to the through-flow differential equation (4.1), the following conditions at infinity and at the body section contour  $C$  have also to be satisfied:

$$\frac{1}{\sigma} \frac{\partial \Psi}{\partial \sigma} \rightarrow U_\infty, \quad \frac{\partial \Psi}{\partial \zeta} \rightarrow 0 \quad \text{as } \zeta \rightarrow -\infty \quad \text{or } \sigma \rightarrow \infty, \quad (4.4a)$$

$$\frac{\partial \Psi}{\partial \zeta} \rightarrow 0 \quad \text{as } \zeta \rightarrow +\infty, \quad (4.4b)$$

$$\Psi = \Psi_0 = \text{const.} \quad \text{on } C. \quad (4.4c)$$

The physical meaning of conditions (4.4a) and (4.4b) can be easily understood making use of the Stokes stream function definition (4.2). More in particular, the previous conditions require that the axial velocity, far away from the slipstream, has to reach the free-stream velocity value  $U_\infty$ , while the radial velocity has to go to zero everywhere at infinity. Equation (4.4c) is a no-penetration condition on the body section contour  $C$ . In order to complete the formulation of the differential problem (4.1)-(4.4), the load distribution at the disk  $\mathcal{H}(\Psi)$ , the angular velocity  $\Omega$  and, obviously, the hub geometry have to be prescribed.

Assuming that the rotor hub is axisymmetric the differential problem (4.1)-(4.4) with  $\Psi_0 = 0$  can also be used to study the flow around an actuator disk with a finite and axisymmetric center-body, which is the purpose of the present chapter.

Once the through-flow solution has been obtained by solving problem (4.1)-(4.4), the tangential velocity can be computed by means of the angular

momentum equation

$$\mathcal{H}(\Psi) = \Omega\sigma w. \quad (4.5)$$

Applying the Hankel transform with respect to  $\sigma$ , Wu (1962) (see Breslin and Andersen (1994) for a detailed description of the mathematical procedure) proved that the Green function of the linear elliptic operator at the right-hand side of equation (4.1) is:

$$G(\sigma, r, \zeta - z) = \frac{1}{2} \int_0^\infty e^{-s|\zeta-z|} J_1(sr) J_1(s\sigma) ds, \quad (4.6)$$

where  $J$  is the Bessel function of the first kind. The above equation can also be related to the stream function of a ring vortex with unit radius and strength (see Chapter 1). This suggests that the flow around the actuator disk with a finite and axisymmetric hub can be modelled by a superposition of ring vortices distributed in the slipstream vortical region and over the hub surface. To this end,  $c$  being the curvilinear abscissa describing the hub section contour  $C$ , it is convenient to introduce the density strengths  $\gamma_{ad}(\zeta, \sigma)$  and  $\gamma_h(c)$  for the actuator disk slipstream and the hub singularities distribution, respectively. In more detail, the stream function and velocity components induced by an isolate ring vortex of strength  $\kappa$ , radius  $r$  and centered at  $(\zeta = z, \sigma = 0)$  are (Basset 1888; Lamb 1932)

$$\frac{\Psi'(\zeta, \sigma)}{\sigma} = \frac{\kappa r}{2} \int_0^\infty e^{-s|\zeta-z|} J_1(sr) J_1(s\sigma) ds, \quad (4.7)$$

$$u'(\zeta, \sigma) = \frac{\kappa r}{2} \int_0^\infty e^{-s|\zeta-z|} s J_1(sr) J_0(s\sigma) ds, \quad (4.8)$$

$$v'(\zeta, \sigma) = \pm \frac{\kappa r}{2} \int_0^\infty e^{-s|\zeta-z|} s J_1(sr) J_1(s\sigma) ds, \quad (4.9)$$

with the positive sign for  $\zeta - z \geq 0$  and vice versa. Therefore, the superposition of the ring vortex stream functions can be simply obtained by integrating equation (4.7) over the slipstream domain and the hub section contour:

$$\begin{aligned} \frac{\Psi(\zeta, \sigma)}{\sigma} &= \frac{1}{2} \int_0^\infty \int_{\sigma_h(z)}^{\sigma_s(z)} \int_0^\infty e^{-s|\zeta-z|} \gamma_{ad}(z, r) r J_1(sr) J_1(s\sigma) ds dr dz + \\ &\quad \underbrace{\frac{1}{2} \oint_C \int_0^\infty \gamma_h(c) r(c) e^{-s|\zeta-z|} J_1(sr(c)) J_1(s\sigma) ds dc}_{\Psi_h(\zeta, \sigma)} + \frac{U_\infty \sigma}{2}. \end{aligned} \quad (4.10)$$

In the above equation, which constitutes the exact and implicit form of the coupled through-flow solution,  $\sigma_h(\zeta)$  is the function describing the hub shape. Obviously,  $\sigma_h(\zeta) = 0$  for  $\zeta \leq \zeta_{h,LE}$  and  $\zeta \geq \zeta_{h,TE}$ , where  $\zeta_{h,LE}$  and  $\zeta_{h,TE}$  are axial position of the hub leading edge and trailing edge, respectively. The first term of the right-hand side of equation (4.10) is the Stokes stream function induced at the point  $(\zeta, \sigma)$  by the continuum singularity distribution of the actuator disk wake and it is simply obtained by integrating equation (4.7) for  $\sigma_h(\zeta) \leq \sigma \leq \sigma_s(\zeta)$  and  $0 \leq \zeta \leq +\infty$ , i.e. over the rotor slipstream. The second term of the right-hand side of equation (4.10), which is obtained by integrating equation (4.7) over the hub section contour  $C$ , is the Stokes stream function induced at the point  $(\zeta, \sigma)$  by the ring vortex sheet representing the hub, and, finally, the last term is the contribution of the free stream. It can be shown that, in order to satisfy equation (4.1) and the associated boundary conditions (4.4), the density strength  $\gamma_{ad}(\zeta, \sigma)$  has to be equal to the tangential component of the vorticity  $\omega_\theta(\zeta, \sigma)$  in the wake (see Conway (1998) for details), i.e.

$$\gamma_{ad}(\zeta, \sigma) = \omega_\theta(\zeta, \sigma). \quad (4.11)$$

Furthermore, in order to make the hub a stream surface, the tangent to the wall velocity just beneath the hub vorticity sheet has to satisfy the homogeneous Dirichlet boundary condition (Martensen 1959) which can be expressed through the following Fredholm second kind integral equation:

$$-\frac{1}{2}\gamma_h(c) + \oint_C k(c, \tilde{c})\gamma_h(\tilde{c}) d\tilde{c} + (U_\infty + u_{ad}(c)) \cos \beta(c) + v_{ad}(c) \sin \beta(c) = 0, \quad (4.12)$$

where  $\beta(c)$  is the local profile slope and  $k(c, \tilde{c})$  is the velocity parallel to the surface at  $c$ , induced by a ring vortex of unit strength located at  $\tilde{c}$ . The first term in (4.12) is precisely half the velocity jump across the sheet, while the second is the velocity induced at  $c$  by the vortices used to model the hub surface. Finally, the last two terms represent the tangent to the wall component of the free stream velocity  $U_\infty$  and of the velocity induced by the ring vortex distribution modelling the actuator disk slipstream, respectively. The velocities  $u_{ad}(c)$  and  $v_{ad}(c)$  can be evaluated by integrating equations (4.8) and (4.9) over the wake, thus obtaining

$$u_{ad}(\zeta, \sigma) = \frac{1}{2} \int_0^\infty \int_{\sigma_h(z)}^{\sigma_s(z)} \int_0^\infty e^{-s|\zeta-z|} \gamma_{ad}(z, r) sr J_1(sr) J_0(s\sigma) ds dr dz, \quad (4.13)$$

$$v_{ad}(\zeta, \sigma) = \pm \frac{1}{2} \int_0^\infty \int_{\sigma_h(z)}^{\sigma_s(z)} \int_0^\infty e^{-s|\zeta-z|} \gamma_{ad}(z, r) sr J_1(sr) J_1(s\sigma) ds dr dz. \quad (4.14)$$

Comparing the actuator disk with a finite hub with the original method of Conway (1998) and Bontempo and Manna (2013) (see Chapter 1), a few differences in the expressions of the stream function and of the induced velocities appear. In fact, the radial integration in the first term of the right-hand side of equations (4.10), (4.13) and (4.14) differ for the lower limit (0 in the original method,  $\sigma_h(z)$  in the new one), the upper limit remaining the same. This produces significant changes in the semi-analytical approach to be used to compute the solution, as described in the following subsection §4.2.2.

### 4.2.2 The semi-analytical solution procedure

Applying the additivity property of integration on intervals to equations (4.10), (4.13) and (4.14), the following equivalent expression can be obtained:

$$\begin{aligned} \frac{\Psi(\zeta, \sigma)}{\sigma} = & \frac{1}{2} \int_0^\infty \left\{ \left[ \int_0^{\sigma_s(z)} \int_0^\infty e^{-s|\zeta-z|} \omega_\theta(z, r) r J_1(sr) J_1(s\sigma) ds dr \right] \right. \\ & \left. - \left[ \int_0^{\sigma_h(z)} \int_0^\infty e^{-s|\zeta-z|} \omega_\theta(z, r) r J_1(sr) J_1(s\sigma) ds dr \right] \right\} dz + \frac{\Psi_h(\zeta, \sigma)}{\sigma}, \end{aligned} \quad (4.15)$$

$$\begin{aligned} u_{ad}(\zeta, \sigma) = & \frac{1}{2} \int_0^\infty \left\{ \left[ \int_0^{\sigma_s(z)} \int_0^\infty e^{-s|\zeta-z|} \omega_\theta(z, r) sr J_1(sr) J_0(s\sigma) ds dr \right] \right. \\ & \left. - \left[ \int_0^{\sigma_h(z)} \int_0^\infty e^{-s|\zeta-z|} \omega_\theta(z, r) sr J_1(sr) J_0(s\sigma) ds dr \right] \right\} dz, \end{aligned} \quad (4.16)$$

$$\begin{aligned} v_{ad}(\zeta, \sigma) = & \pm \frac{1}{2} \int_0^\infty \left\{ \left[ \int_0^{\sigma_s(z)} \int_0^\infty e^{-s|\zeta-z|} \omega_\theta(z, r) sr J_1(sr) J_1(s\sigma) ds dr \right] \right. \\ & \left. - \left[ \int_0^{\sigma_h(z)} \int_0^\infty e^{-s|\zeta-z|} \omega_\theta(z, r) sr J_1(sr) J_1(s\sigma) ds dr \right] \right\} dz. \end{aligned} \quad (4.17)$$

In the above equations, the density strength of the actuator disk slipstream singularities distribution  $\gamma_{ad}(\zeta, \sigma)$  has been substituted with the tangential

vorticity distribution  $\omega_\theta(\zeta, \sigma)$ , as follows from equation (4.11). The integrals in the first square brackets of equations (4.15), (4.16) and (4.17) are also present in the solution for the actuator disk without hub and, consequently, they will be computed through the procedure described in Conway (1998). Instead, the integrals in the second square brackets are due to the presence of a finite hub and they obviously have to be computed only for  $0 < z < \zeta_{h,TE}$  since they vanish elsewhere.

As discussed in the previous subsection, equation (4.15) can be regarded as the exact solution of the through-flow problem. Unfortunately, it is an implicit form solution because the unknowns  $\sigma_s(\zeta)$ ,  $\omega_\theta(\zeta, \sigma)$  and  $\Psi_h(\zeta, \sigma)$  all depend upon the Stokes stream function  $\Psi$ . To overcome this problem, an iterative procedure, aimed at computing the overall Stokes stream function  $\Psi$ , has been developed as deeply detailed in this subsection. Following the approach suggested by Conway (1998), the load is supposed to be a continuous function which can be cast in the following polynomial form

$$\widehat{\mathcal{H}} = 2\widehat{\Psi}_{ad} \sum_{m=0}^M b_m \left( \frac{\Psi}{\Psi_{ad}} \right)^m, \quad (4.18)$$

where  $\widehat{\mathcal{H}} = 2\mathcal{H}/U_\infty^2$ ,  $\widehat{\Psi}_{ad}$  is the dimensionless Stokes stream function at the actuator disk radius defined as  $\widehat{\Psi}_{ad} = \Psi_{ad}/U_\infty\sigma_{ad}^2$  and  $\sigma_{ad}$  is the actuator disk radius. Assuming that  $\mathcal{H}(\Psi)$  is also  $C^1$  continuous it follows, from equations (4.18) and (4.3), that the tangential vorticity can be expressed as

$$\frac{\omega_\theta(\zeta, \sigma)}{\sigma} = \left[ \frac{J^2}{\pi^2} \frac{\Psi_{ad}}{U_\infty\sigma^2} \left( \sum_{m=0}^M b_m \left( \frac{\Psi}{\Psi_{\sigma_{ad}}} \right)^m \right) - 1 \right] \frac{U_\infty}{\sigma_{ad}^2} \sum_{m=1}^M m b_m \left( \frac{\Psi}{\Psi_{\sigma_{ad}}} \right)^{m-1}. \quad (4.19)$$

In the above equation, the advance coefficient  $J$  is defined as  $J = U_\infty/nD$ , where  $D = 2\sigma_{ad}$  is the rotor diameter and  $n$  is the rotational speed. In order to exactly perform the radial integration in (4.15), (4.16) and (4.17), Conway (1998) suggested to express the tangential vorticity as a function of  $\zeta$  and  $\sigma$  through the following polynomial expansion:

$$\frac{\omega_\theta(\zeta, \sigma)}{\sigma} = \sum_{n=0}^N A_n(\zeta) \left[ 1 - \left( \frac{\sigma}{\sigma_s(\zeta)} \right)^2 \right]^n. \quad (4.20)$$

Substituting equation (4.20) in equation (4.15) and applying the linearity

property of integration, it gives

$$\begin{aligned} \frac{\Psi(\zeta, \sigma)}{\sigma} &= \frac{\Psi_h(\zeta, \sigma)}{\sigma} \\ &+ \frac{1}{2} \int_0^\infty \left\{ \sum_{n=0}^N \left[ A_n(z) \int_0^\infty e^{-s|\zeta-z|} J_1(s\sigma) \left( \int_0^{\sigma_s(z)} \left( 1 - \frac{r^2}{\sigma_s^2(z)} \right)^n r^2 J_1(sr) dr \right) ds \right] \right. \\ &\left. - \left[ \int_0^{\sigma_h(z)} \left( \sum_{n=0}^N A_n(z) \left( 1 - \frac{r^2}{\sigma_s^2(z)} \right)^n \right) r^2 \left( \int_0^\infty e^{-s|\zeta-z|} J_1(sr) J_1(s\sigma) ds \right) dr \right] \right\} dz. \end{aligned} \quad (4.21)$$

The inner radial integral in the first square brackets of the above equation can be performed employing the variable substitution  $x = r/\sigma_s(z)$  and then using the following integral due to Sonine (1880):

$$\int_0^1 x^{\nu+1} (1-x^2)^\mu J_\nu(bx) dx = 2^\mu \Gamma(\mu+1) b^{-(\mu+1)} J_{\nu+\mu+1}(b), \quad (4.22)$$

where  $\Gamma(n)$  is the Gamma function which is equal to  $(n-1)!$  if  $n$  is a positive integer. With the help of equation (4.22), equation (4.21) becomes

$$\begin{aligned} \frac{\Psi(\zeta, \sigma)}{\sigma} &= \int_0^\infty \left\{ \left[ \sum_{n=0}^N A_n(z) 2^{n-1} n! \sigma_s^{2-n}(z) I_{(-n-1, n+2, 1)}(\sigma_s(z), \sigma, \zeta - z) \right] \right. \\ &\left. - \frac{1}{2} \left[ \int_0^{\sigma_h(z)} \left( \sum_{n=0}^N A_n(z) \left( 1 - (r/\sigma_s(z))^2 \right)^n \right) r^2 I_{(0, 1, 1)}(\sigma_s(z), \sigma, \zeta - z) dr \right] \right\} dz \\ &+ \frac{\Psi_h(\zeta, \sigma)}{\sigma}, \end{aligned} \quad (4.23)$$

The integrals  $I_{(\xi, \mu, \nu)}$  appearing in (4.23), with  $\xi$ ,  $\mu$  and  $\nu$  integers, are of the type:

$$I_{(\xi, \mu, \nu)} = \int_0^\infty e^{-s|\zeta-z|} s^\xi J_\mu(sr) J_\nu(s\sigma) ds$$

and each of them can be expressed in terms of complete elliptic integrals and the Heuman Lambda function through the recursive scheme detailed in Conway (2000). The integral  $I_{(0, 1, 1)}$  can be directly calculated as follows (Gradshteyn and Ryzhik 1980)

$$I_{(0, 1, 1)} = \frac{1}{\pi \sqrt{r\sigma}} Q_{1/2} \left( \frac{2-k^2}{k^2} \right) = \frac{1}{\pi \sqrt{r\sigma}} \frac{[(2-k^2)K(k) - 2E(k)]}{k}, \quad (4.24)$$

where  $Q$  is the Legendre function of second kind,  $K$  and  $E$  are complete elliptic integrals of the first and second kind and  $k = \sqrt{4r\sigma/((r+\sigma)^2 + |\zeta - z|^2)}$ . Finally, the radial integral in the second square brackets and the axial one can be performed through numerical quadrature methods. Following the same procedure, the axial and radial velocities induced by the slipstream singularities distribution at the point  $(\zeta, \sigma)$ , i.e. equations (4.16) and (4.17), become

$$u_{ad}(\zeta, \sigma) = \int_0^\infty \left\{ \left[ \sum_{n=0}^N A_n(z) 2^{n-1} n! \sigma_s^{2-n}(z) I_{(-n, n+2, 0)}(\sigma_s(z), \sigma, \zeta - z) \right] - \frac{1}{2} \left[ \int_0^{\sigma_n(z)} \left( \sum_{n=0}^N A_n(z) \left( 1 - \frac{r^2}{\sigma_s^2(z)} \right)^n \right) r^2 I_{(1, 1, 0)}(\sigma_s(z), \sigma, \zeta - z) dr \right] \right\} dz, \quad (4.25)$$

$$v_{ad}(\zeta, \sigma) = \pm \int_0^\infty \left\{ \left[ \sum_{n=0}^N A_n(z) 2^{n-1} n! \sigma_s^{2-n}(z) I_{(-n, n+2, 1)}(\sigma_s(z), \sigma, \zeta - z) \right] - \frac{1}{2} \left[ \int_0^{\sigma_n(z)} \left( \sum_{n=0}^N A_n(z) \left( 1 - \frac{r^2}{\sigma_s^2(z)} \right)^n \right) r^2 I_{(1, 1, 1)}(\sigma_s(z), \sigma, \zeta - z) dr \right] \right\} dz, \quad (4.26)$$

with (Gradshteyn and Ryzhik 1980)

$$I_{(1, 1, 0)} = \frac{k \left[ k^2(r^2 - \sigma^2 - |\zeta - z|^2)E(k) + 4r\sigma(1 - k^2)K(k) \right]}{8\pi(1 - k^2)\sqrt{r^5\sigma^3}}, \quad (4.27)$$

$$I_{(1, 1, 1)} = \frac{|\zeta - z|k \left[ (2 - k^2)E(k) - 2(1 - k^2)K(k) \right]}{4\pi(1 - k^2)\sqrt{(r\sigma)^3}}. \quad (4.28)$$

In order to evaluate  $\Psi$  via equation (4.23), the Stoke stream function associated to the hub ring vortex sheet  $\Psi_h$  must also be computed. The latter is a function of the density strength distribution  $\gamma_h(c)$  which, in order to fulfil the no-penetration requirement on the hub wall surface, has to satisfy the second kind Fredholm integral equation (4.12). The numerical solution of this equation is carried out by using a classical panel method (Lewis 1991). In particular, the hub section profile is represented through a polyline consisting of  $M_p$  segments with length  $\Delta c_n$ . Using the trapezium rule on each of these segments (panels), the following system of  $M_p \times M_p$  linear algebraic

equations can be obtained:

$$\sum_{n=1}^{M_p} K(c_m, c_n) \gamma_h(c_n) = -(U_\infty + u_{ad,m}) \cos \beta_m - v_{ad,m} \sin \beta_m \quad m=1, \dots, M_p. \quad (4.29)$$

The actuator disk induced velocities  $u_{ad,m}$  and  $v_{ad,m}$ , appearing in the above equation, can be evaluated by means of equations (4.16) and (4.17), respectively. The entries of matrix  $K$ , which are equal to  $k(c_m, c_n) \Delta c_n$  when  $n \neq m$  and  $k(c_m, c_m) \Delta c_m - \frac{1}{2} \gamma_d(c_m)$  for  $n = m$ , represent the tangent to the wall velocity induced at  $c_m$  by the ring vortex of unit strength located at  $c_n$ . Finally, the  $K$  matrix coefficients can be computed through (Gibson 1972)

$$K(c_m, c_n) = (u_{mn} \cos \beta_m + v_{mn} \sin \beta_m) \Delta c_n,$$

with

$$u_{mn} = -\frac{1}{2\pi\sigma_n \sqrt{\zeta^{*2} + (\sigma^* + 1)^2}} \left\{ K(k) - \left[ 1 + \frac{2(\sigma^* - 1)}{\zeta^{*2} + (\sigma^* - 1)^2} \right] E(k) \right\},$$

$$v_{mn} = \frac{\zeta^*/\sigma^*}{2\pi\sigma_n \sqrt{\zeta^{*2} + (\sigma^* + 1)^2}} \left\{ K(k) - \left[ 1 + \frac{2\sigma^*}{\zeta^{*2} + (\sigma^* - 1)^2} \right] E(k) \right\}.$$

In the above equations  $k = \sqrt{4\sigma^*/[\zeta^{*2} + (\sigma^* + 1)^2]}$ ,  $\sigma^* = \sigma_m/\sigma_n$  and  $\zeta^* = (\zeta_m - \zeta_n)/\sigma_n$ . The inner integral in the  $\Psi_h$  definition (see equation (4.10)) is of the  $I_{(0,1,1)}$  type and can be exactly computed through (4.24). Finally, once the  $\gamma_h(c)$  has been obtained by solving system (4.29), the Stokes stream function  $\Psi_h$ , computed by using the trapezium rule, reads:

$$\Psi_h(\zeta, \sigma) = \sum_{m=1}^{M_p} \frac{\gamma_h(c_m) \Delta c_m \sqrt{\sigma \sigma_m}}{2\pi} Q_{1/2} \left( 1 + \frac{(\sigma_m - \sigma)^2 + (\zeta - \zeta_m)^2}{(2\sigma_m \sigma)} \right) + \frac{U_\infty \sigma^2}{2}. \quad (4.30)$$

The integration of (4.23), (4.25) and (4.26) is still prevented since, as anticipated in §4.2.1, the  $\sigma_s(\zeta)$  distribution is not known in advance and must be determined as a part of the solution. The problem is solved by working out the following iterative procedure, which is similar to that developed in Chapter 1. First of all, note that the Stokes stream function is constant along the slipstream edge  $\sigma_s(\zeta)$ ; thus equation (4.23) reduces there on to

the following nonlinear integral equation for  $\sigma_s(\zeta)$ :

$$\begin{aligned} \Psi(0, \sigma_{ad}) &= \frac{U_\infty \sigma_s^2(\zeta)}{2} + \Psi'_h(\zeta, \sigma_s(\zeta)) \\ &+ \sigma_s(\zeta) \int_0^\infty \left\{ \left[ \sum_{n=0}^N A_n(z) 2^{n-1} n! \sigma_s^{2-n}(z) I_{(-(n+1), n+2, 1)}(\sigma_s(z), \sigma_s(z), \zeta - z) \right] \right. \\ &\left. - \frac{1}{2} \left[ \int_0^{\sigma_n(z)} \left( \sum_{n=0}^N A_n(z) \left( 1 - \frac{r}{\sigma_s^2(z)} \right)^n \right) r^2 I_{(0, 1, 1)}(\sigma_s(z), \sigma_s(z), \zeta - z) dr \right] \right\} dz, \end{aligned} \quad (4.31)$$

with  $\Psi'_h = \Psi_h - \frac{1}{2} U_\infty \sigma^2$ . The procedure consists of the following steps:

1. The geometry of the hub and the value of the advance coefficient  $J$  are first defined.
2. From equation (4.18), the load distribution  $\mathcal{H}(\Psi)$  is prescribed through  $M$  coefficients  $b_m$ .
3. The matrix  $K$  and its LU decomposition is computed and stored. Note that the entries of matrix  $K$  straightforwardly depend upon the duct geometry.
4. Provisional values of  $\gamma_h(c_m)$  are assumed to be available from the previous iteration.
5. Provisional values of  $\sigma_s(\zeta)$  and  $\{A_n(\zeta)\}_{n=0, N}$  are assumed to be available from the previous iteration at  $n_z$  axial stations.
6. The wake is meshed through a  $n_{zs} \times n_{rs}$  grid, where  $n_{zs}$  and  $n_{rs}$  are the number of axial and radial stations, respectively.
7. The radial integral in equation (4.23) is performed through an adaptive Simpson quadrature scheme (Lyness 1970).
8. The integral in the axial direction, appearing in (4.23), is carried out by the same quadrature scheme. In this way the Stokes stream function  $\Psi$  can be evaluated at all grid points.
9. From equation (4.19), the tangential vorticity  $\omega_\theta$  is computed at all grid points.

10. With the help of a least-squares minimization procedure, the  $\omega_\theta$  distribution, computed at step 9, is parametrized with a new set of  $\{A_n(\zeta)\}_{n=0,N}$ .
11. The axial and radial velocities induced by the actuator disk at the hub section profile are computed (equations (4.25) and (4.26)).
12. Consequently the right-hand side of equation (4.29) and  $\gamma_h(c_m)$  for  $m = 1, \dots, M_P$  can be updated.
13. From (4.31), the new  $\sigma_s(\zeta)$  is re-evaluated through:

$$\sigma_s(\zeta) = \sqrt{\left(\frac{\Psi'_d(\zeta, \sigma_s(\zeta))}{\sigma_s(\zeta)U_\infty} + \frac{I(\zeta, \sigma_s(\zeta))}{U_\infty}\right)^2 + \frac{2\Psi(0, \sigma_{ad})}{U_\infty} - \frac{\Psi'_h(\zeta, \sigma_s(\zeta))}{\sigma_s(\zeta)U_\infty} - \frac{I(\zeta, \sigma_s(\zeta))}{U_\infty}},$$

where

$$\begin{aligned} I(\zeta, \sigma_s(\zeta)) &= \\ &= \int_0^\infty \left\{ \left[ \sum_{n=0}^N A_n(z) 2^{n-1} n! \sigma_s^{2-n}(z) I_{(-(n+1), n+2, 1)}(\sigma_s(z), \sigma_s(z), \zeta - z) \right] \right. \\ &\quad \left. - \frac{1}{2} \left[ \int_0^{\sigma_h(z)} \left( \sum_{n=0}^N A_n(z) \left( 1 - \frac{r^2}{\sigma_s^2(z)} \right)^n \right) r^2 I_{(0, 1, 1)}(\sigma_s(z), \sigma_s(z), \zeta - z) dr \right] \right\} dz \end{aligned}$$

14. Since the iterative procedure convergence worsens with the load increase, an under-relaxation technique is used to update the slipstream edge  $\sigma_s(\zeta)$  at each iteration. More in particular, the relation

$$\sigma_s(\zeta) = \sigma_s(\zeta)|_{old} + [\sigma_s(\zeta)|_{new} - \sigma_s(\zeta)|_{old}] \omega_{rf}$$

is employed, where  $\omega_{rf}$  is the relaxation factor.

15. Go to item 5 until convergence of the slipstream  $\sigma_s(\zeta)$  is reached.

At the first iteration  $\gamma_h(c_m)$ ,  $\sigma_s(\zeta)$  and  $\Psi$  are calculated ignoring the presence of the disk.

$\zeta/\sigma_{ad}$	$\sigma/\sigma_{ad}$	$\zeta/\sigma_{ad}$	$\sigma/\sigma_{ad}$
-1.0482	0.0000	0.0518	0.3735
-1.0460	0.0264	0.1209	0.3707
-1.0395	0.0557	0.1897	0.3658
-1.0287	0.0829	0.2579	0.3585
-1.0136	0.1096	0.3254	0.3490
-0.9944	0.1354	0.3917	0.3372
-0.9709	0.1602	0.4568	0.3232
-0.9435	0.1837	0.5202	0.3072
-0.9121	0.2057	0.5818	0.2893
-0.8770	0.2260	0.6412	0.2698
-0.8381	0.2444	0.6984	0.2489
-0.7958	0.2607	0.7530	0.2269
-0.7501	0.2745	0.8048	0.2041
-0.7012	0.2861	0.8537	0.1808
-0.6494	0.2974	0.8994	0.1573
-0.5948	0.3088	0.9417	0.1343
-0.5376	0.3199	0.9806	0.1120
-0.4781	0.3305	1.0158	0.0909
-0.4165	0.3404	1.0471	0.0713
-0.3531	0.3495	1.0746	0.0535
-0.2881	0.3575	1.0980	0.0378
-0.2217	0.3641	1.1173	0.0246
-0.1543	0.3692	1.1323	0.0140
-0.0861	0.3726	1.1432	0.0063
-0.0173	0.3740	1.1497	0.0016
		1.1518	0.0000

Table 4.1: Hub coordinates.

### 4.3 Discussion and analysis of the results

As anticipated in sections §4.2.1 and §4.2.2, in order to solve the differential problem (4.1)-(4.4) the load distribution at the disk  $\mathcal{H}(\Psi)$ , the advance coefficient  $J$ , and, obviously, the hub geometry have to be prescribed. In all cases reported in this chapter, the hub geometry detailed in Table 4.1 and a value of  $J = 0.5$  are used.

To correctly prescribe the load distribution at the disk some preliminarily considerations are needed. First of all, as customary in engineering applications, the load  $\mathcal{H}$  is required to fall to zero at the disk radius  $\sigma_{ad}$ ; this implies that  $\sum_{m=0}^M b_m = 0$  (see equation (4.18)). Instead, the load at the hub  $\mathcal{H}(0, \sigma_h(0))$  can be set both equal and different from zero. In particular, from equation (4.18), the value of the coefficient  $b_0$  can be simply related to the load at the hub  $\mathcal{H}(0, \sigma_h(0))$  by

$$b_0 = \frac{\mathcal{H}(0, \sigma_h(0))\sigma_{ad}^2}{U_\infty \Psi_{ad}} = \frac{\widehat{\mathcal{H}}(0, \sigma_h(0))}{2\widehat{\Psi}_{ad}}. \quad (4.32)$$

Furthermore, from equation (4.18), it readily follows that the value of the coefficient  $b_1$  is proportional to the load derivative with respect to  $\Psi$  calculated at the hub:

$$b_1 = \frac{\sigma_{ad}^2}{U_\infty} \frac{d\mathcal{H}}{d\Psi} \Big|_{\Psi=0} = 2 \frac{d\widehat{\mathcal{H}}}{d\widehat{\Psi}} \Big|_{\Psi=0}. \quad (4.33)$$

The load  $\mathcal{H}(0)$  and its derivative  $d\mathcal{H}/d\Psi|_{\Psi=0}$  at the hub, i.e. the coefficients  $b_0$  and  $b_1$ , must also be prescribed in such a way to prevent a singular behaviour of the tangential vorticity on the  $\zeta$  axis. In fact, by prescribing both  $\mathcal{H}(0)$  and  $d\mathcal{H}/d\Psi|_{\Psi=0}$  different from zero, it is easy to show that the function  $\omega_\theta/\sigma$  tends to  $\infty$  as  $\sigma \rightarrow 0$  (see equation (4.3)). The latter circumstance prevents to carry out point 10 of the iterative solution procedure since it is impossible to properly approximate in a least-squares sense the tangential vorticity singularity through the algebraic polynomial (4.20). Instead, by assuming  $\mathcal{H}(0) \neq 0$  and  $d\mathcal{H}/d\Psi|_{\Psi=0} = 0$ , equation (4.3) returns the indeterminate form  $\infty \cdot 0$  as  $\sigma \rightarrow 0$ . The tangential component of the vorticity can be evaluated by fixing  $b_1 = 0$  in equation (4.19) that, with some algebra, returns

$$\lim_{\sigma \rightarrow 0} \frac{\omega_\theta}{\sigma} = \lim_{\sigma \rightarrow 0} \left\{ \left[ \frac{J^2 \Psi}{\pi^2 U_\infty \sigma^2} \left( b_0 + \sum_{m=2}^M b_m \left( \frac{\Psi}{\Psi_{ad}} \right)^{m-1} \right) \right] \frac{U_\infty}{\sigma_{ad}^2} \sum_{m=2}^M m b_m \left( \frac{\Psi}{\Psi_{ad}} \right)^{m-2} \right\}.$$

Then, by applying the algebraic limit theorem, the above equation yields

$$\lim_{\sigma \rightarrow 0} \frac{\omega_\theta(\zeta, \sigma)}{\sigma} = \frac{2J^2}{\pi^2 \sigma_{ad}^2} b_2 b_0 \lim_{\sigma \rightarrow 0} \frac{\Psi}{\sigma^2},$$

which results in the form  $0/0$ . At last, employing the l'Hôpital's rule and making use of the Stokes stream function definition (4.2), the tangential vorticity on the axis reads

$$\lim_{\sigma \rightarrow 0} \frac{\omega_\theta(\zeta, \sigma)}{\sigma} = \frac{J^2}{\pi^2 \sigma_{ad}^2} b_2 b_0 u(\zeta, 0) \quad b_0 \neq 0, b_1 = 0$$

which is not a singular function. Finally, the tangential component of the vorticity also does not exhibit a singular behaviour on the axis for  $\mathcal{H}(0) = 0$ , i.e. for  $b_0 = 0$ . In this case equation (4.3) returns the indeterminate form  $0/0$ . Fixing  $b_0 = 0$  in equation (4.19) and applying the algebraic limit theorem it, with some algebra, returns

$$\lim_{\sigma \rightarrow 0} \frac{\omega_\theta(\zeta, \sigma)}{\sigma} = \left[ \frac{J^2}{\pi^2} \frac{\Psi_{ad}}{U_\infty} \left( \lim_{\sigma \rightarrow 0} \frac{\sum_{m=1}^M b_m \left( \frac{\Psi}{\Psi_{ad}} \right)^m}{\sigma^2} \right) - 1 \right] \frac{U_\infty}{\sigma_{ad}^2} b_1.$$

At the end, using the l'Hôpital's rule, the tangential vorticity on the axis becomes

$$\lim_{\sigma \rightarrow 0} \frac{\omega_\theta(\zeta, \sigma)}{\sigma} = \frac{U_\infty b_1}{\sigma_{ad}^2} \left( \frac{J^2}{2\pi^2} b_1 \frac{u(\zeta, 0)}{U_\infty} \right) \quad b_0 = 0$$

Summarizing, to properly assign the load distribution of an actuator disk with swirl the following conditions have to be satisfied:

$$\sum_{m=0}^M b_m = 0 \quad (4.34a)$$

$$b_0 = 0 \quad \text{or} \quad b_0 \neq 0 \text{ and } b_1 = 0 \quad (4.34b)$$

Figure 4.1 shows the computed radial distribution of the load  $\hat{\mathcal{H}}(0, \sigma/\sigma_{ad})$  at the disk and the projection of the generatrices of the stream-tubes onto the meridian plane obtained by prescribing  $M = 3$ ,  $b_0 = 1$ ,  $b_1 = 0$ ,  $b_2 = 10$  and  $b_3 = -11$ . Undoubtedly, the shape of the computed dimensionless load radial distribution  $\hat{\mathcal{H}}(0, \sigma/\sigma_{ad})$  has a good physical resemblance to that for a typical propeller (Figure 4.1 left). Figure 4.1 (right) clearly demonstrates

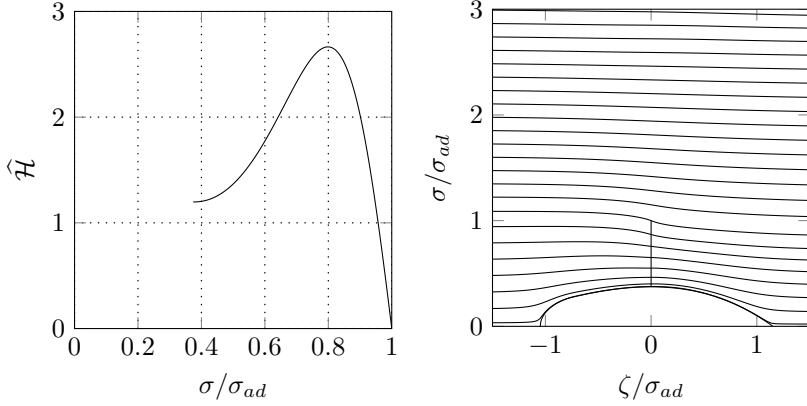


Figure 4.1: Load radial distribution (left) and projection of the generatrices of the stream-tubes onto the meridian plane (right).

$C_{T,rot}$	$C_{T,hub}$	$C_T$	$C_P$	$\eta$
1.540	-7.531E-2	1.465	2.276	0.644

Table 4.2: Semi-analytical actuator disk with finite hub: performance coefficients.

that the no-penetration boundary condition at the hub section profile is fully satisfied. Moreover, Figure 4.1 (right) also highlights the nonlinear effect of the slipstream contraction which is completely taken into account by the present method. Table 4.2 lists the predicted values for the global performance coefficients. As customary, the following classical definitions for the thrust and power coefficients have been employed:

$$C_{T,rot} = \frac{T_{rot}}{\frac{1}{2}\rho U_\infty^2 \pi \sigma_{ad}^2}, \quad C_{T,hub} = \frac{T_{hub}}{\frac{1}{2}\rho U_\infty^2 \pi \sigma_{ad}^2}, \quad C_P = \frac{P}{\frac{1}{2}\rho U_\infty^2 \pi \sigma_{ad}^2}, \quad (4.35)$$

where  $T_{rot}$  and  $T_{hub}$  are the rotor and hub axial thrust, respectively, and  $P$  is the rotor power exchange. Moreover, the total thrust coefficient can be expressed as  $C_T = C_{T,rot} + C_{T,hub}$ , while the propulsive efficiency is  $\eta = C_T/C_P$ . Figure 4.2 reports the radial distribution of the axial and radial velocity components at different axial stations. More in particular, Figure 4.2 shows that the radial velocity component is very small upstream

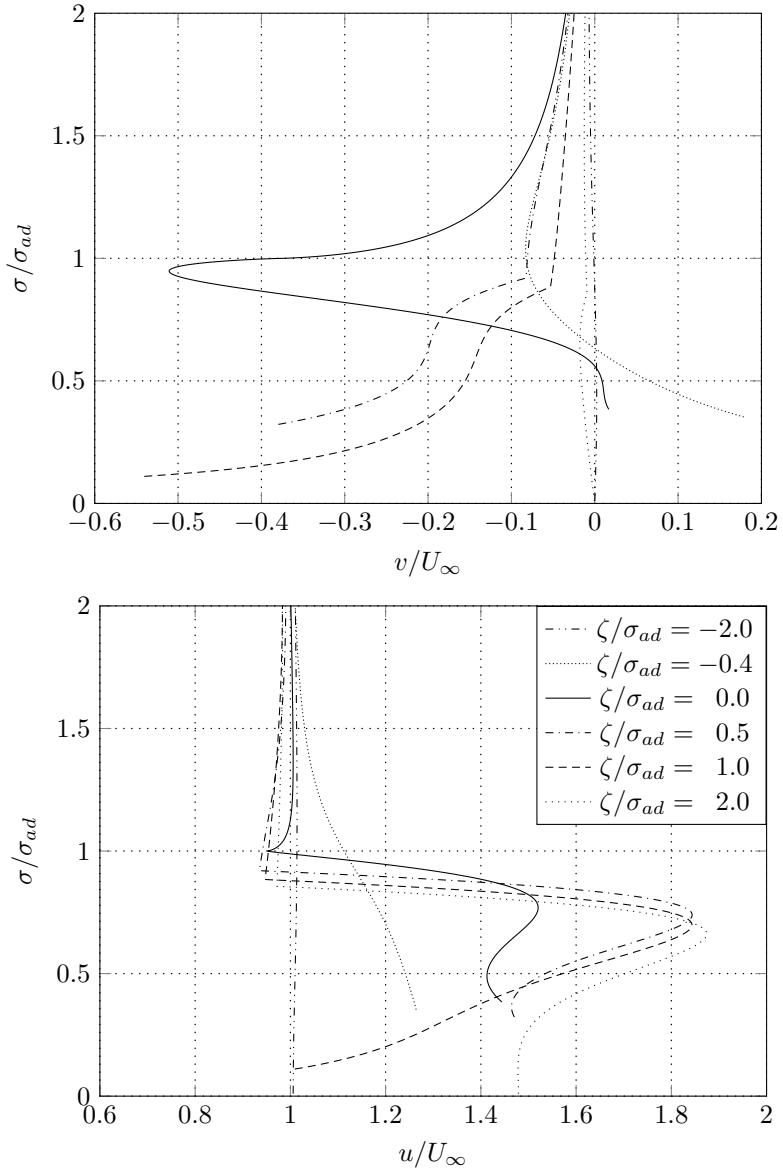


Figure 4.2: Radial (top) and axial (bottom) velocity profiles at different axial stations.

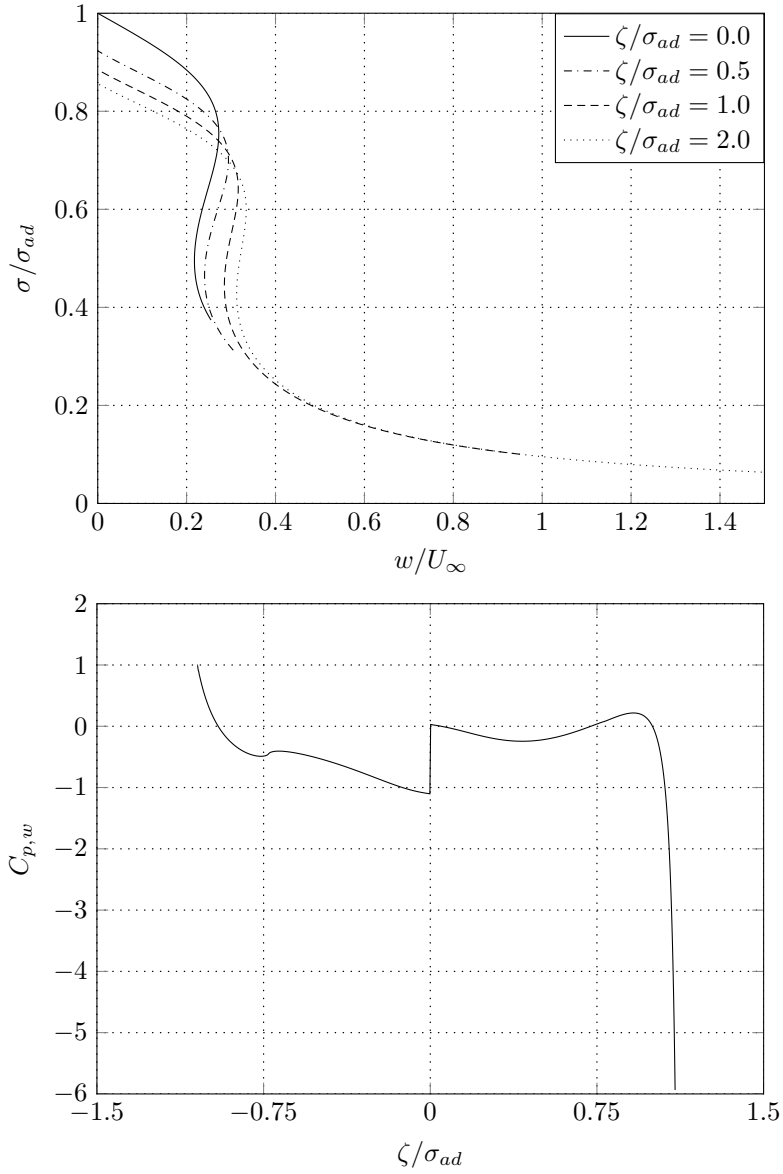


Figure 4.3: Tangential velocity profiles at different axial stations (top) and distribution of the wall pressure coefficient (bottom).

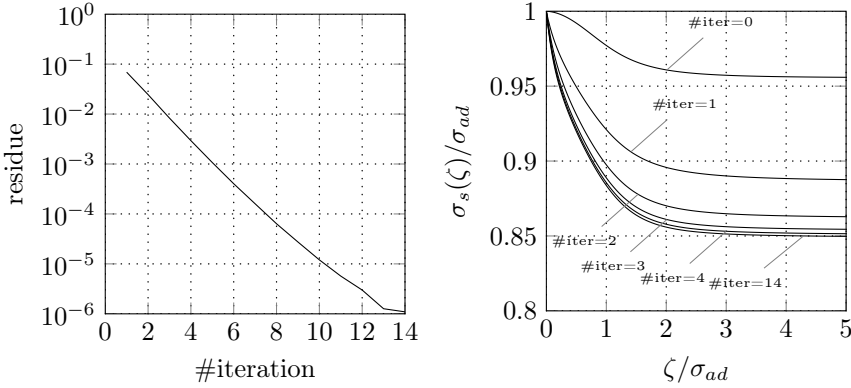


Figure 4.4: Convergence analysis.

and downstream of the device (see the distribution of  $v/U_\infty$  for  $\zeta/\sigma_{ad} = -2$  and  $\zeta/\sigma_{ad} = 2$ ). Instead, in the forepart of the hub ( $\zeta/\sigma_{ad} = -0.4$ ) the radial velocity is significant and, in more detail, it is positive near the hub and negative otherwise. This trend can be readily justified. In fact, the incoming fluid is carried outward in the spanwise direction by the forepart of the hub thus promoting a positive radial velocity. Conversely, the hub effect reduces as soon as the radius is increased and at a certain radial location the slipstream contraction effect prevails over the streamline divergence, thus giving rise to a negative radial velocity. In the back side of the hub ( $\zeta/\sigma_{ad} = 0.5, \zeta/\sigma_{ad} = 1.0$ ) the radial velocity is throughout negative since, in this region of the space, the hub and the slipstream contraction effects both produce a negative radial velocity. Figure 4.2 also shows that, for  $\zeta/\sigma_{ad} = -2.0$ ,  $u/U_\infty$  is everywhere almost equal to the free stream velocity  $U_\infty$ , while, for  $\zeta/\sigma_{ad} = -0.5$ , both the hub and the actuator disk induce an increase of the axial velocity. At last, the typical propeller jet can be recognized for  $\zeta/\sigma_{ad} \geq 0$ . Figure 4.3 shows the tangential velocity radial distribution. In accordance with the angular momentum equation (4.5), the data point out that, due to the non-zero value of the load at the hub  $\mathcal{H}(0) \neq 0$ ,  $w$  has to approach  $\infty$  moving towards the  $\zeta$  axis. Finally, Figure 4.3 also presents the distribution of the wall pressure coefficient defined as  $C_{p,w} = (p - p_\infty)/\frac{1}{2}\rho U_\infty^2$ . The  $C_{p,w}$  jump at the disk station  $\zeta/\sigma_{ad} = 0$  is obviously due to the non-zero value of the load at the hub  $\mathcal{H}(0) \neq 0$ , i.e.  $b_0 \neq 0$ .

Figure 4.4 shows the convergence history (left) and the slipstream  $\sigma_s(\zeta)$

$C_{T,rot}$	$C_{T,hub}$	$C_T$	$C_P$	$\eta$
1.586	7.902E-2	1.665	2.287	0.728

Table 4.3: Semi-analytical actuator disk with finite hub and without slipstream rotation: performance coefficients.

at different iterations (right). In the figure, the residue defined as the absolute value of the difference between two successive slipstream radii evaluated at  $\zeta = 5\sigma_{ad}$ , normalized with  $\sigma_{ad}$ . As anticipated in §4.2.2, an under-relaxation technique has to be adopted in order to preserve the stability of the method. In particular, a under-relaxation factor  $\omega_{rf} = 0.5$  has been employed with success in all calculations. Figure 4.4 right also shows that the nonlinear effects produce a significant contraction of the slipstream radius that at  $\zeta/\sigma_{ad} = 5$  is reduced to about 85% of the propeller radius.

The special case of a rotor without slipstream rotation can successfully be employed to model a contra-rotating rotor pair or a turbomachinery stage both with  $w(\zeta, \sigma) = 0$  in the wake. In this case, the tangential component of the vorticity can be directly related to the load radial distribution through the relation  $\omega_\theta(\zeta, \sigma)/\sigma = d\mathcal{H}/d\Psi$  (Conway 1998) that, with the help of equation (4.18), reduces to:

$$\frac{\omega_\theta(\zeta, \sigma)}{\sigma} = -\frac{U_\infty}{\sigma_{ad}^2} \sum_{m=1}^M mb_m \left( \frac{\Psi}{\Psi_{\sigma_{ad}}} \right)^{m-1}, \quad (4.36)$$

to be used in the iterative procedure instead of (4.19). Furthermore, the only condition to be met when assigning the load distribution is equation (4.34a). For the sake of brevity, in the following section, only the case of a propeller without slipstream rotation will be presented. All data have been obtained with the semi-analytical method detailed in section 4.2 which is also validated through a comparison with the results obtained with a CFD actuator disk technique.

## 4.4 Error analysis and comparison with CFD

In the following section the results obtained with the semi-analytical actuator disk method are analysed and validated. To this end, consider an actuator disk without slipstream rotation and with the following values for the load distribution parameters defined in §4.2.2:  $M = 3$ ,  $b_0 = 1$ ,  $b_1 = 1$ ,

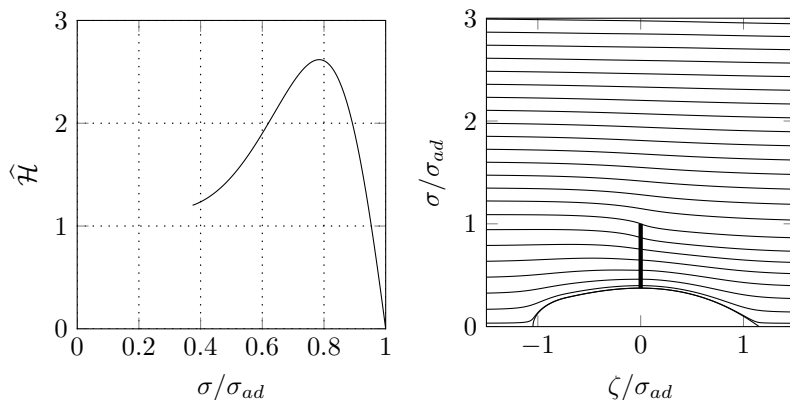


Figure 4.5: Nonlinear actuator disk with finite hub (SAHP-5): load radial distribution (left) and streamlines (right).

$b_2 = 7$  and  $b_3 = -9$ . Table 4.3 lists the performance coefficients related to this configuration, while the load radial distribution and the streamlines are reported in Figure 4.5. In order to properly validate the results, a detailed analysis of the numerical errors associated to the semi-analytical procedure described in §4.2.2 is carried out in §4.4.1. The error analysis allows to obtain a set of reference numerical data which can be compared with the results of a CFD actuator disk. As mentioned in the introduction, the latter is a widely employed analysis tool that provides the solution of the discretised flow equations by simulating the rotor effects with a body force distribution in the actuator disk plane. Once more, the so-called “fan boundary condition”, implemented in the commercial CFD code ANSYS Fluent, is used to model the rotor energy transfer. In particular, a mesh dependence analysis is first carried out in §4.4.2 and finally, in §4.4.3, the results of the semi-analytical and CFD actuator disk methods are compared one another.

#### 4.4.1 The semi-analytical actuator disk with finite hub: error analysis

The solution procedure described in §4.2.2 consists of both analytical and numerical steps. In order to gain some confidence on the accuracy of the present method, it is important to quantify the impact of the numerical errors associated to the solution procedure onto the quality of the results.

<i>#case</i>	$n_z$	$n_{zs}$	$n_{rs}$	$M_p$	$b_0$	$b_1$	$b_2$	$b_3$
SAHP-1	101	51	51	200	1.0	1.0	7.0	-9.0
SAHP-2	201	101	101	400	1.0	1.0	7.0	-9.0
SAHP-3	301	151	151	600	1.0	1.0	7.0	-9.0
SAHP-4	401	201	201	800	1.0	1.0	7.0	-9.0
SAHP-5	501	251	251	1000	1.0	1.0	7.0	-9.0

Table 4.4: Nonlinear actuator disk with finite hub: numerical parameters.

<i>#case</i>	Performance coefficients relative error			Axial velocity $L_2$ discrete norm of the error		
	$C_T$	$C_P$	$\eta$	$u _{\zeta=-1}$	$u _{\zeta=1}$	$u _{\zeta=2}$
SAHP-1	1.869E-3	3.344E-3	1.470E-3	3.136E-4	1.460E-3	1.483E-3
SAHP-2	3.242E-4	4.748E-4	1.505E-4	4.755E-5	2.077E-4	2.141E-4
SAHP-3	8.150E-5	8.997E-5	8.463E-6	9.843E-6	3.968E-5	4.117E-5
SAHP-4	2.145E-5	1.665E-5	4.809E-6	3.397E-6	8.792E-6	8.692E-6
SAHP-5	0	0	0	0	0	0

Table 4.5: Nonlinear actuator disk with finite hub: error analysis.

To this end, the effects of the four parameters  $n_z$ ,  $n_{zs}$ ,  $n_{rs}$  and  $M_p$ , introduced in §4.2.2, is investigated and discussed. In particular, for the sake of conciseness, these parameters are made to grow all together in a five-levels range (see Table 4.4). The accuracy of the performance coefficient values and of the velocity fields data is judged on the basis of the distance from the results obtained by the most accurate set (SAHP-5). In Table 4.5, the axial velocity  $L_2$  discrete norm of the error and the relative errors of the performance coefficients are listed, where case SAHP-5 is assumed as reference. As it can be easily inferred from Table 4.5, a good accuracy level is already reached with the lowest value of the analysed numerical parameters, thus demonstrating the possibility to obtain an accurate solution in a very short computational time.

# case	# cells inner domain	# cells full-size domain
CFDHP-1	41301	106092
CFDHP-2	167633	336805
CFDHP-3	675417	1056225

Table 4.6: Characteristics of the mesh employed in the CFD grid dependence analysis.

#case	Axial velocity $L_2$ discrete norm of the error			Radial velocity $L_2$ discrete norm of the error		
	$u _{\zeta=-1}$	$u _{\zeta=1}$	$u _{\zeta=2}$	$v _{\zeta=-1}$	$v _{\zeta=1}$	$v _{\zeta=2}$
	CFDHP-1	6.296E-4	2.446E-2	2.981E-2	7.356E-4	1.618E-3
CFDHP-2	1.489E-4	8.520E-3	1.064E-2	2.035E-4	5.184E-4	1.072E-4
CFDHP-3	0	0	0	0	0	0

Table 4.7: CFD actuator disk: mesh dependence analysis.

	$\zeta = -1.0$	$\zeta = 1.0$	$\zeta = 2.0$
radial velocity	3.130E-5	3.180E-4	7.696E-5
axial velocity	2.141E-4	6.124E-3	7.566E-3
wall pressure coefficient	4.199E-3		

Table 4.8: Comparison between semi-analytical (SAHP-5) and CFD (CFDHP-3) actuator disk:  $L_2$  discrete norm of the error.

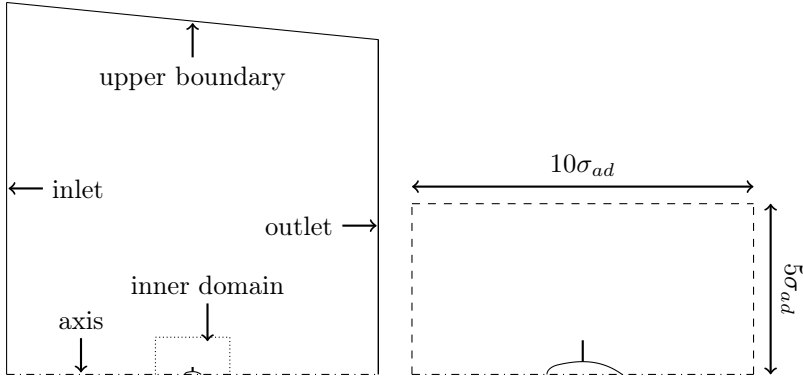


Figure 4.6: Computational domain. Left: full size; right: inner domain.

#### 4.4.2 The CFD actuator disk with finite hub: mesh dependence analysis

Figure 4.6 shows the two dimensional computational domain adopted in the CFD actuator disk simulations. The inlet boundary, which is  $25\sigma_{ad}$  far from the actuator disk plane, is treated as an uniform velocity boundary condition. At the outlet boundary, which is also placed at  $25\sigma_{ad}$  far from the rotor, a uniform pressure  $p_\infty$  is imposed. Obviously, at the hub section profile an inviscid wall boundary condition is employed, while the load radial distribution obtained in the reference case (SAHP-5) of the semi-analytical method is prescribed at the rotor plane through the aforementioned “fan boundary condition”. Finally, the upper edge, whose midpoint is located at  $45\sigma_{ad}$  far from the axis, is also treated as a uniform pressure outlet boundary condition. A body-fitted structured multi-block mesh is adopted. Different mesh densities in different parts of the computational domain were adopted to save computational resources. More in detail, a finer grid spacing is setted in the so-called inner domain (see Figure 4.6 right), while the mesh density is reduced moving towards the external edges of the domain. Spatial discretisation is performed with a second order scheme, while time integration is carried out with a pressure correction method. The error analysis is conducted by increasing the inner domain mesh density on a three-level range as detailed in Table 4.6. Finally, Table 4.7 reports the  $L_2$

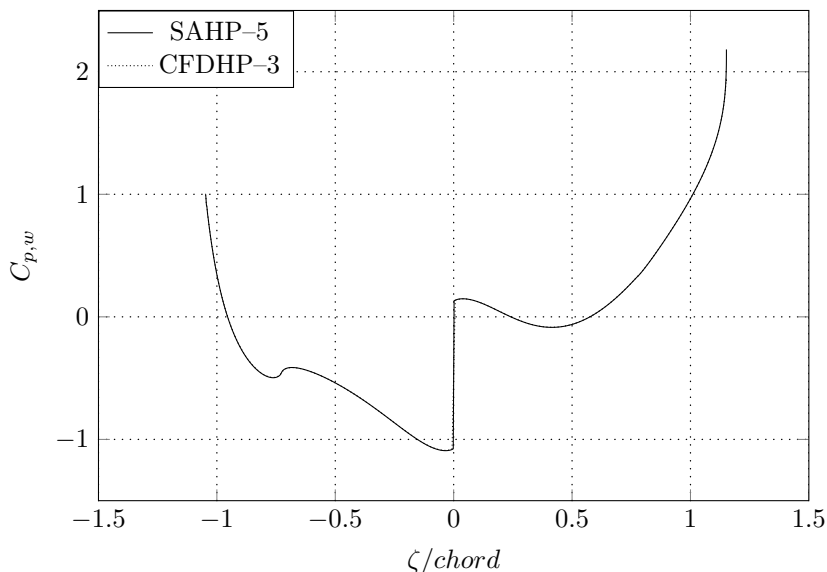


Figure 4.7: Comparison between the wall pressure coefficient profiles obtained with the semi-analytical (SAHP-5) and CFD (CFDHP-3) actuator disk methods.

discrete norm of the error in the axial and radial velocities by assuming the fine grid level results (CFDHP-3) as reference.

#### 4.4.3 Semi-analytical and CFD actuator disk with finite hub: comparison of the results

As reported in Chapter 1, the semi-analytical actuator disk with a finite hub procedure could be validated at downstream infinity by means of asymptotic relations. However, in the present chapter, a validation is obtained at all points of the computational domain and not only at downstream infinity. In particular, in order to validate the semi-analytical method, the results of case SAHP-5 have been compared with those obtained with the finest mesh (CFDHP-3) through the CFD actuator disk described in the previous section. The comparisons between the velocity profiles at different axial stations and the  $C_{p,w}$  distribution obtained with the two methods are reported Figures 4.8 and 4.7, respectively. In all cases the agreement is excellent

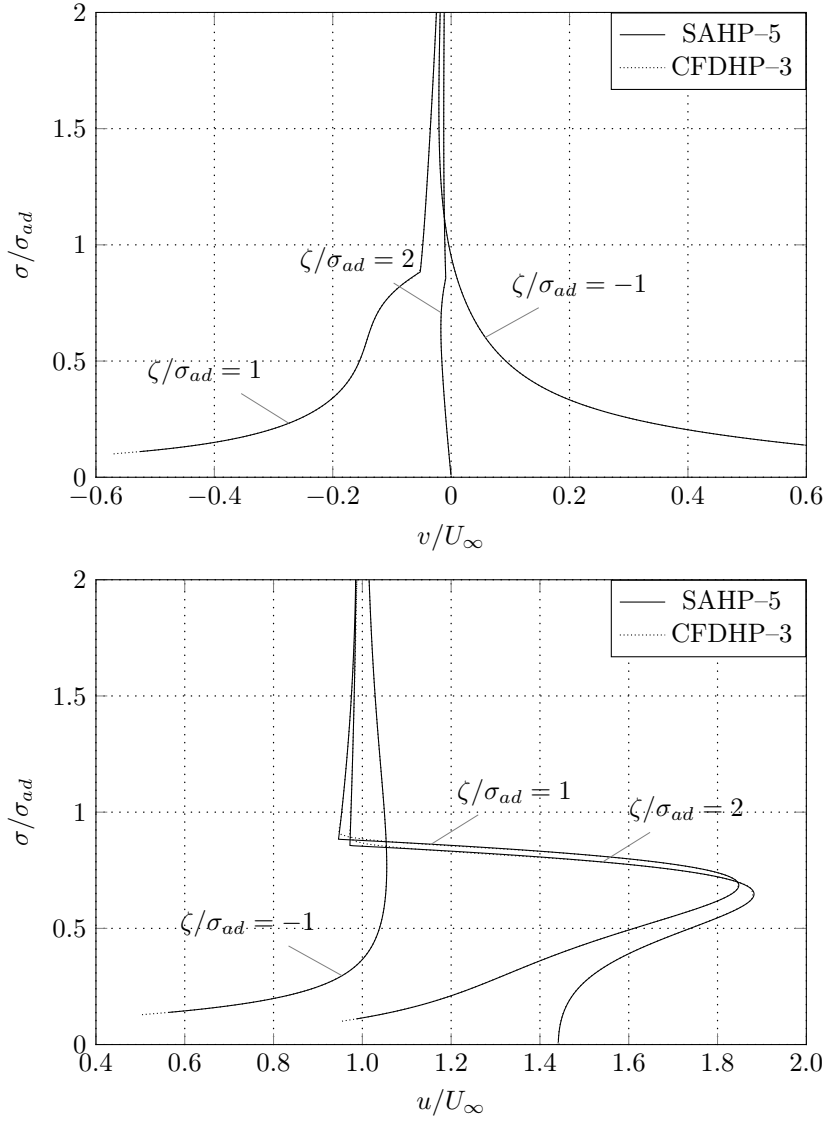


Figure 4.8: Radial (top) and axial (bottom) velocity profiles obtained with the semi-analytical (SAHP-5) and CFD (CFDHP-3) actuator disk methods.

as also witnessed by the errors reported in Table 4.8, which quantifies the differences between the results of the two models.



## CHAPTER 5

---

### CONCLUSIONS

---

In this thesis an extension to ducted rotors of the nonlinear and semi-analytical actuator disk theory of Conway (1998) has been presented. In particular, an exact solution for the inviscid axisymmetric flow generated by a heavily loaded ducted rotor and a cost-effective semi-analytical solution procedure of the resulting equation are detailed. The solution being exact, the proper shape of the slipstream, whether converging or diverging, is naturally accounted for, even for heavy loads. The solution procedure can handle rotor wake rotation, radial load distributions, and ducts of general shape. Furthermore, the method preserves the fully coupled nature of the solution, duly taking into account the nonlinear mutual interaction between the duct and the rotor. The solution is expressed as a triple integral over the radial and axial coordinates and over the allowed values of the separation constant of the eigensolutions of the Laplace equation in cylindrical coordinates. Two of these integrals are exactly evaluated, while the integration in the axial direction is performed through numerical quadrature, with an extremely reduced computational cost. The procedure has been validated at downstream infinity, i.e.  $\zeta \rightarrow +\infty$ , with the help of asymptotic relations.

On the engineering side, the method has been employed to investigate the characteristics of the flow around both wind turbines and marine propeller.

In the first case, the obtained results clearly show that the ducted wind

turbine can swallow a higher mass flow rate than an open turbine with the same rotor load. Consequently, the ducted turbine achieves a higher value of the extracted power.

The analysis of the results about ducted propellers have shown that, in order to increase the device efficiency for prescribed propulsive thrust, the duct must be properly designed. In more detail, according to the linearised theory, the coupling between the duct and the rotor has to return a lower rotor load, i.e.  $\mathbf{T}_{duct}$  and  $\mathbf{T}_{rot}$  need to have the same direction. Furthermore, the beneficial effect of the duct is shown to be particularly significant for heavily loaded propellers. Finally, the method has been successfully employed to properly match the duct and the rotor, the optimal matching being based on the analysis of the local flow characteristics occurring in the duct leading edge region.

As a matter of fact, the availability of a numerical model which could properly handle a prescribed hub geometry is mandatory for all those applications characterised by a appreciable value of the hub/propeller radii ratio, as frequently encountered in the marine propeller field. For this reason, an extension of the semi-analytical actuator disk method capable to deal with finite and axisymmetric hubs of general shape has also been presented and deeply discussed.

To further validate the method, emphasis has been given to the comparison of the results of the semi-analytical procedure with a CFD actuator disk method commonly employed to simulate the flow around open and ducted rotors. The latter method is based on the introduction of an actuator disk model, describing the effects of the rotor through radial profiles of blade forces distributed over a disk surface, in a CFD package. In order to properly compare the results of the two methods, a thorough error analysis has been carried out and a set of reference numerical data, providing the inviscid axisymmetric velocity and pressure field distributions, has been generated with controlled accuracy. Evidence has been given of the excellent agreement between the results of the two methods. Owing to the in-depth analysis of the error generated by the semi-analytical method and to the exactness of the solution in its implicit form, the collected data are well-suited for code-to-code validation of existing or newly developed computational methods.

Finally, thanks to its extremely reduced computational cost the semi-analytical method can easily be integrated into design systems based on the repeated analysis scheme of hierarchical type.

# APPENDIX A

---

## THE GREEN FUNCTION OF THE LINEAR ELLIPTIC OPERATOR $L_{(\zeta, \sigma)}$

---

As proven in Chapter 1 the differential problem for the steady, incompressible and inviscid flow around an actuator disk reads:

$$L_{(\zeta, \sigma)} \left( \frac{\Psi}{\sigma} \right) = \sigma \left( \frac{\partial^2}{\partial \sigma^2} + \frac{1}{\sigma} \frac{\partial}{\partial \sigma} - \frac{1}{\sigma^2} + \frac{\partial^2}{\partial \zeta^2} \right) \frac{\Psi}{\sigma} = \epsilon_s \frac{\Omega^2 \sigma^2 - \mathcal{H} \, d\mathcal{H}}{\Omega^2} \frac{d\Psi}{d\mathcal{H}}, \quad (\text{A.1})$$

$$\frac{1}{\sigma} \frac{\partial \Psi}{\partial \sigma} \rightarrow U_\infty, \quad \frac{\partial \Psi}{\partial \zeta} \rightarrow 0 \quad \text{as } \zeta \rightarrow -\infty \quad \text{or } \sigma \rightarrow \infty, \quad (\text{A.2a})$$

$$\frac{\partial \Psi}{\partial \zeta} \rightarrow 0 \quad \text{as } \zeta \rightarrow +\infty, \quad (\text{A.2b})$$

where  $\epsilon_s = 1$  inside the slipstream and  $\epsilon_s = 0$  otherwise. The objective of this appendix is to obtain the Green function  $G(\zeta, \sigma; z, r)$  for the linear elliptic operator  $L_{(\zeta, \sigma)}$  appearing at the left-hand side of equation (A.1). The first to attain this task was Wu (1962) who, however, omitted the derivation of  $G$ . A more detailed and thorough description of the issue can also be found in Breslin and Andersen (1994).

First of all, it is convenient to introduce the following dimensionless

variables:

$$\hat{\sigma} = \frac{\sigma}{\sigma_{ad}}, \quad \hat{\zeta} = \frac{\zeta}{\sigma_{ad}}, \quad \hat{\mathbf{u}} = \frac{1}{U_\infty} \mathbf{u},$$

$$\hat{\Psi} = \frac{\Psi}{U_\infty \sigma_{ad}^2}, \quad \hat{\mathcal{H}} = \frac{2\mathcal{H}}{U_\infty^2}, \quad \lambda = \frac{\Omega \sigma_{ad}}{U_\infty}.$$

Making use of the above quantities, the dimensionless form of equations (A.1) and (A.2) can be written as

$$L_{(\hat{\zeta}, \hat{\sigma})} \left( \frac{\hat{\Psi}}{\hat{\sigma}} \right) = \hat{\sigma} \left( \frac{\partial^2}{\partial \hat{\sigma}^2} + \frac{1}{\hat{\sigma}} \frac{\partial}{\partial \hat{\sigma}} - \frac{1}{\hat{\sigma}^2} + \frac{\partial^2}{\partial \hat{\zeta}^2} \right) \frac{\hat{\Psi}}{\hat{\sigma}} = \epsilon_s \frac{1}{2} \left( \hat{\sigma}^2 - \frac{\hat{\mathcal{H}}}{2\lambda^2} \right) \frac{d\hat{\mathcal{H}}}{d\hat{\Psi}}, \quad (\text{A.3})$$

$$\frac{1}{\hat{\sigma}} \frac{\partial \hat{\Psi}}{\partial \hat{\sigma}} \rightarrow 1, \quad \frac{\partial \hat{\Psi}}{\partial \hat{\zeta}} \rightarrow 0 \quad \text{as } \hat{\zeta} \rightarrow -\infty \quad \text{or } \hat{\sigma} \rightarrow \infty, \quad (\text{A.4a})$$

$$\frac{\partial \hat{\Psi}}{\partial \hat{\zeta}} \rightarrow 0 \quad \text{as } \hat{\zeta} \rightarrow +\infty. \quad (\text{A.4b})$$

It is further convenient to introduce the perturbation stream function  $\psi$  and its dimensionless form  $\hat{\psi}$  defined as

$$\Psi = \frac{U_\infty \sigma^2}{s} + \psi, \quad \hat{\Psi} = \frac{1}{2} \hat{\sigma}^2 + \hat{\psi}$$

Finally, by substituting the above equations in (A.3) and (A.4), it returns

$$L_{(\hat{\zeta}, \hat{\sigma})} \left( \frac{\hat{\psi}}{\hat{\sigma}} \right) = \hat{\sigma} \left( \frac{\partial^2}{\partial \hat{\sigma}^2} + \frac{1}{\hat{\sigma}} \frac{\partial}{\partial \hat{\sigma}} - \frac{1}{\hat{\sigma}^2} + \frac{\partial^2}{\partial \hat{\zeta}^2} \right) \frac{\hat{\psi}}{\hat{\sigma}} = -g(\hat{\zeta}, \hat{\sigma}) \quad (\text{A.5})$$

$$\frac{1}{\hat{\sigma}} \frac{\partial \hat{\psi}}{\partial \hat{\sigma}} \rightarrow 0, \quad \frac{\partial \hat{\psi}}{\partial \hat{\zeta}} \rightarrow 0 \quad \text{as } \hat{\zeta} \rightarrow -\infty \quad \text{or } \hat{\sigma} \rightarrow \infty, \quad (\text{A.6a})$$

$$\frac{\partial \hat{\psi}}{\partial \hat{\zeta}} \rightarrow 0 \quad \text{as } \hat{\zeta} \rightarrow +\infty, \quad (\text{A.6b})$$

where

$$g(\hat{\zeta}, \hat{\sigma}) = -\epsilon_s \frac{1}{2} \left( \hat{\sigma}^2 - \frac{\hat{\mathcal{H}}}{2\lambda^2} \right) \frac{d\hat{\mathcal{H}}}{d\hat{\Psi}}.$$

Note that the boundary conditions are now homogeneous.

The Green function  $G(\widehat{\zeta}, \widehat{\sigma}; z, r)$  of the linear operator  $L_{(\widehat{\zeta}, \widehat{\sigma})}$ , which is applied to the function  $\widehat{\psi}(\widehat{\zeta}, \widehat{\sigma})/\widehat{\sigma}$ , has to satisfy the equation

$$L_{(\widehat{\zeta}, \widehat{\sigma})} \left\{ G(\widehat{\zeta}, \widehat{\sigma}; z, r) \right\} = -\delta(\widehat{\sigma} - r)\delta(\widehat{\zeta} - z), \quad (\text{A.7})$$

and the same boundary conditions of  $\widehat{\psi}/\widehat{\sigma}$ . In the above equation  $\delta$  is the Dirac delta function. Assuming that the second Green's identity for unbounded domain can be applied to the functions  $\widehat{\psi}/\widehat{\sigma}$  and  $G$ <sup>1</sup>, it can be easily found that

$$\int_{-\infty}^{+\infty} \int_0^{+\infty} \left[ G \nabla^2 \left( \frac{\widehat{\psi}}{r} \right) - \frac{\widehat{\psi}}{r} \nabla^2 G \right] r \, dr dz = 0. \quad (\text{A.8})$$

From equations (A.5) and (A.7) the Laplacian of  $\widehat{\psi}/\sigma$  and  $G$  can be written as

$$\nabla^2 \left( \frac{\widehat{\psi}}{\widehat{\sigma}} \right) = \frac{\widehat{\psi}}{\widehat{\sigma}^3} - \frac{g(\widehat{\zeta}, \widehat{\sigma})}{\widehat{\sigma}}, \quad \nabla^2 G = \frac{G}{\widehat{\sigma}^2} - \frac{\delta(\widehat{\sigma} - r)\delta(\widehat{\zeta} - z)}{\widehat{\sigma}},$$

respectively. Then, substituting the above equations in (A.8) gives

$$\begin{aligned} & \int_{-\infty}^{+\infty} \int_0^{+\infty} \left[ G \nabla^2 \left( \frac{\widehat{\psi}}{r} \right) - \frac{\widehat{\psi}}{r} \nabla^2 G \right] r \, dr dz = \\ & \int_{-\infty}^{+\infty} \int_0^{+\infty} \left[ G \left( \frac{\widehat{\psi}}{r^3} - \frac{g(z, r, \widehat{\psi})}{r} \right) - \frac{\widehat{\psi}}{r} \nabla^2 \left( \frac{G}{r^2} - \frac{\delta(\widehat{\sigma} - r)\delta(\widehat{\zeta} - z)}{r} \right) \right] r \, dr dz = \\ & \int_{-\infty}^{+\infty} \int_0^{+\infty} \frac{\widehat{\psi}}{r} \delta(\widehat{\sigma} - r)\delta(\widehat{\zeta} - z) \, dr dz - \int_{-\infty}^{+\infty} dz \int_0^{+\infty} G g \, dr = 0. \end{aligned}$$

Finally, applying the shifting properties of the Dirac  $\delta$  function, it yields

$$\widehat{\psi}(\widehat{\zeta}, \widehat{\sigma}) = \widehat{\sigma} \int_{-\infty}^{+\infty} dz \int_0^{+\infty} G(\widehat{\zeta}, \widehat{\sigma}; z, r) g(z, r) \, dr. \quad (\text{A.9})$$

The derivation of  $G$  can be carried out by employing the Hankel transform which is defined as (L. C. Andrews and Shivamoggi 1988)

$$\widetilde{F}_\nu(s) = \int_0^\infty r f(r) J_\nu(sr) \, dr, \quad (\text{A.10})$$

---

<sup>1</sup>Several assumptions are needed to apply Green's identities to bounded and unbounded domains. A detailed description of these hypothesis can be found in Tikhonov and Samarskii (1990) Chapter IV and Rubinstein (1998) Chapter 12.

while, the corresponding inversion formula takes the form

$$f(r) = \int_0^\infty s \tilde{F}_\nu(s) J_\nu(sr) ds, \quad (\text{A.11})$$

where  $J_\nu$  is the Bessel function of the first kind and order  $\nu$ . Multiplying equation (A.7) by  $\hat{\sigma} J_1(s\hat{\sigma})$  and integrating, it returns

$$\begin{aligned} & \int_0^\infty \frac{\partial^2 G}{\partial \hat{\sigma}^2} \hat{\sigma} J_1(s\hat{\sigma}) d\hat{\sigma} + \int_0^\infty \frac{\partial G}{\partial \hat{\sigma}} J_1(s\hat{\sigma}) d\hat{\sigma} - \int_0^\infty \frac{G}{\hat{\sigma}} J_1(s\hat{\sigma}) d\hat{\sigma} + \\ & \frac{d^2 \tilde{G}_1}{d\hat{z}^2} = - \int_0^\infty \delta(\hat{\sigma} - r) \delta(\hat{\zeta} - z) J_1(s\hat{\sigma}) d\hat{\sigma}. \end{aligned} \quad (\text{A.12})$$

Making use of the shifting properties of the Dirac  $\delta$  function, the right-hand side of the above equation becomes  $-J_1(sr) \delta(\hat{\zeta} - z)$ . Then, applying the change of variable  $\bar{\sigma} = s\hat{\sigma}$ , equation (A.12) reads

$$\begin{aligned} & \int_0^\infty \frac{\partial^2 G}{\partial \bar{\sigma}^2} \bar{\sigma} J_1(\bar{\sigma}) d\bar{\sigma} + \int_0^\infty \frac{\partial G}{\partial \bar{\sigma}} J_1(\bar{\sigma}) d\bar{\sigma} - \int_0^\infty \frac{G}{\bar{\sigma}} J_1(\bar{\sigma}) d\bar{\sigma} + \frac{d^2 \tilde{G}_1}{d\hat{z}^2} = \\ & - J_1(sr) \delta(\hat{\zeta} - z). \end{aligned} \quad (\text{A.13})$$

Thanks to the characteristics of the behaviour of  $G$  at infinity, the integration by parts of the first integral in equation (A.13) yields

$$- \int_0^\infty \frac{\partial G}{\partial \bar{\sigma}} \bar{\sigma} \frac{dJ_1}{d\bar{\sigma}} d\bar{\sigma} - \int_0^\infty \frac{G}{\bar{\sigma}} J_1(\bar{\sigma}) d\bar{\sigma} + \frac{d^2 \tilde{G}_1}{d\hat{z}^2} = -J_1(sr) \delta(\hat{\zeta} - z).$$

Once more, the integration by parts of the first term in the right-hand side of the above equation returns

$$\int_0^\infty \frac{1}{\bar{\sigma}} \left[ \bar{\sigma}^2 \frac{d^2 J_1}{d\bar{\sigma}^2} + \bar{\sigma} \frac{dJ_1}{d\bar{\sigma}} - J_1(\bar{\sigma}) \right] G d\bar{\sigma} + \frac{d^2 \tilde{G}_1}{d\hat{z}^2} = -J_1(sr) \delta(\hat{\zeta} - z). \quad (\text{A.14})$$

The integral appearing in the left-hand side of the equation (A.14) can be elaborated through the Bessel's differential equation

$$x^2 \frac{d^2 y}{dx^2} + x \frac{dy}{dx} + (x^2 - \nu^2) y = 0 \quad (\text{A.15})$$

whose solution are the Bessel function of the first, second and third kind. In equation (A.15),  $\nu$  is an arbitrary complex number representing the order of the related Bessel function. From (A.15) with  $\nu = 1$ , the following equation holds:

$$\bar{\sigma}^2 \frac{d^2 J_1}{d\bar{\sigma}^2} + \bar{\sigma} \frac{dJ_1}{d\bar{\sigma}} - J_1(\bar{\sigma}) = -\bar{\sigma}^2 J_1(\bar{\sigma}).$$

Making use of the previous equation, (A.14) can be cast in the form

$$\int_0^\infty \frac{1}{\hat{\sigma}} \left[ -s^2 \hat{\sigma}^2 J_1(s\hat{\sigma}) \right] G d\hat{\sigma} + \frac{d^2 \tilde{G}_1}{d\hat{z}^2} = -J_1(sr) \delta(\hat{\zeta} - z) \quad (\text{A.16})$$

which, with the help of the Hankel transform (A.10), becomes

$$\frac{d^2 \tilde{G}_1}{d\hat{z}^2} - s^2 \tilde{G}_1 = -J_1(sr) \delta(\hat{\zeta} - z). \quad (\text{A.17})$$

To complete the formulation of the differential problem, two boundary conditions have to be associated to the above equation. First of all,  $\tilde{G}_1$  has to be a continuous function at  $\hat{\zeta} = z$  thus obtaining

$$\lim_{\hat{\zeta} \rightarrow z^-} \tilde{G}_1 = \lim_{\hat{\zeta} \rightarrow z^+} \tilde{G}_1, \quad (\text{A.18})$$

which is the first boundary condition. The second one follows from integrating (A.17) over  $\hat{\zeta}$  from  $z - \epsilon$  to  $z + \epsilon$  and passing to the limit as  $\epsilon \rightarrow 0$ , i.e.

$$\lim_{\epsilon \rightarrow 0} \int_{z-\epsilon}^{z+\epsilon} \frac{d^2 \tilde{G}_1}{d\hat{\zeta}^2} d\hat{\zeta} - \lim_{\epsilon \rightarrow 0} \int_{z-\epsilon}^{z+\epsilon} s^2 \tilde{G}_1 d\hat{\zeta} = -J_1(sr) \lim_{\epsilon \rightarrow 0} \int_{z-\epsilon}^{z+\epsilon} \delta(\hat{\zeta} - z) d\hat{\zeta}.$$

By exploiting the Dirac  $\delta$  function properties, the right-hand side of the above equation can be written as  $-J_1(sr)$ , while, from equation (A.18), the second integral at the left-hand side vanishes. Finally, the second boundary condition reads

$$\lim_{\hat{\zeta} \rightarrow z^-} \frac{d\tilde{G}_1}{d\hat{\zeta}} - \lim_{\hat{\zeta} \rightarrow z^+} \frac{d\tilde{G}_1}{d\hat{\zeta}} = -J_1(sr). \quad (\text{A.19})$$

From the definition of the Dirac  $\delta$  function, the right-hand side of equation (A.17) is zero for  $\hat{\zeta} \neq z$ . Then, the solution of the homogeneous equations is

$$\tilde{G} = C_1 e^{-s(\hat{\zeta}-z)} + C_2 e^{s(\hat{\zeta}-z)}.$$

More in particular,  $G$  being regular at infinity, the above equation becomes

$$\begin{cases} \tilde{G} = C_1 e^{-s(\hat{\zeta}-z)} & \hat{\zeta} - z \geq 0, \\ \tilde{G} = C_2 e^{s(\hat{\zeta}-z)} & \hat{\zeta} - z \leq 0. \end{cases}$$

Substituting condition (A.18) in the above equations retruns  $C_1 = C_2$ . Then, condition (A.19) yields  $C_1 = C_2 = J_1(sr)/2s$ . At the end, the solution of the differential problem (A.17)-(A.18)-(A.19) reads

$$\tilde{G}_1 = \frac{J_1(sr)}{2s} e^{-s|\hat{\zeta}-z|}.$$

Finally, making use of the Hankel transform inverse formula (A.11), the Green function of the  $L_{(\hat{\zeta}, \hat{\sigma})}$  can be expressed as

$$G(\hat{\zeta}, \hat{\sigma}; z, r) = \frac{1}{2} \int_0^\infty e^{-s|\hat{\zeta}-z|} J_1(s\hat{\sigma}) J_1(sr) ds.$$

## APPENDIX B

---

### COMPUTATION OF BESSEL-LAPLACE INTEGRALS

---

As stated in Chapter 1 and 4, the solution procedure of the differential problem for the open and ducted actuator disk reduces to evaluate integrals of the Bessel-Laplace kind, which can be expressed as

$$I_{(\xi,\mu,\nu)} = \int_0^\infty e^{-s|\zeta-z|} s^\xi J_\mu(sr) J_\nu(s\sigma) ds, \quad (\text{B.1})$$

where  $\xi$ ,  $\mu$  and  $\nu$  are integers. To accomplish this task, Conway (2000) carried out several recursion relations that can be arranged in three recursion schemes aimed to compute the integrals  $I_{(-(n+1),n+2,1)}$ ,  $I_{(-n,n+2,0)}$  and  $I_{(-n,n+2,1)}$  appearing in the Stokes stream function (1.38), axial (1.39) and radial (1.40) velocity expressions, respectively. More in particular, in the first section of this appendix some recurrence relations are obtained and discussed, while in the second section these relations are employed to develop the recursion schemes for  $\Psi$ ,  $u$  and  $v$ . Finally, in the last section some useful analytical solutions for the Bessel-Laplace integrals are provided.

#### B.1 Recurrence relations

First of all, it is convenient to introduce the recurrence relations involving integrals with  $\xi = 0$ . It can be shown that for  $\mu = \nu$  the following equation

holds (Watson 1944):

$$I_{(0,\nu,\nu)} = \frac{Q_{\nu-1/2}(\omega)}{\pi\sqrt{\sigma r}}, \quad (\text{B.2})$$

where  $Q_{\nu-1/2}(\omega)$  is the second kind Legendre function of degree  $\nu - 1/2$  evaluated in

$$\omega = \frac{r^2 + \sigma^2 + (\zeta - z)^2}{2\sigma r}.$$

The Legendre function of half-integer degree can be further related to the complete elliptic integrals  $K(k)$  and  $E(k)$ , whose modulus  $k$  reads

$$k = \sqrt{\frac{4\sigma r}{(r + \sigma)^2 + |\zeta - z|^2}}.$$

More in particular,  $Q_{-1/2}(\omega)$  and  $Q_{1/2}(\omega)$  can be expressed as (Abramowitz and Stegun 1964)

$$Q_{-1/2}(\omega) = kK(k)$$

and

$$Q_{1/2}(\omega) = \frac{2 - k^2}{k}K(k) - \frac{2}{k}E(k),$$

respectively. Making use of the above equations, the Legendre functions of higher half-integer degree can be computed by applying the recurrence relation of Hobson (1896)

$$Q_{n+1}(\omega) = \frac{2n + 1}{n + 1}\omega Q_n(\omega) - \frac{n}{n + 1}Q_{n-1}(\omega). \quad (\text{B.3})$$

With  $n = \nu - 1$ , the Hobson's relation can be written as

$$Q_{\nu-1/2}(\omega) = \frac{4(\nu - 1)}{2\nu - 1}\omega Q_{\nu-3/2}(\omega) - \frac{2\nu - 3}{2\nu - 1}Q_{\nu-5/2}(\omega),$$

which, by means of equation (B.2), yields the following recursion (Conway 2000):

$$I_{(0,\nu,\nu)} = \frac{4(\nu - 1)}{2\nu - 1}\omega I_{(0,\nu-1,\nu-1)} - \frac{2\nu - 3}{2\nu - 1}I_{(0,\nu-2,\nu-2)}. \quad (\text{B.4})$$

Turning now to the integrals with  $\xi = 1$  and  $\mu = \nu$ , equation 3.12.15.27 page 287 of Prudnikov, Brychkov, and Marichev (1992) reads

$$I_{(1,\nu,\nu)} = -\frac{|\zeta - z|}{2\pi\sqrt{(r\sigma)^3}} \frac{k^2}{\sqrt{1 - k^2}} Q_{\nu-1/2}^1(\omega) \quad (\text{B.5})$$

where  $Q_{\nu-1/2}^1(\omega)$  is the second kind associated Legendre function of order 1 and degree  $\nu - 1/2$ . The latter can be reduced to Legendre functions by means of recurrence 8.5.1 page 333 of Abramowitz and Stegun (1964):

$$Q_n^{i+1}(\omega) = \frac{1}{\sqrt{\omega^2 - 1}} [(n - i)\omega Q_n^i(\omega) - (n + i)Q_{n-1}^i(\omega)]. \quad (\text{B.6})$$

In fact, by setting  $i = 0$  and  $n = \nu - 1/2$  in the above equation and then substituting in (B.5), the following formula can be obtained:

$$I_{(1,\nu,\nu)} = -\frac{|\zeta - z|}{2\pi\sqrt{(r\sigma)^3}} \frac{k^2}{\sqrt{1 - k^2}} \frac{1}{\sqrt{\omega^2 - 1}} \left[ \left( \nu - \frac{1}{2} \right) \omega Q_{\nu-1/2}(\omega) - \left( \nu - \frac{1}{2} Q_{(\nu-1)-1/2}(\omega) \right) \right],$$

which, by means of equation (B.2), returns (Conway 2000)

$$I_{(1,\nu,\nu)} = \frac{|\zeta - z|(2\nu - 1)}{8r\sigma} \frac{k^4}{1 - k^2} (I_{(0,\nu-1,\nu-1)} - \omega I_{(0,\nu,\nu)}). \quad (\text{B.7})$$

The recursion for the integrals with  $\xi = 0$  and  $\mu \neq \nu$  can be derived from the classical Bessel function recurrence relations (Abramowitz and Stegun 1964):

$$J_{n-1}(x) + J_{n+1}(x) = \frac{2n}{x} J_n(x), \quad (\text{B.8})$$

$$J_{n-1}(x) - J_{n+1}(x) = 2J'_n(x). \quad (\text{B.9})$$

The equations

$$J_{\nu-1}(s\sigma) + J_{\nu+1}(s\sigma) = \frac{2\nu}{s\sigma} J_\nu(s\sigma) \quad (\text{B.10})$$

and

$$J_{\nu-1}(sr) + J_{\nu+1}(sr) = \frac{2\nu}{sr} J_\nu(sr)$$

can be simply found by setting  $x = s\sigma$  and  $x = sr$  in (B.8), respectively. Multiplying the first one by  $J_{\nu+1}(sr)$  and the second by  $J_{\nu-1}(s\sigma)$  and subtracting the two equations, the following relation results:

$$J_{\nu+1}(sr)J_\nu(s\sigma) = \frac{s\sigma}{2\nu} [J_{\nu+1}(sr)J_{\nu+1}(s\sigma) - J_{\nu-1}(sr)J_{\nu-1}(s\sigma)] + \frac{\sigma}{r} J_\nu(sr)J_{\nu-1}(s\sigma). \quad (\text{B.11})$$

Finally, the recursion for the Bessel-Laplace integrals

$$I_{(0,\nu+1,\nu)} = \frac{\sigma}{r} I_{(0,\nu,\nu-1)} + \frac{\sigma}{2\nu} (I_{(1,\nu+1,\nu+1)} - I_{(1,\nu-1,\nu-1)}) \quad (\text{B.12})$$

is obtained by integrating between  $s = 0$  and  $s = \infty$  the product of equation (B.11) and  $e^{-s|\zeta-z|}$ . Setting  $x = sr$  and  $n = \mu - 1$  in equation (B.8) gives

$$J_{\mu-2}(sr) + J_{\mu}(sr) = \frac{2(\mu-1)}{sr} J_{\mu-1}(sr).$$

Multiplying the above equation by (B.10), and then integrating the product of the resulting relation and  $e^{-s|\zeta-z|}$  between  $s = 0$  and  $s = \infty$ , returns

$$I_{(0,\mu,\nu)} = -I_{(0,\mu-2,\nu)} + \frac{(\mu-1)\sigma}{\nu r} (I_{(0,\mu-1,\nu+1)} + I_{(0,\mu-1,\nu-1)}). \quad (\text{B.13})$$

Moreover, using equation (B.9) and integration by parts, the following recurrence relation can be obtained:

$$I_{(0,\mu,\nu)} = I_{(0,\mu-2,\nu)} - \frac{2|\zeta-z|}{r} I_{(0,\mu-1,\nu)} + \frac{\sigma}{r} (I_{(0,\mu-1,\nu-1)} - I_{(0,\mu-1,\nu+1)}). \quad (\text{B.14})$$

Combining the last two equations yields

$$\begin{aligned} I_{(0,\mu,\nu)} &= \frac{2(\nu+1)|\zeta-z|}{\sigma(\nu+1-\mu)} I_{(0,\mu,\nu+1)} - \frac{2(\nu+1)r}{\sigma(\nu+1-\mu)} I_{(0,\mu-1,\nu+1)} \\ &\quad + \frac{\nu+1+\mu}{\nu+1-\mu} I_{(0,\mu,\nu+2)} \end{aligned} \quad (\text{B.15})$$

Finally, for  $\xi < 0$ , the recurrence relation

$$I_{(\xi,\mu,\nu)} = \frac{r}{2\xi} (I_{(\xi+1,\mu+1,\nu)} + I_{(\xi+1,\mu-1,\nu)}) \quad (\text{B.16})$$

can be easily obtained from equation (B.8). Obviously, the above equation holds for all cases in which the integral exists.

## B.2 Recursion schemes

As stated in Chapter 1 and 4, the solution procedure of the differential problem for the open and ducted actuator disk reduces to evaluate the integrals

$$I_{(-(n+1),n+2,1)} \quad I_{(-n,n+2,0)} \quad I_{(-n,n+2,1)} \quad n = 0, \dots, N$$

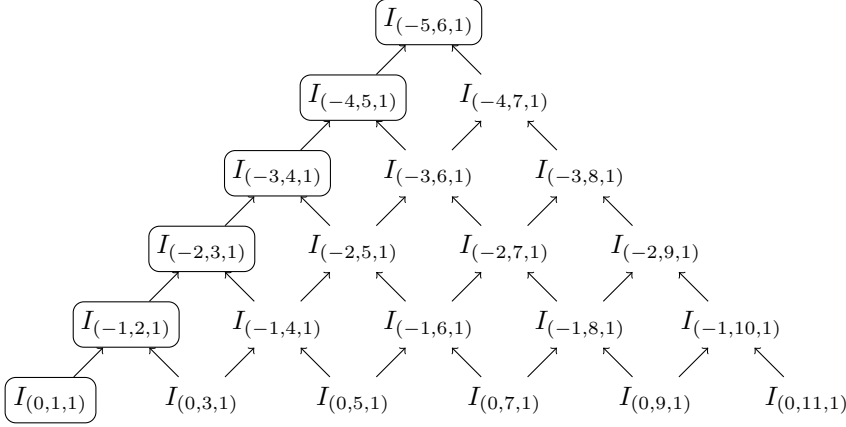


Figure B.1: Computation of the integrals  $I_{-(n+1), n+2, 1}$  through equation (B.16)

which appear in the Stokes stream function, axial and radial velocity expressions, respectively. To accomplish this task, the recursion relations furnished in the previous section can be arranged in three recursion schemes. In particular, the schemes start up by computing the integrals  $I_{(0,0,0)}$ ,  $I_{(0,1,1)}$ ,  $I_{(0,1,0)}$  and  $I_{(1,0,0)}$  whose analytical solutions are provided in the next section. After that, the diagonal entries of

$$[I_{(0,\mu,\nu)}] = \begin{bmatrix} I_{(0,0,0)} & 0 & 0 & 0 & 0 & 0 & \dots \\ I_{(0,1,0)} & I_{(0,1,1)} & 0 & 0 & 0 & 0 & \dots \\ I_{(0,2,0)} & I_{(0,2,1)} & I_{(0,2,2)} & 0 & 0 & 0 & \dots \\ I_{(0,3,0)} & I_{(0,3,1)} & I_{(0,3,2)} & I_{(0,3,3)} & 0 & 0 & \dots \\ I_{(0,4,0)} & I_{(0,4,1)} & I_{(0,4,2)} & I_{(0,4,3)} & I_{(0,4,4)} & 0 & \dots \\ I_{(0,5,0)} & I_{(0,5,1)} & I_{(0,5,2)} & I_{(0,5,3)} & I_{(0,5,4)} & I_{(0,5,4)} & \dots \\ \vdots & \vdots & \vdots & \vdots & \vdots & \vdots & \ddots \end{bmatrix} \quad (\text{B.17})$$

can be computed by applying relation (B.4). More in detail, with  $\omega > 1$ , the Miller's algorithm for downward recurrence is employed (Abramowitz and Stegun 1964). Furthermore, thanks to the knowledge of the diagonal entries of  $[I_{(0,\mu,\nu)}]$ , it is possible to compute the components of the vector

$$[I_{(1,n,n)}] = [I_{(1,0,0)} \quad I_{(1,1,1)} \quad I_{(1,2,2)} \quad I_{(1,3,3)} \quad I_{(1,4,4)} \quad I_{(1,5,5)} \quad \dots]$$

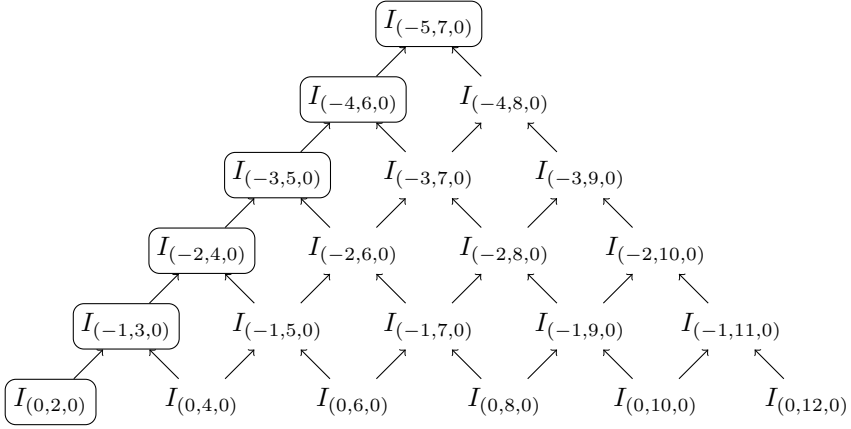


Figure B.2: Computation of the integrals  $I_{(-n, n+2, 0)}$  through equation (B.16)

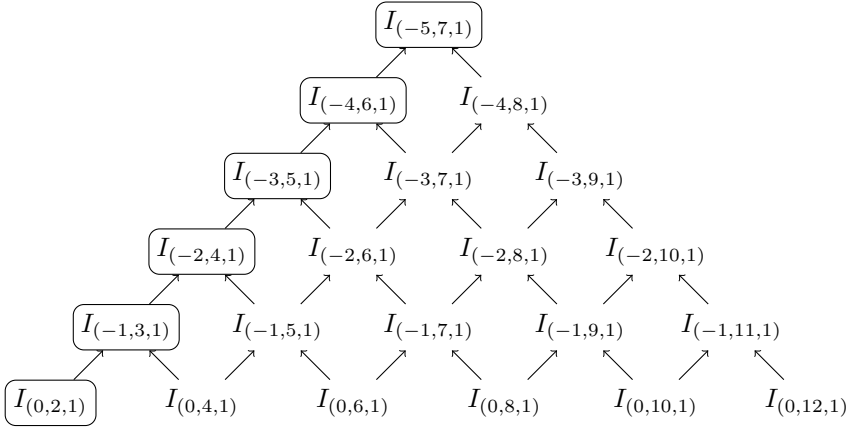


Figure B.3: Computation of the integrals  $I_{(-n, n+2, 1)}$  through equation (B.16)

through equation (B.7). Consequently, recurrence (B.12) can be used to compute the integrals appearing in the subdiagonal of matrix (B.17), while relation (B.15) is successively employed to evaluate all the remaining entries of  $[I_{(0,\mu,\nu)}]$ . Finally, the elements of the first and second column of  $[I_{(0,\mu,\nu)}]$ , i.e.  $I_{(0,n,0)}$  and  $I_{(0,n,1)}$ , can be used to calculate the integrals  $I_{(-(n+1),n+2,1)}$ ,  $I_{(-n,n+2,0)}$  and  $I_{(-n,n+2,1)}$ . More in particular, for  $N = 5$ , Figures B.1, B.2 and B.3 show the computational strategy adopted to evaluate  $I_{(-(n+1),n+2,1)}$ ,  $I_{(-n,n+2,0)}$  and  $I_{(-n,n+2,1)}$ , respectively.

### B.3 Analytical solutions for the Bessel-Laplace integrals

In this section some useful analytical solutions for the Bessel-Laplace integrals are listed. More in particular, the integrals are expressed in terms of complete elliptic integrals  $K(k)$  and  $E(k)$  and Heuman Lambda function  $\Lambda(|\beta|, k)$ , where  $\beta = \arcsin(|\zeta - z|/\sqrt{(\sigma - r)^2 + |\zeta - z|^2})$ .

$$I_{(0,0,0)} = \frac{k}{\pi\sqrt{\sigma r}}K(k)$$

$$I_{(0,1,1)} = \frac{1}{\pi k\sqrt{\sigma r}} \left[ (2 - k^2)K(k) - 2E(k) \right]$$

$$I_{(0,2,2)} = \frac{1}{3\pi k^3\sqrt{\sigma r}} \left[ (4 - k^2)(4 - 3k^2)K(k) - 8(2 - k^2)E(k) \right]$$

$$I_{(0,3,3)} = \frac{1}{15\pi k^5\sqrt{\sigma r}} \left[ (2 - k^2)(128 - 128k^2 + 15k^4)K(k) - 2(128 - 128k^2 + 23k^4)E(k) \right]$$

$$I_{(0,4,4)} = \frac{1}{105\pi k^7\sqrt{\sigma r}} \left[ (6144 - 12288k^2 + 8000k^4 - 1856k^6 + 105k^8)K(k) - 32(2 - k^2)(96 - 96k^2 + 11k^4)E(k) \right]$$

$$I_{(0,1,0)} = \frac{1}{r} \left[ 1 - \frac{|\zeta - z|k}{2\pi\sqrt{\sigma r}} K(k) - \frac{1}{2} \Lambda(|\beta|, k) \right] \quad (\sigma < r)$$

$$I_{(0,1,0)} = \frac{1}{r} \left[ \frac{|\zeta - z|k}{2\pi\sqrt{\sigma r}} K(k) + \frac{1}{2} \Lambda(|\beta|, k) \right] \quad (\sigma > r)$$

$$I_{(0,2,0)} = \frac{4}{\pi k r} \sqrt{\frac{\sigma}{r}} E(k) - \frac{k\sigma}{\pi r^2} \sqrt{\frac{\sigma}{r}} K(k) + \frac{|z|}{r^2} \Lambda(|\beta|, k) - \frac{2|z|}{r^2} \quad (\sigma < r)$$

$$I_{(0,2,0)} = \frac{4}{\pi k r} \sqrt{\frac{\sigma}{r}} E(k) - \frac{k\sigma}{\pi r^2} \sqrt{\frac{\sigma}{r}} K(k) - \frac{|z|}{r^2} \Lambda(|\beta|, k) \quad (\sigma > r)$$

$$I_{(0,2,1)} = \frac{2|z|}{\pi k \sqrt{(\sigma r)^3}} E(k) - \frac{|z|k[(\zeta - z)^2 + 2\sigma^2 + r^2]}{2\pi\sqrt{\sigma^3 r^5}} K(k) - \frac{\sigma}{2r^2} \Lambda(|\beta|, k) + \frac{\sigma}{r^2} \quad (\sigma < r)$$

$$I_{(0,2,1)} = \frac{2|z|}{\pi k \sqrt{(\sigma r)^3}} E(k) - \frac{|z|k[(\zeta - z)^2 + 2\sigma^2 + r^2]}{2\pi\sqrt{\sigma^3 r^5}} K(k) + \frac{\sigma}{2r^2} \Lambda(|\beta|, k) \quad (\sigma > r)$$

$$I_{(0,3,1)} = \frac{2}{\pi k r} \sqrt{\frac{\sigma}{r}} \left[ \frac{4\sigma}{r} - \frac{8(2 - k^2)}{3k^2} + \frac{r}{\sigma} \right] E(k) + \frac{k}{\pi r} \sqrt{\frac{\sigma}{r}} \left[ \frac{2(4 - k^2)(4 - 3k^2)}{3k^4} - \frac{r}{\sigma} \frac{2 - k^2}{k^2} - 2 \left( \frac{\sigma}{r} \right)^2 \right] K(k) + \frac{4\sigma|z|}{r^3} \left( \frac{\Lambda(|\beta|, k)}{2} - 1 \right) \quad (\sigma < r)$$

$$I_{(0,3,1)} = \frac{2}{\pi k r} \sqrt{\frac{\sigma}{r}} \left[ \frac{4\sigma}{r} - \frac{8(2 - k^2)}{3k^2} + \frac{r}{\sigma} \right] E(k) + \frac{k}{\pi r} \sqrt{\frac{\sigma}{r}} \left[ \frac{2(4 - k^2)(4 - 3k^2)}{3k^4} - \frac{r}{\sigma} \frac{2 - k^2}{k^2} - 2 \left( \frac{\sigma}{r} \right)^2 \right] K(k) - \frac{2\sigma|z|}{r^3} \Lambda(|\beta|, k) \quad (\sigma > r)$$

$$\begin{aligned}
 I_{(0,3,2)} &= \frac{2|z|[2r^2 + 5\sigma^2 + 2(\zeta - z)^2]}{3\pi k\sqrt{\sigma^3 r^5}} E(k) \\
 &+ \frac{\sigma|z|}{\pi\sqrt{(\sigma r)^3}} \left\{ \frac{(3k^2 - 4)(4 - k^2)}{3k^3} - \frac{k[(\zeta - z)^2 + 2\sigma^2 + r^2]}{2r^2} \right\} K(k) \\
 &- \frac{\sigma^2}{2r^3} \Lambda(|\beta|, k) + \frac{\sigma^2}{r^3} \quad (\sigma < r)
 \end{aligned}$$

$$\begin{aligned}
 I_{(0,3,2)} &= \frac{2|z|[2r^2 + 5\sigma^2 + 2(\zeta - z)^2]}{3\pi k\sqrt{\sigma^3 r^5}} E(k) \\
 &+ \frac{\sigma|z|}{\pi\sqrt{(\sigma r)^3}} \left\{ \frac{(3k^2 - 4)(4 - k^2)}{3k^3} - \frac{k[(\zeta - z)^2 + 2\sigma^2 + r^2]}{2r^2} \right\} K(k) \\
 &+ \frac{\sigma^2}{2r^3} \Lambda(|\beta|, k) \quad (\sigma > r)
 \end{aligned}$$

$$\begin{aligned}
 I_{(0,4,0)} &= -\frac{k}{3\pi\sigma r^4} \sqrt{\frac{\sigma}{r}} \left\{ -8\sigma^4 + r^4 + 8r^2(\zeta - z)^2 + 4\sigma^2 \left[ r^2 + 8(\zeta - z)^2 \right] \right. \\
 &+ \left. 10(\zeta - z)^4 \right\} K(k) + \frac{8}{3\pi k r^3} \sqrt{\frac{\sigma}{r}} \left[ -4\sigma^2 + 2r^2 + 11(\zeta - z)^2 \right] E(k) \\
 &+ \frac{2|z|(-2 + \Lambda(|\beta|, k))[-3\sigma^2 + r^2 + 2(\zeta - z)^2]}{r^4} \quad (\sigma < r)
 \end{aligned}$$

$$\begin{aligned}
 I_{(0,4,0)} &= -\frac{k}{3\pi\sigma r^4} \sqrt{\frac{\sigma}{r}} \left\{ -8\sigma^4 + r^4 + 8r^2(\zeta - z)^2 + 4\sigma^2 \left[ r^2 + 8(\zeta - z)^2 \right] \right. \\
 &+ \left. 10(\zeta - z)^4 \right\} K(k) + \frac{8}{3\pi k r^3} \sqrt{\frac{\sigma}{r}} \left[ -4\sigma^2 + 2r^2 + 11(\zeta - z)^2 \right] E(k) \\
 &- \frac{2|z|\Lambda(|\beta|, k)[-3\sigma^2 + r^2 + 2(\zeta - z)^2]}{r^4} \quad (\sigma > r)
 \end{aligned}$$

$$I_{(1,0,0)} = \frac{|z|k^3}{4\pi(1 - k^2)\sqrt{(\sigma r)^3}} E(k)$$

$$I_{(1,1,1)} = -\frac{|\zeta - z|k}{4\pi(1 - k^2)\sqrt{(\sigma r)^3}} [2(1 - k^2)K(k) - (2 - k^2)E(k)]$$

$$I_{(1,2,2)} = \frac{|z| [(k^4 - 16k^2 + 16)E(k) - 8(2 - k^2)(1 - k^2)K(k)]}{4\pi k(1 - k^2)\sqrt{(\sigma r)^3}}$$

$$I_{(1,3,3)} = \frac{|z|}{12\pi k^3(1 - k^2)\sqrt{(\sigma r)^3}} \left[ 2(k^2 - 1)(128 - 128k^2 + 27k^4)K(k) - (k^2 - 2)(128 - 128k^2 + 3k^4)E(k) \right]$$

$$I_{(1,4,4)} = \frac{|z|}{20\pi k^5(1 - k^2)\sqrt{(\sigma r)^3}} \left[ -32(k^2 - 1)(k^2 - 2)(32 - 32k^2 + 5k^4)K(k) + (2048 - 4096k^2 + 2496k^4 - 448k^6 + 5k^8)E(k) \right]$$

$$I_{(1,1,0)} = \frac{k}{8\pi(1 - k^2)\sqrt{\sigma^3 r^5}} [4\sigma r(1 - k^2)K(k) + k^2(r^2 - \sigma^2 - |\zeta - z|^2)E(k)]$$

$$I_{(-1,0,1)} = \frac{1}{\pi} \sqrt{\frac{r}{\sigma}} \left[ \frac{1}{2} \left( \frac{\sigma}{r} - \frac{r}{\sigma} \right) kK(k) + \frac{2}{k} E(k) \right] - \frac{\zeta - z}{2\sigma} \Lambda(\beta, k) \quad (\sigma < r)$$

$$I_{(-1,0,1)} = \frac{1}{\pi} \sqrt{\frac{r}{\sigma}} \left[ \frac{1}{2} \left( \frac{\sigma}{r} - \frac{r}{\sigma} \right) kK(k) + \frac{2}{k} E(k) \right] + \frac{\zeta - z}{2\sigma} \Lambda(\beta, k) - \frac{|z|}{\sigma} \quad (\sigma > r)$$

$$I_{(-1,1,1)} = -\frac{|z|}{\pi\sqrt{\sigma r}} \left[ \frac{(\zeta - z)^2 + 2r^2 + 2\sigma^2}{4\sigma r} kK(k) - \frac{1}{k} E(k) \right] + \frac{1}{2} \left[ \frac{|r^2 - \sigma^2|}{2\sigma r} \Lambda(|\beta|, k) + \frac{\sigma}{r} \right] \quad (\sigma < r)$$

$$I_{(-1,1,1)} = -\frac{|z|}{\pi\sqrt{\sigma r}} \left[ \frac{(\zeta - z)^2 + 2r^2 + 2\sigma^2}{4\sigma r} kK(k) - \frac{1}{k} E(k) \right] + \frac{1}{2} \left[ \frac{|r^2 - \sigma^2|}{2\sigma r} \Lambda(|\beta|, k) + \frac{r}{\sigma} \right] \quad (\sigma > r)$$

$$\begin{aligned}
 I_{(-1,2,0)} &= \frac{|z|[(\zeta - z)^2 + 4\sigma^2]k}{4\pi\sqrt{\sigma r^5}}K(k) - \frac{3|z|}{\pi k}\sqrt{\frac{\sigma}{r^3}}E(k) \\
 &\quad - \frac{|r^2 - \sigma^2| + 2(\zeta - z)^2}{4r^2}\Lambda(|\beta|, k) + \frac{2(\zeta - z)^2 - \sigma^2}{2r^2} + \frac{1}{2} \quad (\sigma < r)
 \end{aligned}$$

$$\begin{aligned}
 I_{(-1,2,0)} &= \frac{|z|[(\zeta - z)^2 + 4\sigma^2]k}{4\pi\sqrt{\sigma r^5}}K(k) - \frac{3|z|}{\pi k}\sqrt{\frac{\sigma}{r^3}}E(k) \\
 &\quad - \frac{|r^2 - \sigma^2| - 2(\zeta - z)^2}{4r^2}\Lambda(|\beta|, k) \quad (\sigma < r)
 \end{aligned}$$

$$\begin{aligned}
 I_{(-1,2,1)} &= \frac{k}{2\pi}\sqrt{\frac{\sigma}{r}}\left[\frac{(4 - k^2)(4 - 3k^2)}{3k^4} - \frac{\sigma^2}{r^2}\right]K(k) \\
 &\quad + \frac{1}{2\pi k}\sqrt{\frac{\sigma}{r}}\left[\frac{4\sigma}{r} - \frac{8(2 - k^2)}{3k^2}\right]E(k) \\
 &\quad + \frac{\sigma}{r^2}\left(\frac{(\zeta - z)\Lambda(\beta, k)}{2} - |z|\right) \quad (\sigma < r)
 \end{aligned}$$

$$\begin{aligned}
 I_{(-1,2,1)} &= \frac{k}{2\pi}\sqrt{\frac{\sigma}{r}}\left[\frac{(4 - k^2)(4 - 3k^2)}{3k^4} - \frac{\sigma^2}{r^2}\right]K(k) \\
 &\quad + \frac{1}{2\pi k}\sqrt{\frac{\sigma}{r}}\left[\frac{4\sigma}{r} - \frac{8(2 - k^2)}{3k^2}\right]E(k) \\
 &\quad - \frac{\sigma(\zeta - z)}{2r^2}\Lambda(\beta, k) \quad (\sigma > r)
 \end{aligned}$$

$$\begin{aligned}
 I_{(-2,2,1)} &= \frac{|z|}{12\pi k\sqrt{\sigma r^3}}\left[3r^2 - 15\sigma^2 + \frac{4\sigma r(2 - k^2)}{k^2}\right]E(k) \\
 &\quad + \frac{|z|k}{48\pi\sqrt{\sigma^3 r^5}}\left\{3[(\sigma^2 - r^2)(\zeta - z)^2 + 6\sigma^4 - 2r^2(\sigma^2 + r^2)]\right. \\
 &\quad \left.- 2\sigma^2 r^2\left[\frac{16 - 32k^2 + 19k^4 - 3k^6}{k^4(1 - k^2)}\right]\right\}K(k) \\
 &\quad + \frac{|r^4 - \sigma^4| - 2\sigma^2(|r^2 - \sigma^2| + 2(\zeta - z)^2)}{16\sigma r^2}\Lambda(|\beta|, k) \\
 &\quad + \frac{\sigma(4(\zeta - z)^2 - \sigma^2)}{8r^2} - \frac{\sigma}{4} \quad (\sigma < r)
 \end{aligned}$$

$$\begin{aligned}
 I_{(-2,2,1)} &= \frac{|z|}{12\pi k \sqrt{\sigma r^3}} \left[ 3r^2 - 15\sigma^2 + \frac{4\sigma r(2 - k^2)}{k^2} \right] E(k) \\
 &+ \frac{|z|k}{48\pi \sqrt{\sigma^3 r^5}} \left\{ 3 [(\sigma^2 - r^2)(\zeta - z)^2 + 6\sigma^4 - 2r^2(\sigma^2 + r^2)] \right. \\
 &\quad \left. - 2\sigma^2 r^2 \left[ \frac{16 - 32k^2 + 19k^4 - 3k^6}{k^4(1 - k^2)} \right] \right\} K(k) \\
 &+ \frac{|r^4 - \sigma^4| - 2\sigma^2(|r^2 - \sigma^2| - 2(\zeta - z^2))}{16\sigma r^2} \Lambda(|\beta|, k) + \frac{r^2}{8\sigma} \quad (\sigma > r)
 \end{aligned}$$

---

## BIBLIOGRAPHY

---

- Abdel-Maksoud, M. and H. J. Heinke (2002). “Scale effects on ducted propellers”. In: *Proceedings of the 24th Symposium on Naval Hydrodynamics*. Fukuoka, Japan.
- Abramowitz, M. and I. A. Stegun (1964). *Handbook of Mathematical Functions: With Formulas, Graphs, and Mathematical Tables*. National Bureau of Standards. Applied Mathematics Series, Issue 55.
- Ammara, I., C. Leclerc, and C. Masson (2002). “A viscous three – dimensional differential/actuator-disk method for the aerodynamic analysis of wind farms”. In: *Transactions of the American Society of Mechanical Engineers Journal of Solar Energy Engineering* 124.4, pp. 345–356.
- Anderson, J. D. (2001). *Fundamentals of Aerodynamics*. 3rd. McGraw-Hill.
- Andrews, J. B. and D. E. Cummings (1972). “A design procedure for large-hub propellers”. In: *Journal of Ship Research* 16.3, pp. 167–193.
- Andrews, L. C. and B. K. Shivamoggi (1988). *Integral transforms for engineers and applied mathematicians*. Macmillan publishing company.
- ANSYS (2009). *Fluent 12.0 User’s Guide*.
- Badoe, C., A. B. Phillips, and S. R. Turnock (2012). “Initial numerical propeller rudder interaction studies to assist fuel efficient shipping”. In: *15th Numerical Towing Tank Symposium*. July 10, Cortona, IT.
- Baltazar, J. and J. A. C. Falcão de Campos (2009). “On the modelling of the flow in ducted propellers with a panel method”. In: *Proceedings of the 1st International Symposium on Marine Propulsors*. Vol. 9.
- Basset, A. B. (1888). *A treatise on hydrodynamics*. vol. II. Deighton Bell.

BIBLIOGRAPHY

- Batchelor, G. K. (1967). *An introduction to fluid dynamics*. Cambridge University Press.
- Bontempo, R., M. Cardone, M. Manna, and G. Vorraro (2014). “Ducted propeller flow analysis by means of a generalized actuator disk model”. In: *Energy Procedia* 45C, pp. 1107–1115. ISSN: 1876-6102. DOI: 10.1016/j.egypro.2014.01.116. URL: <http://www.sciencedirect.com/science/article/pii/S1876610214001179>.
- Bontempo, R. and M. Manna (2013). “Solution of the flow over a non-uniform heavily loaded ducted actuator disk”. In: *Journal of Fluid Mechanics* 728, pp. 163–195. ISSN: 1469-7645. DOI: 10.1017/jfm.2013.257. URL: [http://journals.cambridge.org/article\\_S0022112013002577](http://journals.cambridge.org/article_S0022112013002577).
- Breslin, J. P. and P. Andersen (1994). *Hydrodynamics of ship propellers*. Cambridge University Press.
- Broglia, R., G. Dubbioso, D. Durante, and A. Di Mascio (2013). “Simulation of turning circle by CFD: Analysis of different propeller models and their effect on manoeuvring prediction”. In: *Applied Ocean Research* 39, pp. 1–10.
- Calaf, M., C. Meneveau, and J. Meyers (2010). “Large eddy simulation study of fully developed wind-turbine array boundary layers”. In: *Physics of Fluids* 22.
- Caracostas, N. (1978). “Off design performance analysis of ducted propellers”. In: *Proceedings Propellers/Shafting '78 Symposium, SNAME*, pp. 3.1–3.8.
- Carlton, J. (2007). *Marine propellers and propulsion*. 2nd. Butterworth – Heinemann.
- Castellani, F. and A. Vignaroli (2013). “An application of the actuator disc model for wind turbine wakes calculations”. In: *Applied Energy* 101, pp. 432–440.
- Çelik, F., M. Güner, and S. Ekinçi (2010). “An approach to the design of ducted propeller”. In: *Transaction B: Mechanical Engineering, Scientia Iranica* 17.5, pp. 406–417.
- Chaplin, H.R. (1964). *A method for numerical calculation of slipstream contraction of a shrouded impulse disk in the static case with application to other axisymmetric potential flow problems*. Tech. rep. 1857. David Taylor Model Basin.
- Chen, H. C. and S. K. Lee (2003a). “Chimera RANS simulation of propeller-ship interactions including crash-astern conditions”. In: *Proceedings of the Thirteenth International Offshore and Polar Engineering Conference*. Vol. 6. May 25–30, Hononolulu, Hawaii, pp. 334–343.

- (2003b). “Time-domain simulation of propeller-ship interactions under turning conditions”. In: *Proceedings of the 16<sup>th</sup> ASCM Engineering Mechanics Conference*. July 16–18, University of Washington, Seattle.
- Chen, H. C., T. Liu, and E. T. Huang (2002). “Time-domain Simulation of large-amplitude ship roll motions by a Chimera RANS method”. In: *International Journal of Offshore and Polar Engineering* 12.3.
- Chen, H. C. and V. C. Patel (1985). *Calculation of Trailing-Edge, Stern and Wake Flows by a Time-Marching Solution of the Partially-Parabolic Equations*. Tech. rep. 285. Iowa Inst. Hydraulic Research.
- Choi, J. E., K. S. Min, J. H. Kim, S. B. Lee, and H. W. Seo (2010). “Resistance and propulsion characteristics of various commercial ships based on CFD results”. In: *Ocean Engineering* 37.7, pp. 549–566.
- Choi, J. K. and S. A. Kinnas (2001). “Prediction of non-axisymmetric effective wake by a three-dimensional Euler solver”. In: *Journal of Ship Research* 45.1, pp. 13–33.
- Coney, W. B. (1989). “A method for the design of a class of optimum marine propulsors”. PhD thesis. Massachusetts Institute of Technology.
- Conway, J. T. (1995). “Analytical solutions for the actuator disk with variable radial distribution of load”. In: *J. Fluid Mech.* 297, pp. 327–355.
- (1998). “Exact actuator disk solutions for non-uniform heavy loading and slipstream contraction”. In: *J. Fluid Mech.* 365, pp. 235–267.
- (2000). “Analytical solutions for the newtonian gravitational field induced by matter within axisymmetric boundaries”. In: *Monthly Notices of the Royal Astronomical Society* 316.3, pp. 540–554.
- Dai, C. M., J. J. Gorski, and H. J. Haussling (1991). “Computation of an integrated ducted propulsor/stern performance in axisymmetric flow”. In: *Propellers/Shafting '91 Symposium*. Virginia Beach, VA.
- de Vries, O. (1979). *Fluid dynamic aspects of wind energy conversion*. AGARD No.243.
- Dickmann, H. E. and J. Weissinger (1955). “Beitrag zur theorie optimaler dusenchrauben (Kortdusen)”. In: *Schiffbautechn* 49, pp. 452–486.
- Dobrev, I., F. Massouh, and M. Rapin (2007). “Actuator surface hybrid model”. In: vol. 75. 1.
- Dyne, G. (1967). *A method for the design of ducted propellers in a uniform flow*. Tech. rep. 62. SSPA.
- Falcão de Campos, J. A. C. (1983). “On the calculation of ducted propeller performance in axisymmetric flows”. PhD thesis. Delft University of Technology.

BIBLIOGRAPHY

- Froude, R. E. (1889). "On the part played in propulsion by differences of fluid pressure". In: *Transactions of the Institute of Naval Architects* 30, pp. 390–405.
- Gibson, I. S. (1972). "Application of vortex singularities to ducted propellers". PhD thesis. University of Newcastle upon Tyne.
- Gibson, I. S. and R. I. Lewis (1973). "Ducted propeller analysis by surface vorticity and actuator disk theory". In: *Proceedings of the Symposium on Ducted Propeller*. Royal Institute of Naval Architects.
- Goldstein, S. (1929). "On the vortex theory of screw propellers". In: *Proceedings of the Royal Society of London. Series A* 123.792, pp. 440–465.
- Gradshteyn, I. S. and I. M. Ryzhik (1980). *Tables of integrals, series and products*. Academic press.
- Greenberg, M. D. (1972). "Nonlinear actuator disk theory." In: *Zeitschrift fuer Flugwissenschaften* 20, pp. 90–98.
- Greenberg, M. D. and S. R. Powers (1970). *Nonlinear actuator disk theory and flow field calculations, including nonuniform loading*. Tech. rep. CR-1672. NASA.
- Greve, M., K. Wöckner-Kluwe, M. Abdel-Maksoud, and T. Rung (2012). "Viscous-Inviscid Coupling Methods for Advanced Marine Propeller Applications". In: *International Journal of Rotating Machinery* 2012.
- Haimov, H., J. Vicario, and J. Del Corral (2011). "RANSE code application for ducted and endplate propellers in open water". In: *Proceedings of the Second International Symposium on Marine Propulsors*. Hamburg, Germany.
- Hansen, M. O. L., N. N. Sorensen, and R. G. Flay (2000). "Effect of placing a diffuser around a wind turbine". In: *Wind Energy* 3, pp. 207–213.
- Hess, J. L. and W. O. Valarezo (1985). "Calculation of steady flow about propellers using a surface panel method". In: *Journal of Propulsion and Power* 1.6, pp. 470–476.
- Hobson, E. W. (1896). "On a type of spherical harmonics of unrestricted degree, order, and argument". In: *Philosophical Transactions of the Royal Society of London. Series A, Containing Papers of a Mathematical or Physical Character* 187, pp. 443–531.
- Hoekstra, M. (2006). "A RANS-based analysis tool for ducted propeller systems in open water condition". In: *International shipbuilding progress* 53.3, pp. 205–227.
- Horlock, J. H. (1978). *Actuator disk theory*. McGraw-Hill.
- Horn, F. (1940). "Beitrag zur Theorie ummantelter Schiffsschrauben". In: *Jahrbuch der schiffbautechnischen Gesellschaft*, pp. 106–187.

- Horn, F. and H. Amtsberg (1950). "Entwurf von Schiffsdüsen systemen (Kortdüsen)". In: *Jahrbuch der schiffbautechnischen Gesellschaft* 44, pp. 141–206.
- Hough, G. R. and D. E. Ordway (1964). "The generalized actuator disk". In: *Developments in Theoretical and Applied Mechanics* 2, pp. 317–336.
- Hughes, M. J., S. A. Kinnas, and J. E. Kerwin (1992). "Experimental validation of a ducted propeller analysis method". In: *ASME Transactions Journal of Fluids Engineering* 114, pp. 214–219.
- Ivanell, S. (2009). "Numerical computations of wind turbine wakes". PhD thesis. KTH, Royal Inst. Technol.
- Ivanell, S., R. Mikkelsen, J. N. Sørensen, and D. Henningson (2008). "Three dimensional actuator disc modelling of wind farm wake interaction". In: *Proceedings of the European Wind Energy Conference*.
- Ivanell, S., J. N. Sørensen, R. Mikkelsen, and D. Henningson (2009). "Analysis of numerically generated wake structures". In: *Wind Energy* 12.1, pp. 63–80.
- Jacob, K. and F. W. Riegels (1963). "The calculation of the pressure distributions over aerofoil sections of finite thickness with and without flaps and slats". In: *Z. Flugwiss* 11.9, pp. 357–367.
- Kawamura, T., H. Miyata, and K. Mashimo (1997). "Numerical simulation of the flow about self-propelling tanker models". In: *Journal of Marine Science and Technology* 2.4, pp. 245–256.
- Kerwin, J. E., D. P. Keenan, S. D. Black, and Diggs (1994). "A coupled viscous/potential flow design method for wake-adapted, multi-stage, ducted propulsors using generalized geometry. Discussion. Authors' closure". In: *Transactions-Society of Naval Architects and Marine Engineers* 102, pp. 23–56.
- Kerwin, J. E., S. A. Kinnas, J. T. Lee, and W. Shih (1987). "A surface panel method for the hydrodynamic analysis of ducted propellers". In: *Trans. SNAME* 95.
- Kerwin, J. E. and C. S. Lee (1978). "Prediction of steady and unsteady marine propeller performance by numerical lifting-surface theory". In: *Trans. SNAME*, pp. 218–253.
- Kerwin, J. E. and R. Leopold (1964). "A Design Theory for Subcavitating Propellers". In: *Transactions of the Society of Naval Architects and Marine Engineers* 72.
- Kim, J., E. Paterson, and F. Stern (2003). "Sub-visual and acoustic modeling for ducted marine propulsor". In: *Proceedings of the 8th International Conference on Numerical Ship Hydrodynamics*. Busan, Korea, pp. 22–25.

BIBLIOGRAPHY

- Kinnas, S. A. and W. B. Coney (1988). “On the optimum ducted propeller loading”. In: *Proceedings Propellers '88 Symposium*, pp. 1.1–1.13.
- (1992). “The generalised image model - An application to the design of ducted propellers”. In: *Journal of Ship Research* 36, pp. 197–209.
- Kinnas, S. A., P. Griffin, J. K. Choi, and E. Kosal (1998). “Automated design of propulsor blades for high-speed ocean vehicle applications”. In: *Trans. SNAME* 106.
- Kort, L. (1934). “Der neue düsenschrauben-antrieb”. In: *Werft, Reederei und Hafen* 15.
- Küchemann, D. and J. Weber (1953). *Aerodynamics of propulsion*. McGraw-Hill.
- Lamb, H. (1932). *Hydrodynamics*. Cambridge University Press.
- Lanzafame, R. and M. Messina (2013). “Advanced brake state model and aerodynamic post-stall model for horizontal axis wind turbines”. In: *Renewable Energy* 50, pp. 415–420.
- Larsen, G. C., H. A. Madsen, K. Thomsen, and T. J. Larsen (2008). “Wake meandering: a pragmatic approach”. In: *Wind Energy* 11.4, pp. 377–395.
- Leclerc, C. and C. Masson (2004). “Toward blade-tip vortex simulation with an actuator-lifting surface model”. In: *AIAA Paper*.
- Lee, H. and S. A. Kinnas (2001). *MPUF3A (Version 1.2) user’s manual and documentation*. Tech. rep. 01-2.
- Lee, S. K. and H. C. Chen (2005). “The influence of propeller/hull interaction on propeller induced cavitating pressure”. In: *ISOPE Conference*. June 19–24, Seoul, Korea, pp. 25–33.
- Lerbs, H. W. (1952). “Moderately loaded propellers with a finite number of blades and an arbitrary distribution of circulation”. In: *Transactions of the Society of Naval Architects and Marine Engineers* 60, pp. 73–123.
- Lewis, R. I. (1991). *Vortex element methods for fluid dynamic analysis of engineering systems*. Cambridge University Press.
- Liu, Y. H. and M. Ikehata (1995). “Investigation into hub effect of marine propeller by surface vortex lattice method”. In: *Journal of the Society of Naval Architects of Japan* 177, pp. 59–66.
- Ludolph, K. (1977). *Propeller-Hub Interference Effects Using an Approximate Lifting Surface Theory*. Tech. rep. File No. TM 77-198. Applied Research Laboratory, The Pennsylvania State University.
- Luttmer, B. R. I. and F. A. J. Jassen (1982). *Laser-Doppler velocity measurements round and force measurements on a duct 37 with and without propeller*. Tech. rep. 50156-1-SR. Netherlands Ship Model Basin.

- Lyness, J. N. (1970). “Algorithm 379: Squank (Simpson Quadrature Used Adaptivity-Noise Killed)”. In: *Communications of the ACM* 13.4, pp. 260–263.
- Madsen, H. A. (1996). “A CFD analysis of the actuator disc flow compared with momentum theory results”. In: *Proc. 10th IEA Symp. on the Aerodynamics of Wind Turbines*, pp. 109–124.
- Madsen, H. A. and F. Rasmussen (1999). “The influence on energy conversion and induction from large blade deflections”. In: *Proceeding of the European Wind Energy Conference*, pp. 138–141.
- Martensen, E. (1959). “Berechnung der druckverteilung an gitterprofilen in ebener potentialströmung mit einer Fredholmschen integralgleichung.” In: *Arch. Rat. Mech.* 3, pp. 235–270.
- Masson, C., I. Ammara, and I. Paraschivoiu (1997). “An aerodynamic method for the analysis of isolated horizontal-axis wind turbines”. In: *International Journal of Rotating Machinery* 3.1, pp. 21–32.
- McCormick, B. W. (1955). “The effect of a finite hub on the optimum propeller”. In: *Journal of the Aeronautical Sciences* 22.9, pp. 645–650.
- Mikkelsen, R. (2003). “Actuator disc methods applied to wind turbines”. PhD thesis. Technical University of Denmark.
- Mikkelsen, R. F. and J. N. Sørensen (2000). “Yaw analysis using a numerical actuator disc model”. In: *Proceedings of the 14th IEA symposium on the aerodynamics of wind turbines*.
- Mikkelsen, R., J. N. Sørensen, S. Øye, and N. Troldborg (2007). “Analysis of power enhancement for a row of wind turbines using the actuator line technique”. In: *Journal of Physics: Conference Series*. Vol. 75. 1.
- Mikkelsen, R., J. N. Sørensen, and W. Z. Shen (2001). “Modelling and analysis of the flow field around a coned rotor”. In: *Wind Energy* 4.3, pp. 121–135.
- Miyata, H., M. Zhu, and O. Watanabe (1992). “Numerical study on a viscous flow with free-surface waves about a ship in steady straight course by a finite-volume method”. In: *Journal of Ship Research* 32.4, pp. 332–345.
- Morgan, W. B. (1961). *A theory of the ducted propeller with a finite number of blades*. Tech. rep. University of California, Berkeley, Institute of engineering research.
- (1962). “Theory of the annular airfoil and ducted propeller”. In: *Proceedings of the Fourth Symposium on Naval Hydrodynamics*, pp. 151–197.
- Morgan, W. B. and E. B. Caster (1968). “Comparison of theory and experiment on ducted propellers”. In: *Proceedings of the 7th Symposium on Naval Hydrodynamics*. Ed. by R. D. Cooper and S. W. Doroff, pp. 1311–1349.

- Nakatake, K. (1989). “On ship hull-propeller-rudder interactions (in Japanese)”. In: *Proceedings of the 3<sup>rd</sup> JSPC Symposium*. Japan Ship Performance Committee, Society of Naval Architects of Japan. Tokyo, pp. 231–259.
- Nyiri, A. and L. Baranyi (1983). “Numerical method for calculating the flow around a cascade of aerofoils”. In: *Proceedings of VII international J.S.M.E. symposium fluid machinery and fluidics*. Tokyo: vol. 2.
- Oosterveld, M. W. C. (1970). *Wake adapted ducted propellers*. Tech. rep. 345. Wageningen, Netherlands: Netherlands Ship Model Basin.
- Ordway, D. E., M. M. Sluyter, and B. O. U. Sonnerup (1960). *Three-Dimensional Theory of Ducted Propellers*.
- Phillips, A. B., S. R. Turnock, and M. Furlong (2009). “Evaluation of manoeuvring coefficients of a self-propelled ship using a blade element momentum propeller model coupled to a Reynolds averaged Navier Stokes flow solver”. In: *Ocean Engineering* 36.15, pp. 1217–1225.
- Piquet, J., P. Queutey, and M. Visonneau (1987). “Computation of viscous flows past axisymmetric bodies with and without a propeller in operation”. In: *Numer. Methods in Laminar and Turbulent Flow* 5, pp. 644–655.
- Prudnikov, A. P., Yu. A. Aleksandrovich Brychkov, and O. I. Marichev (1992). *Integrals and Series: Direct Laplace Transforms. Vol. 4*. Gordon and Breach Science Publishers.
- Rankine, W. J. M. (1865). “On the mechanical principles of the action of propellers”. In: *Trans. Inst. Nav. Arch.* 6.
- Réthoré, P.-E. M. and N. N. Sørensen (2008). “Actuator disc model using a modified Rhie-Chow/SIMPLE pressure correction algorithm. Comparison with analytical solutions”. In: *EWEC 2008 Conference Proceedings*. The European Wind Energy Association.
- Rubinstein, L. (1998). *Partial differential equations in classical mathematical physics*. Cambridge University Press.
- Ryan, P. G. and E. J. Glover (1972). “A ducted propeller design method: a new approach using surface vorticity distribution techniques and lifting line theory”. In: *Trans. R.I.N.A.* 114, pp. 545–563.
- Sadat-Hosseini, H., P. Carrica, F. Stern, N. Umeda, H. Hashimoto, S. Yamamura, and A. Mastuda (2011). “CFD, system-based and EFD study of ship dynamic instability events: Surf-riding, periodic motion, and broaching”. In: *Ocean Engineering* 38.1, pp. 88–110.
- Sánchez-Caja, A., J. V. Pykkänen, and T. P. Sipilä (2008). “Simulation of the incompressible viscous flow around ducted propellers with rudders using a RANSE solver”. In: *Proceeding of the 27th Symposium on Naval Hydrodynamics*. Seoul, Korea.

- Schetz, J. A. and S. Favin (1977). “Numerical solution for the near wake of a body with propeller”. In: *Journal of Hydronautics* 11.4, pp. 136–141.
- (1979). “Numerical solution of a body-propeller combination flow including swirl and comparisons with data”. In: *Journal of Hydronautics* 13.2, pp. 46–51.
- Shen, W. Z., J. H. Zhang, and J. N. Sørensen (2009). “The actuator surface model: a new Navier-Stokes based model for rotor computations”. In: *Journal of solar energy engineering* 131.1.
- Sibuet Watters, C. and C. Masson (2007). “Recent advances in modeling of wind turbine wake vortical structure using a differential actuator disk theory”. In: *Journal of Physics: Conference Series*. Vol. 75. 1.
- Sileo, L. and S. Steen (2009). “Numerical investigation of the interaction between a stern tunnel thruster and two ducted main propellers”. In: *Proceedings First International Symposium on Marine Propulsors*. Trondheim, Norway.
- Sonine, N. J. (1880). “Recherches sur les fonction cylindriques et le développement des fonctions continues en séries”. In: *Math. Ann.* 16.1, pp. 1–80.
- Sørensen, J. N. and C. W. Kock (1995). “A model for unsteady rotor aerodynamics”. In: *Journal of wind engineering and industrial aerodynamics* 58.3, pp. 259–275.
- Sørensen, J. N. and A. Myken (1992). “Unsteady actuator disc model for horizontal axis wind turbines”. In: *Journal of Wind Engineering and Industrial Aerodynamics* 39.1, pp. 139–149.
- Sørensen, J. N. and W. Z. Shen (2002). “Numerical modeling of wind turbine wakes”. In: *Journal of fluids engineering* 124.2, pp. 393–399.
- Sørensen, J. N., W. Z. Shen, and X. Munduate (1998). “Analysis of wake states by a full-field actuator disc model”. In: *Wind Energy* 1.2, pp. 73–88.
- Stern, F., H. T. Kim, V. C. Patel, and H. C. Chen (1988a). “A viscous-flow approach to the computation of propeller-hull interaction”. In: *Journal of Ship Research* 32.4, pp. 246–262.
- (1988b). “Computation of viscous flow around propeller-shaft configurations”. In: *Journal of ship research* 32.4, pp. 263–284.
- Stern, F., H. T. Kim, D. H. Zhang, Y. Toda, J. Kerwin, and S. Jessup (1994). “Computation of viscous flow around propeller-body configurations: series 60  $C_B = 0.6$  Ship Model”. In: *Journal of ship research* 38.2, pp. 137–157.
- Stern, F., Y. Toda, and H. T. Kim (1991). “Computation of viscous flow around propeller-body configurations: Iowa axisymmetric body”. In: *Journal of Ship Research* 35.2, pp. 151–161.

BIBLIOGRAPHY

- Stipa, L. (1931). “Ala a turbina”. In: *L’Aerotecnica*, pp. 923–953. Translated by D. M. Miner, NACA TM 655, 1932.
- Tachmindji, A. J. (1956). *The potential problem of the optimum propeller with finite hub*. Tech. rep. DTIC Document.
- (1958). “The potential problem of the optimum propeller with finite number of blades operating in a cylindrical duct”. In: *Journal of Ship Research* 2.3, pp. 23–32.
- Tikhonov, A. N. and A. A. Samarskii (1990). *Equations of mathematical physics*. Dover publications.
- Toda, Y., F. Stern, I. Tanaka, and V. C. Patel (1900). “Mean-flow measurements in the boundary layer and wake of a series 60  $C_B = 0.6$  model ship with and without propeller”. In: *Journal of Ship Research* 34.4, pp. 225–252.
- Troldborg, N. (2008). “Actuator line modeling of wind turbine wakes”. PhD thesis. Technical University of Denmark.
- Troldborg, N., J. N. Sørensen, and R. Mikkelsen (2010). “Numerical simulations of wake characteristics of a wind turbine in uniform inflow”. In: *Wind Energy* 13.1, pp. 86–99.
- Tsakonas, S., W. R. Jacobs, and M. R. Ali (1978). “Propeller-duct interaction due to loading and thickness effects”. In: *Proceedings of the Propellers/Shafting ’78 Symposium, SNAME*.
- Van Gunsteren, L. A. (1973). “A contribution to the solution of some specific ship propulsion problems”. PhD thesis. Delft University of Technology.
- Van Houten, R. (1986). *Analysis of ducted propellers in steady flow*. Tech. rep. Watertown, Mass.: Airflow Research and Manufacturing Corp.
- Van Manen, J. D. (1957). “Recent research on propellers in nozzles”. In: *International Shipbuilding Progress* 4.36.
- (1962). “Effect of radial load distribution on the performance of shrouded propellers”. In: *Transaction RINA*.
- Van Manen, J. D. and M. W. C. Oosterveld (1966). “Analysis of ducted propeller design”. In: *Transaction SNAME* 74, pp. 522–561.
- Van Manen, J. D. and A. Superina (1959). “The design of screw propellers in nozzles”. In: *International Shipbuilding Progress* 6.55, pp. 95–113.
- Von Mises, R. (1945). *Theory of flight*. McGraw-Hill.
- Wang, M. H. (1985). “Hub Effects in Propeller Design and Analysis.” PhD thesis. Massachusetts Institute of Technology.
- Wang, T., L. D. Zhou, and X. Zhang (2003). “Numerical simulation of 3-D integrative viscous complicated flow field around axisymmetric body with ducted propulsion”. In: *Journal of Ship Mechanics* 7.2, pp. 21–32.

- Watanabe, O., A. Masuko, and Y. Shiorose (1994). "Numerical simulation of a wave-viscous flow about a ship including propeller effects." In: *Proceedings 20<sup>th</sup> Symposium on Naval Hydrodynamics*. National Academy Press, Washington DC, pp. 946–958.
- Watson, G. N. (1944). *A treatise on the theory of Bessel functions*. Cambridge university press.
- Weems, K. M., R. A. Korpus, W. M. Lin, M. Fritts, and H. C. Chen (1994). "Near-Field Flow Prediction for Ship Design". In: *Proceedings of the 20<sup>th</sup> Symposium on Naval Hydrodynamics*. 21–26 August, University of California, Santa Barbara, CA, pp. 21–26.
- Wilkinson, D. H. (1967a). *A numerical solution of the analysis and design problems for the flow past one or more aerofoils or cascades*. Tech. rep. 3545. A.R.C.
- (1967b). *The calculation of rotational, non-solenoidal flows past two dimensional aerofoils and cascades*. Tech. rep. W/M(6C). English Electric, M.E.L.
- Wu, T. Y. (1962). "Flow through a heavily loaded actuator disc". In: *Schiffstechnik* 9, pp. 134–138.
- Yang, C.I., P. Hartwich, and P. Sundaram (1991). "A Navier-Stokes solution of hull-ring wing-thruster interaction". In: *Proceedings of the Eighteenth Symposium on Naval Hydrodynamics*. Vol. 1, pp. 687–696.
- Zhang, D. H., L. Broberg, L. Larsson, and G. Dyne (1991). "A method for computing stern flows with an operating propeller". In: *Transactions of the Royal Institution of Naval Architects* 134, pp. 245–259.